



The Composition of Saturn's Rings

Kelly E. Miller¹ · Gianrico Filacchione² · Jeffrey N. Cuzzi³ · Philip D. Nicholson⁴ · Matthew M. Hedman⁵ · Kevin Baillié⁶ · Robert E. Johnson⁷ · Wei-Ling Tseng⁸ · Paul R. Estrada³ · Jack Hunter Waite⁹ · Mauro Ciarniello² · Cécile Ferrari¹⁰ · Zhimeng Zhang¹¹ · Amanda Hendrix¹² · Julianne I. Moses¹³ · Hsiang-Wen Hsu¹⁴

Received: 5 October 2023 / Accepted: 20 August 2024

© The Author(s) 2024

Abstract

The origin and evolution of Saturn's rings is critical to understanding the Saturnian system as a whole. Here, we discuss the physical and chemical composition of the rings, as a foundation for evolutionary models described in subsequent chapters. We review the physical characteristics of the main rings, and summarize current constraints on their chemical composition. Radial trends are observed in temperature and to a limited extent in particle size distribution, with the C ring exhibiting higher temperatures and a larger population of small particles. The C ring also shows evidence for the greatest abundance of silicate material, perhaps indicative of formation from a rocky body. The C ring and Cassini Division have lower optical depths than the A and B rings, which contributes to the higher abundance of the exogenous neutral absorber in these regions. Overall, the main ring composition is strongly dominated by water ice, with minor silicate, UV absorber, and neutral absorber components. Sampling of the innermost D ring during Cassini's Grand Finale provides a new set of in situ constraints on the ring composition, and we explore ongoing work to understand the linkages between the main rings and the D ring. The D ring material is organic- and silicate-rich and water-poor relative to the main rings, with a large population of small grains. This composition may be explained in part by volatile losses in the D ring, and current constraints suggest some degree of fractionation rather than sampling of the bulk D ring material.

Keywords Ring particle composition, mixing and particle size distribution · Ring radial and vertical structure · Ring atmosphere

1 Introduction

The rings are a prominent and unique feature in the Saturnian system, and they serve both as a witness plate and a driver for the evolution of the system via interactions with both the moons and Saturn itself. In this chapter we review current knowledge of the physical and chemical composition of Saturn's rings, with a focus on the main rings and the innermost D ring. We begin in Sect. 1 with an overview of the ring structure and main evolutionary processes affecting the rings. In Sect. 2, we describe the physical properties of the main rings, including their brightness, particle size distribution and temperature. Remote sensing constraints on the main rings' chemical composition are then reviewed in Sects. 3, 4 and 5.

Extended author information available on the last page of the article

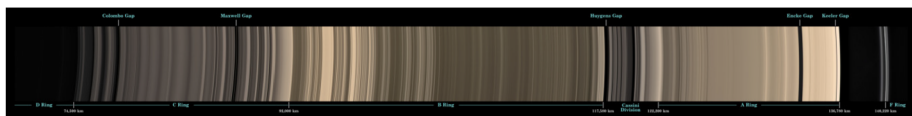


Fig. 1 An optical mosaic of the dark side of Saturn's rings, obtained by the narrow-angle camera of the Cassini ISS instrument. From left to right, we see the broad C, B and A rings at increasing radii, flanked by the narrow F ring at the extreme right. Note the numerous narrow gaps, appearing here as black bands in the C ring, the Cassini Division and in the outer part of the A ring. Courtesy: NASA/JPL-Caltech/Space Science Institute

Section 6 reviews our current knowledge of the D ring, which is thought to be the immediate source for the inflowing ring material that was measured in situ by Cassini and is described in Sect. 7. Current constraints suggest this material includes a gas-phase component, and we review our knowledge of the ring atmosphere and possible connections to the inflowing material in Sect. 8. Finally, we briefly explore the relationship between the main ring composition and the ring moons in Sect. 9, before summarizing our conclusions in Sect. 10.

1.1 Background on Ring Structure

1.1.1 Terminology and Dimensions

Saturn's dense rings (or “main rings”) are traditionally divided into three major components known as the A, B and C rings (see Fig. 1). The outermost or A ring extends from a radius of 136,770 km relative to Saturn's center inward to $\sim 122,000$ km; the outer edge at ~ 2.25 Saturn radii (R_S , where Saturn's equatorial radius is 60,268 km) essentially marks the Roche Limit for self-gravitating icy particles (Tiscareno et al. 2013a). The middle or B ring extends from 117,570 km inward to $\sim 92,000$ km, and is both the brightest and most opaque of the main rings, containing approximately 2/3 of the system's total mass. The inner or C ring extends from the B ring inward to 74,490 km, or $\sim 1.25 R_S$. Located between the A and B rings is the 4500 km wide Cassini Division (“CD”), which Voyager data showed to be comparable in brightness and optical depth to the C ring and which is now considered to be a distinct fourth component of the main rings.

In comparison to their radial width of $\sim 62,000$ km, or almost 10 Earth radii, Saturn's rings are extremely thin. Theoretical estimates based on collisional equilibrium suggest that their centrifugal scale height H is likely to be of order 10 m, a value that is supported by a limited number of experimental estimates ranging from < 30 m in the C ring and Cassini Division to ~ 6 m in the A ring (Hedman et al. 2007b; Jerousek et al. 2011).

Although it is less opaque and almost certainly contains much less material than the main rings, we include in this chapter the nearby D ring, primarily because of the *in situ* sampling by Cassini on its final orbits that observed material hypothesized to originate from this region. The D ring extends inwards from the C ring almost to the outer reaches of the planet's atmosphere at a radius of $< 68,000$ km. Invisible in Earth-based images and in most optical depth profiles, the D ring is dominated by a series of narrow, dusty ringlets and is most readily seen in images taken in forward-scattering geometries (see Sect. 6).

Limited *in situ* sampling near the F ring region outside of the A ring was also performed by Cassini. This ring, which is both shepherded and perturbed by the ring moons Pandora and Prometheus, is discussed further in Ciarniello et al. (2024, this collection), along with the dusty G ring that is associated with the satellite Aegaeon.

Not included in this volume is the very tenuous and isolated E ring, which is associated with the satellite Enceladus, or the even more distant “Phoebe ring” discovered by the Spitzer space telescope (Verbiscer Astron et al. 2009). For information on these rings the interested reader is directed to the reviews by Hedman et al. (2018) and Murray and French (2018) in the book “Planetary Ring Systems” (Tiscareno and Murray 2018).

1.1.2 Optical Depths and Ring Structure

The density of a planetary ring is usually expressed in terms of its normal optical depth τ , which in general is a function of the wavelength of observation λ and the particle size distribution $n(a)$:

$$\tau(\lambda) = \pi \int_{a_{\min}}^{a_{\max}} Q_{\text{ext}}(a, \lambda) a^2 n(a) da \quad (1)$$

where $n(a)da$ is the number of ring particles per unit ring area with particle radii between a and $a + da$ and $Q_{\text{ext}}(a, \lambda)$ is their extinction efficiency at wavelength λ . For quasi-spherical particles, Q_{ext} approaches 0 when the size parameter $x = 2\pi a/\lambda$ is much less than 1, but approaches an asymptotic value between 1 and 2 for $x \gg 1$ (Cuzzi 1985; French and Nicholson 2000).

Detailed radial profiles of optical depth for Saturn’s rings are available from stellar occultations observed by the Ultraviolet Imaging Spectrometer (UVIS; Esposito et al. 2004) at $\lambda \simeq 0.15 \mu\text{m}$ and by the Visual and Infrared Mapping Spectrometer (VIMS; Brown et al. 2004) at $\lambda = 2.9 \mu\text{m}$, for both of which $Q_{\text{ext}} \simeq 1$, as well as radio occultations observed by the Radio Science Subsystem (RSS; Kliore Astron et al. 2004) at Ka-band ($\lambda = 0.94 \text{ cm}$), X-band (3.4 cm) and S-band (13 cm) (Cuzzi et al. 2009).¹

A second useful quantity is the surface mass density of the ring for a given distance (*i.e.*, the mass per unit ring area), expressed as:

$$\Sigma = \frac{4\pi}{3} \int_{a_{\min}}^{a_{\max}} \rho a^3 n(a) da \quad (2)$$

where ρ is the average internal density of the ring particles. For a ring composed of spherical particles with a narrow range of sizes and $Q_{\text{ext}} \simeq 1$, the ratio Σ/τ is approximately equal to $\frac{4}{3}\rho\bar{a}$, where \bar{a} is the mean particle radius. The inverse quantity τ/Σ is known as the opacity of the ring, and is a measure of its optical cross section per unit mass.²

1.2 Relationship of Composition to Ring Age

Evolutionary processes alter the physical and chemical composition of the rings, and an understanding of the types and timescales of these forms of alteration is an essential element

¹For most of the regions in the main rings, $a \gg \lambda$ for the UVIS and VIMS occultation data and $Q_{\text{ext}} \simeq 1$, but for the RSS occultation data, $a \simeq \lambda$ and $Q_{\text{ext}} \simeq 2$ due to the particles’ broad diffraction lobes at cm-wavelengths, as well as the coherent nature of the spacecraft’s radio signal.

²The quantity κ is generally used in radiative transfer to indicate the opacity (cm^2/g) of a medium, or its cross section (for absorption, scattering, or both) per unit surface mass density. Then the incremental optical depth $d\tau$ of a thin layer dz is $d\tau = \kappa\rho dz$. Integrating this expression over the thickness of a ring layer, the normal optical depth of the ring is $\tau = \kappa\Sigma$, where Σ is the surface mass density in g/cm^2 . A related quantity is the extinction coefficient k whereby $d\tau = kdz$ and thus $k = nQ\pi a^2 (\text{cm}^{-1})$, for particles with volume density n (cm^{-3}) and a single particle size a , having (absorption, scattering, or both) efficiency Q (dimensionless)..

of the determination of the ring age. Here, we summarize the primary processes known to drive evolution of the main rings. For an in-depth discussion of the ring age, see Crida et al. (2024, this collection).

1.2.1 Physical Evolution

The physical evolution of the rings is controlled by interparticle collisions and the rings' self-gravity, both of which determine the rings' viscosity and thickness as described below, as well as by gravitational interactions with distant and embedded satellites. In order to estimate the dynamical age of the rings, the two critical parameters are the surface mass density Σ and the effective kinematic viscosity of the rings ν , which control the rate at which keplerian shear within the rings leads to their radial spreading over time. The latter rate is determined by the outward viscous angular momentum flux across the rings

$$F_\nu(r) = \frac{3}{2} \nu \Sigma \Omega r, \quad (3)$$

where $\Omega \approx \sqrt{GM_S/r^3}$ is the local keplerian angular velocity at a radius r from Saturn in the rings (Lynden-Bell and Pringle 1974; Longaretti 2018).

Theoretical models suggest that there are at least three important sources of viscosity: the normal "local viscosity" due to random velocities and the resulting collisions between individual ring particles,³ a "nonlocal viscosity" due to transmission of momentum across large particles in densely-packed rings, and the transfer of momentum by gravitational interactions associated with self-gravity wakes (Daisaka et al. 2001; Longaretti 2018). These self-gravity wakes are 100-m- to km-scale temporary aggregations of particles that form within the Roche limit but are subsequently sheared out and disrupted by tidal forces and the keplerian angular velocity gradient within the rings. The relative importance of these processes in different parts of the rings is not well-known, but gravitational interactions are expected to be dominant in the A ring, where self-gravity wakes are ubiquitous (Colwell et al. 2006; Hedman et al. 2007a).

Empirical estimates of ν come from two sources: the damping of density and bending waves, and the balancing of the viscous torque $2\pi r F_\nu$ with gravitational torques exerted at satellite resonances. For the A ring, estimates of the former lead to $\nu = 40$ to $200 \text{ cm}^2 \text{ s}^{-1}$ (Tiscareno et al. 2007), comparable to the self-gravity-wake viscosity of $\sim 100 \text{ cm}^2 \text{ s}^{-1}$. Balancing the viscous and satellite torques, on the other hand, Tajeddine et al. (2017) find somewhat lower values for the A ring of $\nu = 10 - 50 \text{ cm}^2 \text{ s}^{-1}$ and a similar value for the B ring of $\sim 30 \text{ cm}^2 \text{ s}^{-1}$. There are few reliable estimates in the C ring or Cassini Division.

Under the (probably erroneous) assumption that the dominant contribution to viscosity is local, the measured value of ν can be used to estimate an upper limit on the root mean square (rms) random velocity of particles in the ring plane c via the expression (Goldreich and Tremaine 1978):

$$c^2 = 2\nu\Omega \frac{1 + \tau^2}{\tau}. \quad (4)$$

If the velocity ellipsoid is isotropic, then the ring's centrifugal scale height is simply $H \simeq c/\Omega$. The lower values quoted above for ν imply that $c \leq 0.05 - 0.25 \text{ cm s}^{-1}$ and $H \leq 4 - 20 \text{ m}$ in the A ring and that $c \leq 0.2 \text{ cm s}^{-1}$ and $H \leq 10 \text{ m}$ in the B ring, consistent with

³Akin to molecular viscosity in a fluid medium.

the more direct estimates given above. In the Cassini Division (and perhaps also the C ring), where self-gravity wakes are absent, the same argument leads to $H \simeq 3 - 5$ m (Colwell et al. 2009). In all cases, the ring thickness appears to be comparable to the size of the largest ring particles (see Sect. 2.3 below).

A lower limit on the velocity dispersion comes from the requirement that the rings be stable against axisymmetric and/or wake-type instabilities due to their self-gravity. Known as the Toomre criterion (Toomre 1964), this specifies a minimum value for the dimensionless ratio:

$$Q = \frac{c\Omega}{\pi G \Sigma} \quad (5)$$

of about 1. Numerical simulations show that stable rings with self-gravity wakes typically have $Q \simeq 2$ (see Fig. 14.7 of Schmidt et al. 2009), leading to estimates of $c \simeq 0.10$ and 0.15 cm s $^{-1}$ in the A and B rings, respectively.⁴ For further discussion of the dynamical and structural evolution timescales of the rings, see Crida et al. (2024, this collection).

1.2.2 Compositional Evolution

Apart from their dynamical evolution, ring particles also undergo compositional evolution because they are continuously exposed to exogenous processes such as photolysis and meteoritic particle bombardment, which are capable of altering their original state and chemical makeup. The composition of the rings is one of the key measurements that is useful in constraining their age. This latter topic is discussed in detail in Crida et al. (2024, this collection), and is briefly discussed here as context for the ring composition as a whole.

While the majority of compositional data for the rings comes from remote sensing at UV to infrared wavelengths, and therefore represents the ring particles' surface materials, these data are still useful constraints for the bulk composition of the rings, with the exception of the middle of C ring. The continuous low-velocity collisions among nearby ring particles, and mixing of their subsurfaces due to extrinsic bombardment by meteoroids (known as “impact gardening”) is commonly thought to result in a very efficient mixing of the exogenous and original ring material over timescales of 1 Myr or so, even at depths comparable to the size of the largest ring particles (Elliott and Esposito 2011). Similarly, the ring layer itself is well-mixed, as ring particles move vertically on their inclined orbits, colliding and bouncing around, fragmenting and re-forming, spending time at the faces as well as in the midplane and getting equally exposed on average (Morishima et al. 2010). Comparison of results from visible and near-IR studies with those obtained from microwave observations that sample the bulk of the ring material (Zhang et al. 2017a,b, 2019, see also Sect. 5) generally supports this mixing framework. Interestingly though, microwave data identify a unique part of the mid-C Ring where there is evidence favoring particles having icy mantles and rocky cores.

Owing to their huge surface-area-to-mass ratio (see Table 1), the rings are highly susceptible to the effects of micrometeoroid bombardment and the resulting ballistic transport of their impact ejecta. In particular, ring composition (which is predominantly icy, $\gtrsim 95\%$ by mass) is sensitive to the continuous infall of non-icy meteoroidal material that may accumulate over time. The CDA team’s final analysis of an extensive set of *in situ* observations collected over the more than a dozen years of the Cassini tour provides the total mass flux of

⁴Note that the keplerian angular velocity $\Omega \simeq 1.29 \times 10^{-4}$ s $^{-1}$ in the outer A ring and $\sim 1.66 \times 10^{-4}$ s $^{-1}$ in the middle B ring.

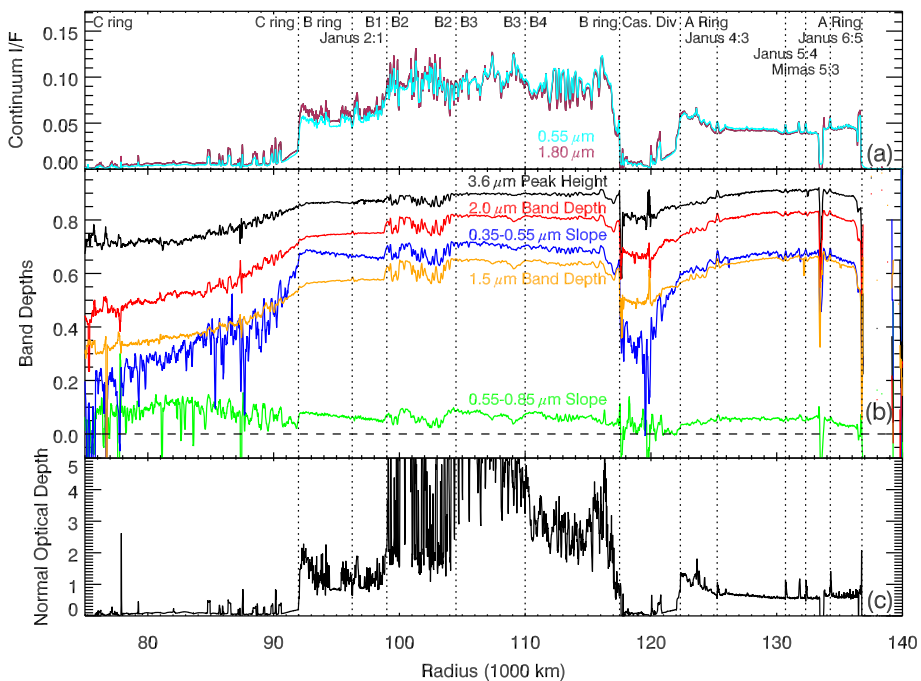


Fig. 2 Radial profiles of the main rings of Saturn derived from Cassini-VIMS observations. The upper panel shows the reflectivity of the rings at two continuum wavelengths of 0.55 and 1.8 μm , with the locations of the major ring boundaries and the strongest density waves identified by vertical dotted lines. The middle panel shows the fractional depths of the water ice bands at 1.55 and 2.0 μm , as well as the peak height at 3.6 μm and the blue and red slopes, rebinned to a uniform sampling resolution of 20 km and smoothed to 100 km. The lower panel shows an optical depth profile of the rings obtained from an occultation of the star γ Crucis, binned to 10 km resolution. (From Tiscareno et al. 2019)

extrinsic, non-icy material impinging on the rings (Kempf et al. 2023; see also discussion in Crida et al. 2024). The main conclusions from this study indicate that the magnitude of the measured flux entering the Saturnian system, between 0.69 and $2.7 \times 10^{-16} \text{ kg m}^{-2} \text{ s}^{-1}$, is roughly a factor of two smaller than previously derived estimates. Moreover, the dynamical origin of these extrinsic micrometeoroids is not from the Oort Cloud as previously assumed, but predominantly from the Edgeworth-Kuiper Belt (Kempf et al. 2023). The latter dynamical population is characterized by much lower entry speeds upon crossing Saturn's Hill sphere, and therefore is more strongly affected by gravitational focusing by the planet. As a result, the rate at which the rings are polluted is also faster. This polluting material is linked to the neutral absorbers, discussed further in Sect. 3.2.2.

2 Physical Properties of the Main Rings

The physical properties of the rings include characteristics such as their brightness and optical depth profiles, particle size distribution, surface mass density, temperature and thermal behavior.

Table 1 Radii, surface areas, surface mass densities, and estimated masses for the principal Saturnian rings

Ring region	R_{in} (km)	R_{out} (km)	Ring surface area (km^2)	Σ (kg m^{-2})	Mass (kg)	Mass(M_{Mimas})	Ref.
A ring	122,340	136,770	1.18×10^{10}	150–400	3.7×10^{18}	0.10	^a
Cass. Div.	117,930	122,340	3.3×10^9	15–190	1.7×10^{17}	0.004	^b
B ring	92,000	117,570	1.68×10^{10}	600	1.01×10^{19}	0.27	^c
C ring	74,490	92,000	9.2×10^9	10–60	3.4×10^{17}	0.009	^d
Total	74,490	136,770	4.11×10^{10}		1.43×10^{19}	0.38	

^a3-component model (Tiscareno et al. 2007; Tiscareno and Harris 2018)

^b2-component model (Colwell et al. 2009; Tiscareno et al. 2013b)

^caverage value used (Hedman and Nicholson 2016)

^d3-component model (Baillié et al. 2011; Hedman and Nicholson 2014)

2.1 Brightness and Optical Depth Profiles

Figure 2 compares two radial brightness profiles of the main rings in reflected light (I/F) as measured in the visible and near-infrared (top), as well as a profile of optical depth (bottom) measured by the VIMS instrument on the Cassini spacecraft. The spectral profiles in the middle panel of Fig. 2 are discussed further in Sect. 3 below. In the A ring, both the optical depth τ and I/F profiles are relatively flat, with an average $\tau \simeq 0.5$ in both the UV (Colwell et al. 2010) and near-IR (Hedman et al. 2013). There are two relatively narrow gaps in its outer part, known as the Encke and Keeler gaps.

The B ring is somewhat brighter than the A ring and much more structurally complex, with τ_{UV} and τ_{IR} ranging from a minimum of ~ 0.9 in the inner parts (known as the B1 region; see labels at top of Fig. 2) to > 5 in parts of the central (or B3) region. The microwave optical depths exceed the radio science detection threshold in the densest parts of the B Ring, partly because $Q_{\text{ext}} \simeq 2$.

The C ring, on the other hand, is relatively transparent. It is dominated by an undulating profile with an average $\tau \simeq 0.05 – 0.10$, punctuated by a series of narrow, more opaque features known as “plateaux” where $\tau \simeq 0.5$, as well as several narrow gaps, some of which contain optically-thick ringlets.

Located between the A and B rings, the Cassini Division shows many similarities to the C ring, with an average $\tau \simeq 0.10 – 0.20$, comprised of eight narrow gaps and three isolated ringlets (Nicholson et al. 2018).

The sharp outer edges of the A and B rings are controlled by strong satellite resonances (Nicholson et al. 2018), but their more gradual inner edges take the form of “ramps”, where τ decreases more-or-less linearly towards the much less opaque Cassini Division and C ring. These inner edges, and the inner edge of the D Ring, appear to be unconfined. In fact, many physical parameters change gradually across these ramps, which are believed to be generated by the process of ballistic transport (Durisen et al. 1989, 1996; Estrada et al. 2015). They are thus important sites for assessing the degree of long-term evolution of the rings, at least on a regional scale (for further discussion see Crida et al. 2024).

2.2 Surface Mass Density

The surface mass densities of the main ring regions (Table 1) have been estimated from the radial wavelengths of the many density and bending waves in the rings that are driven by

external satellites and planetary internal oscillations (Tiscareno et al. 2007; Colwell et al. 2009; Baillié et al. 2011; Hedman and Nicholson 2014, 2016). Numerous estimates for the A ring show that $150 < \Sigma < 400 \text{ kg m}^{-2}$ (Tiscareno et al. 2007; Tiscareno and Harris 2018), with an average value in the central A ring of 350 kg m^{-2} . In the Cassini Division Σ is much lower but varies substantially, ranging from ~ 15 in the inner part to almost 200 kg m^{-2} in the outer ramp (Colwell et al. 2009; Tiscareno et al. 2013b). Reliable data are much scarcer in the B ring, but one study finds that $\Sigma \simeq 600 \text{ kg m}^{-2}$ over much of this region (Hedman and Nicholson 2016), with surprisingly little radial variation. For the C ring Σ ranges from ~ 10 to 60 kg m^{-2} , with the highest values in the central undulating region (Baillié et al. 2011; Hedman and Nicholson 2014).

Based on the above surface mass densities, we can estimate the mass of the main ring components, as listed in Table 1. In units of the mass of the satellite Mimas ($M_{\text{Mimas}} = 3.75 \times 10^{19} \text{ kg}$), we find that the overall mass of the rings is $\sim 0.38 M_{\text{Mimas}}$. This value was confirmed when direct gravity measurements were made by Cassini on its final orbits, yielding $M_{\text{rings}} = (0.41 \pm 0.13) M_{\text{Mimas}}$ (Iess et al. 2019).

Indirect estimates of the average particle size in different ring regions can be made by combining the optical depth with the local surface mass density. As noted in Sect. 1.1.2, $\Sigma/\tau \simeq \frac{4}{3}\rho\bar{a}$, where ρ is the internal mass density of a particle and \bar{a} is the mean particle radius. Assuming an average particle density of 500 kg m^{-3} , suitable for porous water ice,⁵ we find that $\bar{a} \simeq 100 \text{ cm}$ in the A ring, $25 - 60 \text{ cm}$ in the B ring and $10 - 20 \text{ cm}$ in the C ring.

An unexpected result of such comparisons is that within both the B and C rings there appears to be little local correlation between Σ and τ , with τ varying much more than does Σ . This lack of correlation suggests that variations in the particle size distribution may be the cause of much of the observed variability in τ , rather than variations in the total amount of ring material per unit area. This is not currently well-understood. In the B ring, moreover, some local brightness variations may reflect variations in the albedo or phase function of the ring particles, rather than variations in either τ or Σ (Estrada and Cuzzi 1996).

2.3 Particle Size Distribution

The most direct constraints on the particle size distribution come primarily from the multi-wavelength RSS occultation data from Voyager (Zebker et al. 1985), estimates of the near-forward scattering cross-section of the rings at optical and near-IR wavelengths from Earth-based stellar occultation (French and Nicholson 2000), and comparisons of the measured values of optical depth τ in the Cassini UVIS (UV) and VIMS (near-IR) data with those obtained from microwave (RSS) data (Jerousek 2018; Jerousek et al. 2020).

The areal density $n(a)$ of particles of radius a can be modeled as a power law, $n(a) \propto a^{-q}$ for $a_{\min} < a < a_{\max}$. The power-law index q and the upper size limit for particles a_{\max} are both found to vary across the rings, as estimated using various methods. Representative estimates by ring location are provided in Table 2. In the A and C rings and in the Cassini Division, Zebker et al. (1985) and Cuzzi et al. (2009) report a differential index $q = 2.7 - 3.2$ and $a_{\max} \simeq 2 - 10 \text{ m}$. Because of its large optical depth, estimates of a_{\max} and q have a much greater uncertainty for the B ring.

The value of a_{\min} is more poorly defined, but occultations in the near-IR suggest that it varies from a few mm in the outer A ring and C ring to as much as 30 cm in the B

⁵“Ice” or “icy” are used interchangeably with “water ice” throughout the chapter, unless a different compound (e.g. methane) is noted.

Table 2 Particle size distributions in the main rings. Values are averaged by region for differential indices for model power-law particle size distributions in Saturn’s rings. Fits are derived from Voyager RSS data (Zebker et al. 1985), Earth-based 28 Sgr occultation in 1989 (French and Nicholson 2000) and Cassini UVIS, VIMS & RSS data (Jerousek 2018; Jerousek et al. 2020)

Ring Region	Radial location (km)	Avg. q	Min. a_{\min} (cm)	Max. a_{\max} (m)
C Ring background	74500 - 91980	3.16 ^a	0.42 ^a	11 ^a
C Ring Plateaux		3.08 ^a	0.36 ^a	13 ^a
C Ring ramp	90620 - 91980	3.16 ^a	0.38 ^a	13 ^a
B Ring ^b	91980 - 117500	$\sim 2.8^{c,d}$	0.5 ^d	7 ^e
Cassini Division background	117500 - 122100	2.85 ^f	0.41 ^a	8.9 ^a
Cassini Division Triple Band	120550 - 120800	2.94 ^a	0.61 ^a	7.6 ^a
Cassini Division ramp	120900 - 122100	3.07 ^a	0.33 ^a	20 ^a
A Ring inside Encke Gap	122100 - 133410	$2.9 \pm 0.1^{d,g}$	$\sim 2.5^d$	$5 - 10^{d,g}$
A Ring outside Encke Gap	133410 - 136800	$3.05 \pm 0.15^{d,g}$	0.4 ^d	$5 - 10^{d,g}$

^aJerousek et al. (2020)

^bConstraints are limited to regions of the B ring with lower optical depth

^cFrench and Nicholson (2000)

^dJerousek (2018)

^einner B ring, Jerousek (2018)

^fmean of values from Zebker et al. (1985) and Jerousek et al. (2020)

^gZebker et al. (1985)

and inner A rings (French and Nicholson 2000; Cuzzi et al. 2009; Harbison et al. 2013). Figure 3 summarizes the published estimates of power-law indices across the rings, while Fig. 4 shows the corresponding values of a_{\min} and a_{\max} .

Inverting the near-forward scattered signal from RSS, Zebker et al. (1985) derived a power-law index between $q = 2.7$ in the A ring and $q = 3.11$ in the C ring, with particles ranging from 1 mm to ~ 10 m. They also estimated that the Cassini Division has a slightly shallower (*i.e.*, smaller q) particle size distribution than the C ring, with $q = 2.79$, and maximum sizes of 4.5 – 7.5 m. Following the method of Zebker et al. (1985), Jerousek et al. (2020) determined separate power-law indices in the background C ring, in the C ring plateaux, in the background Cassini Division, and in the Triple Band that connects the inner Cassini Division outward to the ramp to the inner edge of the A ring.

Zebker et al. (1985) also found that the size distribution steepens from the inner A ring ($q = 2.7$) to the outer A ring ($q = 3.03$), with the largest values of q being found outside the Encke Gap at a radius of 133,500 km. This result was confirmed by subsequent studies (see Fig. 3). An abrupt jump in q has also been observed by Becker et al. (2016) in diffraction signatures at the edges of the Encke gap: they measured $q = 2.9$ and $a_{\min} = 15$ mm at the inner edge and $q = 3.1$ and $a_{\min} = 9.3$ mm at its outer edge. This trend continues to the outer edge of the A ring, where the minimum size is 4.4 mm with a power-law index of 3.2. This change in the size distribution may be related to an abrupt change in the A ring’s photometric properties (color and phase function) at the Encke gap (Tiscareno et al. 2019). The relative lack of small particles in the inner A ring is consistent with the analyses by Marouf et al. (1986) and Jerousek et al. (2016). Becker (2016) suggests that this depletion in sub-mm particles may indicate that the collisions in this region are too gentle to release

Fig. 3 Particle size distributions across Saturn's main rings: power-law indices inferred from Voyager RSS data (Zebker et al. 1985), 28 Sgr Earth-based occultation (French and Nicholson 2000), and Cassini UVIS, VIMS and RSS (Jerousek et al. 2020)

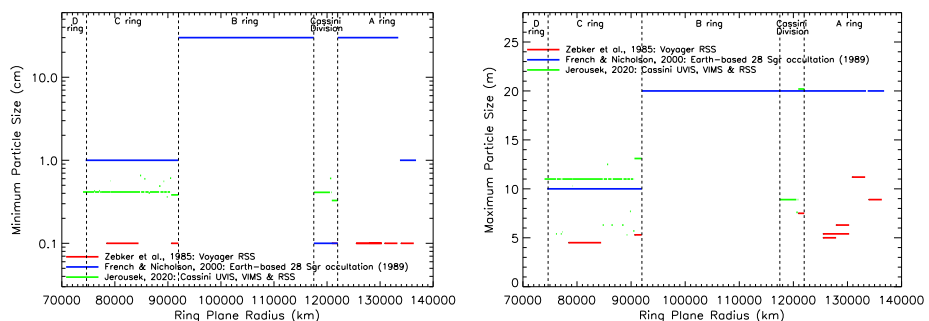
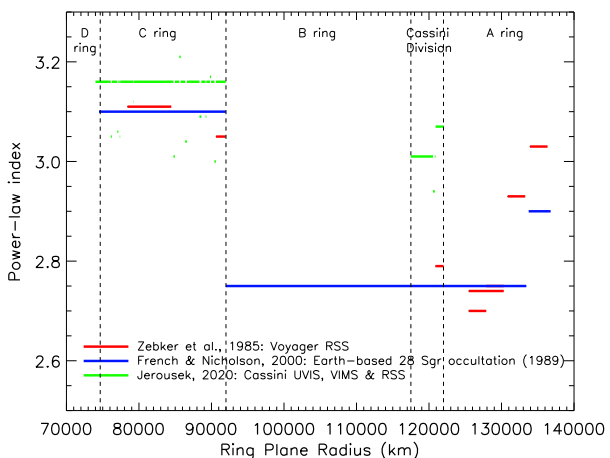


Fig. 4 Particle size distributions across Saturn's main rings: minimal (left) and maximal (right) limits for power-law distributions inferred from Voyager RSS data (Zebker et al. 1985), 28 Sgr Earth-based occultation (French and Nicholson 2000), and Cassini UVIS, VIMS and RSS (Jerousek et al. 2020)

enough energy to remove micron-sized dust from the surfaces of larger aggregates (Albers and Spahn 2006).

From the analysis of Cassini UVIS stellar occultation scans crossing the edges of the Encke and Keeler gaps, the R6, Huygens and Titan ringlets, as well as the outer edges of the A and B rings, Eckert et al. (2021) found minimum particle sizes ranging from 4.5 mm to 66 mm and average power law indices ranging from 3.0 to 3.2. Consistent with the results of Becker et al. (2016) and the RSS multi-wavelength profiles, this indicates that edges perturbed by satellite resonances tend to host more numerous sub-cm particles than the sharp edges of other ringlets. This result appears consistent with the predator-prey model detailed in Esposito et al. (2012), based on the competition between aggregation and fragmentation mechanisms in regions perturbed by satellite resonances. The kinetic model of Brilliantov et al. (2015) confirmed that the observed distributions could be consistent with the steady-state of such an aggregation/fragmentation mechanism.

Particles are much smaller in the D and F rings, with photometric and spectrophotometric data suggesting average sizes of a few tens of microns (Hedman et al. 2011; Vahidinia et al. 2011; Hedman and Stark 2015), although some regions of the F ring may contain a

substantial population of cm-sized particles (Cuzzi et al. 2014b). See Sect. 6.1 for further discussion of particle sizes in the D ring.

2.4 Embedded Moonlets

There is also evidence for a small population of much larger ring particles that are up to a few kilometers in size, distributed across the main rings. Daphnis (3.8 km in radius) and Pan (14.1 km in radius) define the upper limit of this population, followed by a population of \sim 100- to 1000-m- size objects, mainly observed by Cassini-ISS in the A and B rings (Spahn and Sremčević 2000; Tiscareno et al. 2006, 2008, 2010). These 100- to 1000-m objects are known as “propellers” because of the shape of the denser regions they produce in the rings surrounding depletion zones located ahead of the object (which is itself unseen) on its interior and behind the object on its exterior. Propellers form when the orbiting objects are too small to clear a full azimuthal gap but are large enough to clear small azimuthal regions of the rings in their immediate vicinity (Spahn et al. 2018). More massive moons result in perturbations that can open a gap all the way around the rings, as with Pan and Daphnis, which clear the Encke and Keeler gaps in the outer A ring (Nicholson et al. 2018, see Sect. 9 for further discussion). Propellers in the A ring are primarily detected in three narrow belts between radii of 126,750 and 132,000 km (Tiscareno et al. 2008), and their differential size distribution may be modeled as a steep power-law of index $q \simeq 6$ (Tiscareno et al. 2010).

Finally, from the analysis of Cassini UVIS stellar occultations, Baillié et al. (2013) reported the detection of a population of “ghosts” (small regions of low local optical depth, or “holes”) in the C ring and in the Cassini Division, which they believe are consistent with the depletion zones surrounding propellers. Their estimate of the upper limit of the particle size distribution is consistent with the existence of a population of icy particles of up to 12 meters in the C ring and ~ 50 m in the Cassini Division. These objects do not contribute significantly to the measured normal optical depth but may result in the “streaky texture” identified in the C ring by Tiscareno et al. (2019) in Cassini ISS images.

From the distribution of the ghost widths, Baillié et al. (2013) were able to model the size distribution of these boulders as a power-law with a differential index $q = 1.6$ in the C ring and $q = 1.8$ in the Cassini Division assuming the density of water ice. These power-law indices for objects between a few tens of meters and a few hundreds of meters are thus quite different from the estimated values for propellers in the A ring or for smaller ring particles. It is uncertain at present how the assumption of pure water ice for the ghost objects affects the retrieved size distribution, and further work in this area is needed. Ghost objects in the C ring and Cassini Division may represent the coherent shards of one or more consolidated objects that broke up to form the rings, as they exist well inside the Roche limit for solid water ice and are therefore unlikely to have accreted *in situ*. The increased abundance of non-icy material in the central C ring has been cited as additional evidence for the break up of a Centaur or other solid body (Zhang et al. 2017b, ; see also Sect. 5).

2.5 Ring Brightness Temperatures Measured by CIRS

The numerous radial scans of the main rings made with the Composite Infrared Spectrometer (CIRS; Flasar et al. 2004) FP1 detector have provided radial profiles of brightness temperatures, both on their lit and unlit sides (for a review see Spilker et al. 2018). The brightness temperature, which describes the temperature of a blackbody emitting the measured amount of radiation at a given wavelength, is a complex function of the ring’s 3-dimensional structure, particle properties such as spin state, Saturn’s season, the radius from Saturn (which

is a supplemental heating source), and viewing geometry. On the lit side of the rings, the brightness temperature generally decreases from the C ring to the A ring except for the Cassini Division, reflecting the decreasing flux from the planet. Saturn remains a significant source of heating for particles within the close, thin C ring (Spilker et al. 2013). The higher temperatures seen in the C ring and Cassini Division are additionally attributed to the albedos of the particles being lower in these regions, as well as to the lower optical depths in these regions that results in reduced particle mutual shadowing.

On the unlit side, the optically-thin C ring and Cassini Division rings appear hotter than the more opaque A ring, while the optically thick B ring is the coldest of all, reflecting the effects of mutual shadowing between the particles as well as the difficulty with which heat may be transferred across the ring plane (Spilker et al. 2006; Morishima et al. 2010). Any deconvolution of the properties of the ring particles and regolith grains from the brightness temperature profiles is therefore ring-model dependent.

Morishima et al. (2010) have derived the ring particle bolometric Bond albedo A_V as a function of Saturn distance, assuming a multi-particle-layer model that mixes slow and fast rotating particles. The albedo for the A and B rings is roughly constant, with $A_V \sim 0.55$, while the C ring albedo seems to decrease towards the planet from 0.4 to 0.1. In this study, the infrared emissivity was fixed to unity. Were the true infrared emissivity to be a bit lower, the fitted temperatures would favor lower albedos to reproduce a given observed temperature. Other thermal models for the C ring provide average values of about $A_V \sim 0.2$ (see Spilker et al. 2018), similar to but slightly higher than the value of ~ 0.15 derived from visible and NIR observations (Smith et al. 1981; Cooke 1991; Cuzzi et al. 2009). In comparison, the empirical slab model of Altobelli et al. (2014) yields an albedo $A_V \sim 0.45$ that is approximately constant with distance to the planet, albeit with large fluctuations.

If the apparently increasing albedo from the C ring to the A and B rings is real, a correlation between local optical depth and Bond albedo should exist. Such a correlation would be compatible with a darkening pollutant, such as one delivered by meteoroid bombardment, comprising a larger portion of the optically thin C ring (Cuzzi et al. 2009). At this stage, no thermal model has taken into account this variation of albedo in terms of pollutant fraction.

Radial variations in ring brightness temperatures may also originate from changes in emissivity that can stem from compositional or structural causes, such as a change in the regolith grain sizes covering the ring particles. Morishima et al. (2012) have investigated radial variations in regolith properties of particles, assuming grains are made of pure water ice. Any variation of ring emissivity versus distance has then been interpreted as due to variations in the size distribution of grains with distance (see Sect. 3.1).

2.6 Comparison to Ring Temperatures Measured by VIMS

The differences in albedo, optical depth, proximity to Saturn and regolith grain size discussed in the previous sections are the main cause of the temperature variation observed across the rings. While Cassini CIRS data directly measure the rings' brightness temperature, as discussed in Sect. 2.5, VIMS data permit an indirect measurement based on the spectral properties of water ice. Specifically, the position of the $3.6\text{ }\mu\text{m}$ continuum peak exhibited by crystalline water ice is temperature-dependent and can be determined from optical constants measured in the laboratory. As Mastrapa et al. (2009) have demonstrated, the imaginary part of the refractive index of crystalline water ice shows a change in its minimum around $3.6\text{ }\mu\text{m}$ for a range of temperatures between 20 and 150 K.

A similar behaviour has been observed by Clark et al. (2012) in reflectance measurements of small grains of pure water ice at standard illumination conditions (phase = 30°)

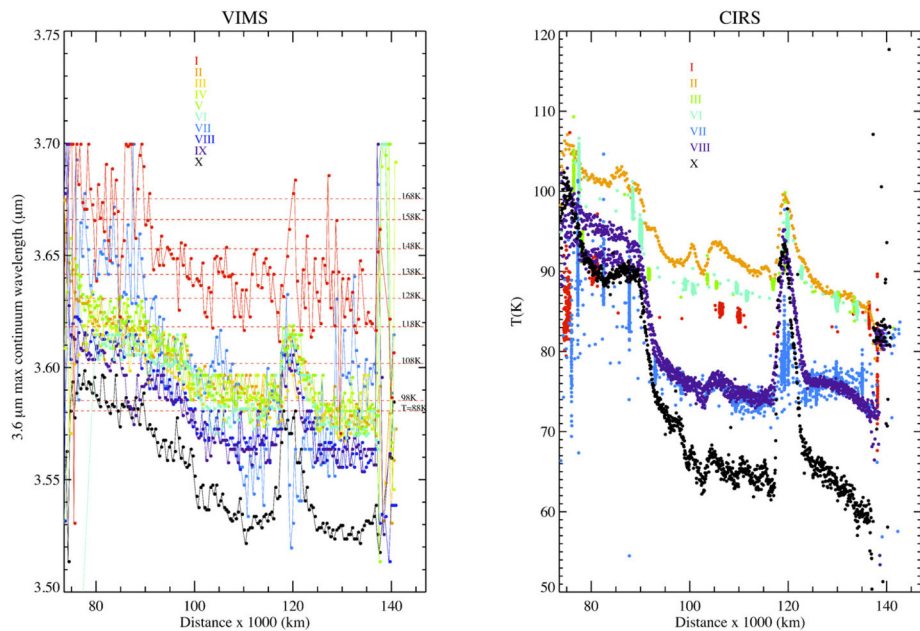


Fig. 5 Left panel: VIMS-retrieved $3.6\text{ }\mu\text{m}$ continuum peak wavelength and corresponding water ice temperature scale (horizontal dashed lines) for the 10 observations considered in Filacchione et al. (2014). From observation (I) to (X) the sub-solar latitude, or solar elevation angle, decreases from -23.5° to 2.6° . When the sub-solar latitude is negative VIMS observes the south face of the ring plane, (I) to (IX); when sub-solar latitude is positive, VIMS observes the north face, (X). Right panel: CIRS-retrieved ring's temperature during 7 of the 10 observations. For some CIRS observations, like in (VIII), the data shown are taken across two consecutive radial scans; this explains the differences observed across the C ring

for sample temperatures varying between 88 K and 172 K. By determining the wavelength of the $3.6\text{ }\mu\text{m}$ peak in reflectance, it is therefore possible to derive the temperature of the ice grains that are the main constituent of the ring particles. The $3.6\text{ }\mu\text{m}$ peak shifts towards shorter wavelengths when the ice is cooled, moving from about $3.675\text{ }\mu\text{m}$ at $T = 172\text{ K}$ to about $3.581\text{ }\mu\text{m}$ at $T = 88\text{ K}$ (Filacchione et al. 2016). By applying this method to ten VIMS radial mosaics of the rings sampled at 400 km/bin in the radial direction, Filacchione et al. (2014) derived radial profiles of the rings' temperature on the sunlit side as shown in Fig. 5. The observations were taken between 2004 near the southern solstice when the solar elevation angle B_0 was -23.5° , and 2010 near equinox ($B_0 = 2.6^\circ$), allowing tracking of the diurnal temperature changes over one half of the seasonal cycle.

Before equinox the south side of the ring plane was illuminated, while after equinox the sun shone on the north face. The maximum temperature was measured in 2004 when the solar elevation angle, B_0 , was at a maximum (observation I, red curve in Fig. 5). Ring particles cool down moving from southern summer to equinox. At equinox the solar rays are parallel to the ring plane and the particles receive the minimum solar illumination. As a consequence of this effect the peak's position shifts to shorter wavelengths and the minimum temperatures are observed across the rings (observation X, black curve in Fig. 5). When both solar and

antisolar ansae observations⁶ are available, such as in the two paired observations (V)–(VI) and (VIII)–(IX), it is possible to distinguish diurnal variations: on the two solar ansa (V and VIII), higher temperatures are measured than for the corresponding antisolar observations, (VI and IX). This effect is particularly evident in the C ring inward of 92,000 km. Since Saturn’s thermal emission is isotropic, a similar thermal behavior is probably the consequence of the cooling of the ring particles during the eclipse period.

While there is substantial agreement between VIMS and CIRS results across the A and B rings, VIMS systematically measures higher temperatures than CIRS across the C ring and Cassini Division. Several effects could explain this discrepancy. One possibility is that the deviation of the peak’s position in the presence of contaminants, in particular organics that have absorption bands in the 3.6 μm peak’s short-wavelength wing (see Sect. 3.2.3), may change the apparent position of the peak towards longer wavelengths. This would result in higher apparent temperatures. Notably, the C ring and Cassini Division are the regions of the rings where the amount of contaminants is larger, and where the assumption of pure water ice made to derive the temperature is less robust.

Alternatively, the difference in reported temperatures may be a consequence of the different skin depths l_λ sampled by the two instruments as a result of the wavelengths at which they operate. While VIMS is sensitive to very shallow depths a few microns from the outer surface of the particles, CIRS measures temperature at a greater depth, perhaps a few millimeters or even a centimeter in clean ice. In this case, VIMS may be measuring surface temperatures while CIRS retrieves volume temperatures. Indeed, the diurnal thermal inertia for the main rings is estimated from eclipse cooling data to be $\sim 10 \text{ J m}^{-2} \text{ K}^{-1} \text{ s}^{-0.5}$, with the lowest values in the Cassini Division. The corresponding thermal skin depth is on the order of 1 mm, greater than the characteristic VIMS penetration but less than that for CIRS (Ferrari et al. 2005; Morishima et al. 2011).

Overall, the comparison between VIMS’ “indirect” temperature measurements and CIRS brightness temperatures reveals that they show the same radial trends, with temperatures on the sunlit side increasing towards Saturn.

3 UV/Optical/IR Observations of the Main Ring Composition

Cassini UV and near-IR spectral data show that Saturn’s ring particles are predominantly made of crystalline water ice with minor contamination from non-icy materials (Cuzzi et al. 2009; Cuzzi, Filacchione and Marouf 2018a). While water ice is original to the rings, part of the non-icy materials that is responsible for the darkening and red-colored appearance at visible wavelengths is exogenous in origin. In this respect, when comparing the current composition of the rings with their original composition, one has to formulate some hypothesis about the ab-initio conditions proposed by the different formation scenarios, whether the rings are remnants of the Saturnian protoplanetary nebula or fragments of a destroyed moon or comet (Harris 1984; Esposito and De Stefano 2018). For example, rings originating in the protoplanetary nebula might be expected to contain some silicates and some volatile ices such as NH₃ or CO₂, while material tidally stripped from a differentiated icy satellite (Canup 2010) might be almost pure water ice. A disrupted comet might have a very different composition from a satellite’s mantle. The different ring formation scenarios are discussed in Sect. 5 of Crida et al. (2024, this collection).

⁶Here “solar ansa” and “antisolar ansa” refer to the ansa closer to the subsolar (or noon) and antisolar (or midnight) points respectively. The antisolar ansa is therefore closer to Saturn’s shadow, but both acquisitions are from the illuminated portion of the rings.

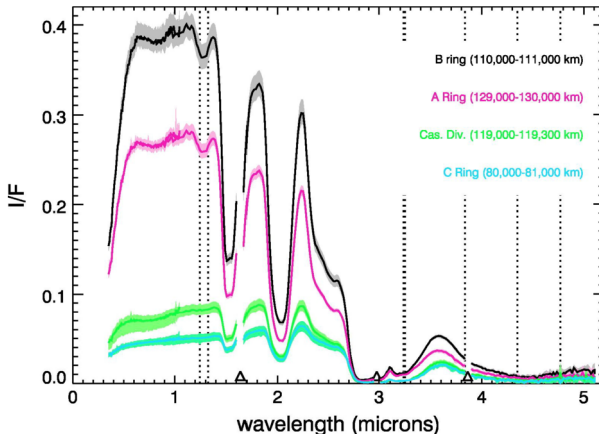


Fig. 6 Reflectance spectra of the sunlit side of the main rings of Saturn derived from Cassini-VIMS observations in 2005 at phase angles of $13 - 41^\circ$. Vertical dotted lines mark the locations of “hot pixels” in the detector with higher than average dark current, while triangles mark the locations of gaps in the order-sorting filter, where the spectral data are less secure and thus not plotted. The solid curves show the mean I/F spectrum for each region, while the shaded bands indicate the range of values observed in each of these locations. These ranges primarily reflect variations in the absolute brightness of the ring, rather than statistical uncertainties in the spectra themselves. Note the strong water–ice absorption bands at 1.25 and 2.0 μm , and the steep slope at wavelengths below 0.6 μm in the A and B ring spectra. Also note the variations in the spectral slope at continuum wavelengths between 0.6 and 2.3 μm among the different spectra. (From Hedman et al. 2013)

In Sect. 3.1 we discuss evidence for crystalline water ice as the dominant ring component, before turning in Sect. 3.2 to a description of endmember materials added to water ice (silicates and rocky material, carbon-bearing material and other ices) and their distribution across ring regions as derived from synergistic analysis and modeling of Cassini data. In Sects. 3.2.1 to 3.2.4 below, we describe spectral features that are observed in the data, as well as how these features have been interpreted in the context of radial trends and other associations with regions of the main rings. Modeling of the data is discussed separately in Sects. 4.1 and 4.2. The data and interpretations described in Sects. 3.2 to 4.2 are associated with spectra at nm to μm wavelengths, and constrain the surface composition of the ring particles. Regolith gardening processes may homogenize the particles on timescales of 1 Myr (Elliott and Esposito 2011). Data and interpretation related to the ring particle interiors are discussed in Sect. 5.

3.1 Water

The reflectance spectrum of the main rings from the near-UV ($\lambda = 0.30 \mu\text{m}$) to the near-IR ($\lambda = 5.2 \mu\text{m}$) is dominated by crystalline H_2O frost (Fig. 6), with typical grain sizes of a few tens to 100 μm (Clark and McCord 1980; Poulet et al. 2003; Cuzzi et al. 2009, 2018b; Filacchione et al. 2012, 2014). The comparative purity of the ice is supported by the very high albedo of the rings in the visible region, where $I/F \approx 0.5$ at low phase angles, as well as an extremely low albedo in the $2.7 - 3.1 \mu\text{m}$ region where water ice is strongly absorbing, and with the very strong absorption edge in the rings’ far-UV spectrum at $\sim 0.17 \mu\text{m}$ that is characteristic of fine-grained H_2O ice (Bradley et al. 2010, 2013).

Spilker et al. (2005) derived emissivity spectra for the A, B and C rings from CIRS data. Particles much larger than the observing wavelengths (16.7 to 1000 μm) were found

to dominate the spectrum for most of the FP1 spectral range, since the observed emissivity spectra appeared free of features within the error bars across this range. Of most interest, however, they found a clear roll-off in the averaged ring particle emissivity at frequencies below 50 cm^{-1} ($\lambda > 200 \mu\text{m}$) that they attributed to a combination of particle size effects along with the low absorption of pure water ice in this spectral region (see their Fig. 5 in particular).

The shape of the roll-off is sensitive to the size distribution and upper and lower size limits of ring particles, as well as the nature of the regolith that covers them. With a radiative transfer model making use of a four-stream calculation along with the delta-M method on a single layer with randomly-distributed regolith-free ring particles, Spilker et al. (2005) found that a size distribution with power-law index $q = 3.4$ reasonably fits the spectrum of the B ring. However, no robust analysis has been performed on the possible range of these parameters, nor on the fraction of contaminants in the water ice. Near the wavelength of the roll-off, the transparency of water ice makes the influence of sub-millimeter-sized water-ice particles apparent, but seems to preclude the presence of grains smaller than a few tens of micrometers. The fact that the CIRS results show the influence of sub-cm size particles so clearly, and that Cassini radio occultation results that sense only free-floating particles have larger minimum-particle-size cutoffs (Sect. 5), suggests that the spectral signature of sub-cm size particles seen in the CIRS data might actually be a manifestation of regolith emissivity, which Spilker et al. (2005) did not model.

Morishima et al. (2012) derived the spectral emissivity from a large number of spectra accumulated by the CIRS FP1 channel at various seasons and viewing geometries before the end of 2010. Good fits were obtained using pure water-ice and a power-law distribution of grain sizes ranging from $\sim 1 \mu\text{m}$ to 1 cm. For the main rings, they found that emissivity varies with ring temperature range (i.e. radial distance, season or phase angle). This observed emissivity is interpreted to be that of the regolith covering ring particles.

Despite many searches, there appear to be no unambiguous spectral indicators of other materials in the UV to near-IR spectral range (Cuzzi et al. 2009, 2018b), or in the mid-IR spectrum measured by the CIRS instrument (Edgington et al. 2008). However, the steep decrease in the main rings' albedo shortward of $\sim 0.6 \mu\text{m}$ — which is especially apparent in the A and B rings in Fig. 6, and leads to their distinctly reddish color at visible wavelengths (Estrada and Cuzzi 1996; Cuzzi et al. 2002) — is *not* characteristic of pure water ice. This is discussed further in Sects. 3.2.1 and 3.2.2.

Data from the Cassini-VIMS instrument have been used by several investigators to spatially map the variations in the purity, regolith grain size and even the temperature of the water ice. This is done using the relative depths of the water-ice bands at 1.55 and $2.0 \mu\text{m}$, the height and exact wavelength of the spectral peak at $\sim 3.6 \mu\text{m}$, and the average spectral slope between 0.35 and $0.55 \mu\text{m}$ (referred to below as the “UV slope”).⁷ Examples of such measurements are shown in the middle panel of Fig. 2, where it is apparent that the strengths of the water ice bands closely track the steepness of the UV slope. This has led to the interpretation that the material responsible for the UV absorption is embedded within the icy grains (i.e., it is an “intra-mix” in spectral parlance; see Sect. 4). However, the observed variations in band depth could be due predominantly to variations in the mixing ratio of the non-icy material or to systematic variations in the water ice grain size in the regolith (Cuzzi et al. 2009).

⁷The band depths are defined as $B_\lambda = (I_0 - I_\lambda)/I_0$, where I_0 is the average continuum intensity level outside the band, while the spectral slope is defined by $S = (I_{\lambda2} - I_{\lambda1})/I_0$. Here I_0 is the average intensity level over the interval $[\lambda1, \lambda2]$, and I_λ is the calibrated I/F at wavelength λ .

Overall, the strongest water-ice bands are found in the outer A and middle B rings, and the weakest in the C ring and Cassini Division. However, the transitions between these regions are much more gradual than might be expected, given the sharpness of the underlying transitions in optical depth. Across the C ring and in the part of the A ring beyond $\sim 136,000$ km there is a steady weakening of the ice bands and of the UV slope (Nicholson et al. 2008; Tiscareno et al. 2019).

3.2 Non-water Components

The primary spectral features that have been ascribed to non-water components are referred to as the “ultraviolet absorber” (Sect. 3.2.1) and the “neutral absorber” (Sect. 3.2.2). Since organic material is a significant component in the Cassini Grand Finale *in situ* ring measurements (Sect. 7.2.1) and different carbon-based materials have been hypothesized as the cause of these two sets of spectral characteristics, we discuss spectral evidence for organic material in the main rings further in Sect. 3.2.3. Finally, in Sect. 3.2.4 we briefly address the lack of evidence in the main rings for volatile ices such as CH₄ or CO₂, which were however both observed in the *in situ* data in the D ring region (Sect. 7.2.1).

3.2.1 Ultraviolet Absorber

Two competing explanations have been offered for the steep decrease in the main rings’ albedo shortward of ~ 0.5 μm (Fig. 6): the presence of small amounts of carbon or carbon-bearing material such as tholins within the ice grains (Cuzzi and Estrada 1998; Poulet et al. 2003), or the presence of nano-phase inclusions of metallic iron or iron minerals such as hematite (Fe₂O₃) or troilite (FeS) (Clark et al. 2012). These two models have very different cosmogonic implications (see further discussion in Sect. 3.2.3 below).

Iron metal or hematite, perhaps in the form of extremely tiny nanograins, has been proposed as a darkening and/or reddening agent (Clark et al. 2012). This suggestion has really only been made for the C Ring, which is far less red than the A and B rings (Sect. 4.2). Meteoroid bombardment and ballistic transport would predict that the C Ring is indeed more polluted by extrinsic meteoroids. However, radiative transfer models tend to find that carbon-tholin-silicate mixtures provide better fits to C ring spectra than iron metal or hematite (Sect. 4.2, Cuzzi et al. 2018b; Ciarniello et al. 2024).

While carbon-based materials therefore provide the better spectral fits, the Grand Finale data provide some new evidence for the presence of Fe-based materials in the rings. In analyses of CDA data from Cassini’s Grand Finale (see Sect. 7), Fischer et al. (2018) reported two distinct compositional populations: iron-rich grains (93% of them sulfides) providing more than half of the detections; and iron-poor grains (most of them silicates) providing less than half. A dynamical analysis of these detected grains, expanded upon by Trieloff et al. (2023), found that the silicate component plausibly derives from ejecta off the surfaces of Saturn’s retrograde irregular moons, while the iron sulfide-rich component is plausibly exogenous to the Saturn system. Iron sulfides and silicates have not been found to provide optimal fits to spectra of the C ring, and less so of the A and B rings. However, any measurement of the composition of non-icy material is of interest.

More recently, Linti et al. (2024) performed compositional analysis of silicate grains detected by CDA during the Grand Finale that were traced to the B, C, and D rings. They found that the compositions were homogeneous, independent of the source region, and that the grains were Fe-poor in comparison to chondritic materials, as well as in comparison to the Fischer et al. (2018) analysis. They suggest these results may point to chemical fractionation occurring in the rings that results in the small, Fe-poor silicate grains that were sampled, and larger, Fe-enriched grains that may not have been measured by *in situ* techniques.

3.2.2 Neutral Absorber

As noted above, the water-ice band depths in the C ring and Cassini Division are low in comparison with those in the A and B rings, as seen in Fig. 2. At the same time, the UV slope is shallower, which makes the rings' visible colors less red. These changes in the UV, visible and near-IR spectrum are accompanied by a decrease in the visual albedo in these same spectral regions that has generally been attributed to the addition of a spectrally-neutral absorber from an external source (Cuzzi and Estrada 1998). The higher concentrations of this material in the C ring and Cassini Division can then readily be explained in terms of these regions' lower mean surface mass densities and thus greater susceptibility to "contamination" by non-icy extrinsic material (e.g. Filacchione et al. 2014).

This neutral absorber has no specific spectral signature, but on cosmogonic grounds it has usually been identified either as carbonaceous material such as in carbonaceous meteorites or comets, amorphous elemental carbon from the *in situ* breakdown of accreted organic material, or perhaps silicates such as in stony meteorites. While most recent modellers assume this material is carbonaceous in nature, silicates remain a possibility. Future analyses of spectral data from the CIRS FP3 channel (9 – 17 μm) might permit detection of the characteristic emission or absorption features due to silicates in the 10 – 11 μm region, but will be challenging due to the relatively low ring temperatures and poor signal-to-noise ratio of these data (Edgington et al. 2008).

3.2.3 Spectral Evidence for Organic Material

The question remains whether the neutral absorber in the rings (and probably also the UV absorber) is predominantly some sort of carbonaceous material, perhaps in the form of tholins, polycyclic aromatic hydrocarbons (PAHs) or amorphous carbon; or a combination of silicates and oxidized iron. It seems likely that this journal can only be finally settled by analysis of *in situ* data such as that discussed in Sect. 7 below, but there are some additional remote sensing observations that bear on this journal.

In their study of Cassini VIMS spectra of the rings, which covered a wide range of phase, incidence and emission angles, Filacchione et al. (2014) reported a detection of the fundamental — but very weak — absorption bands due to CH bond stretching. The analysis, performed on a low phase ($\approx 6^\circ$), high signal-to-noise ring mosaic containing a statistically significant dataset ($> 8,000$ individual spectra), allowed the detection of faint aliphatic CH₂ bands at 3.42 and 3.52 μm (Fig. 7). Conversely, the other main spectral feature associated with organic matter and particularly with C-C or aromatic bonds in polycyclic aromatic hydrocarbons (PAHs) at 3.29 μm ,⁸ which was detected by VIMS on the dark terrains of Iapetus, Hyperion and Phoebe (Coradini et al. 2008; Dalle Ore et al. 2012; Cruikshank et al. 2007, 2008), is not recognizable in VIMS rings spectra. These aromatic features are thought to be produced in warmer, higher-energy environments such as the protosolar or proto-Saturnian nebula. This feature seems to be absent in the rings, though its proximity to the very strong water ice absorption at $\sim 3.0 \mu\text{m}$ makes any detection very difficult, if not impossible.

The detection of the aliphatic features across the rings and the absence of the aromatic band led Filacchione et al. (2014) to suggest an ultimate origin for this material in the diffuse interstellar medium where aliphatic bonds outnumber the aromatic ones (Pendleton and

⁸Dalle Ore et al. (2012) report the aromatic mode at 3.284 μm . The positions of the 4 aliphatic bands of CH₂-CH₃ symmetric-asymmetric are in fact not fixed, but have a small range of variability ($\sim 20 \text{ nm}$) depending on the specific molecule.

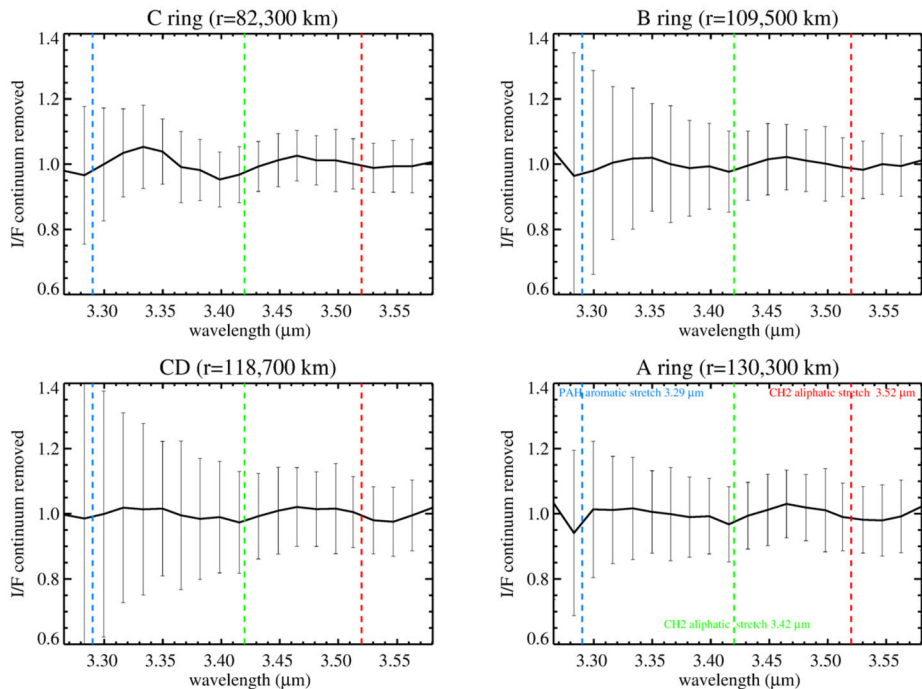


Fig. 7 Continuum-removed IR reflectance spectra by VIMS showing the two aliphatic hydrocarbon absorption features at 3.42–3.52 μm across the A, B, and C rings and CD. From (Filacchione et al. 2014)

Allamandola 2002; Raponi et al. 2020). Although seen in all major ring regions, the 3.42 μm band was stronger in the C ring and in the Cassini Division (Fig. 8), implying a likely association with accumulated exogenous, interplanetary debris that is now suspected to originate in the Kuiper Belt (Kempf et al. 2023). This spatial distribution matches very well with the quantitative spectral fits reported by Ciarniello et al. (2019), who found higher abundances of organics in the C ring and Cassini Division (see Tables 3 and 6).

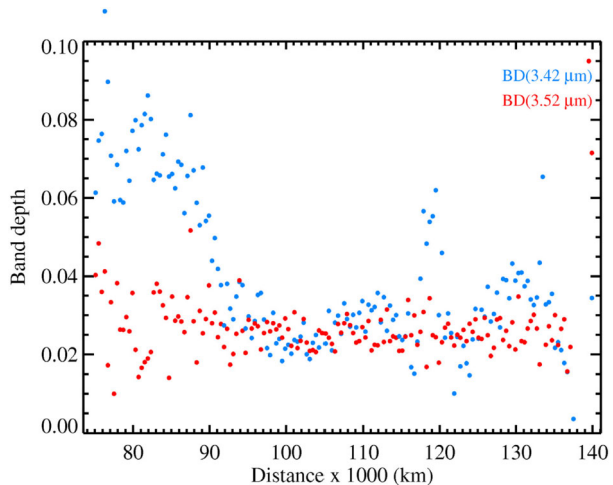
A careful study of the B ring by Clark et al. (2019), on the other hand, failed to find any evidence for an aliphatic band at the 0.2% level, after the co-addition of almost 22,000 individual VIMS spectra from regions selected to be uncontaminated by saturnshine.⁹ One way to reconcile these two observations, of course, is to attribute the CH band to the “neutral absorber” brought in by interplanetary bombardment. As noted above, this aliphatic material is more visible in parts of the rings with lower optical depths such as the C ring or Cassini Division, and much less abundant in the A and B rings.

3.2.4 Other Ices

Most common ices (*e.g.*, CO, CO₂, NH₃ and especially N₂ and CH₄) are too volatile to survive over geological timescales in Saturn’s rings. Of course, merely being volatile is no guarantee of escape from Saturn’s gravity field, but the gaseous species are likely to be photoionized and then effectively swept away into the magnetosphere on seasonal timescales

⁹Reflected light from the planet is dominated by strong methane bands, and thus carries an imprint of a similar C-H stretch feature at $\sim 3.3 \mu\text{m}$.

Fig. 8 Radial profiles showing the variability of the aliphatic hydrocarbon band depths at 3.42–3.52 μm . From (Filacchione et al. 2014)



(Cuzzi et al. 2009). The detection of other, less-volatile organic ices is again complicated by the presence of saturnshine, which imprints strong CH_4 bands in the rings' spectra except at large phase angles or at longitudes well beyond the terminator.

Nevertheless, CO_2 or NH_3 ice should be readily detectable, if they are present. Models of the near-UV spectrum suggest that there is very little or no NH_3 ice in the rings (Cuzzi et al. 2018b), while near-IR spectra of the rings show no sign of the strong CO_2 feature at 4.2 μm seen on Iapetus and several other mid-size icy satellites (Clark et al. 2012; Filacchione et al. 2014).

4 Regolith Radiative Transfer Modeling of the Main Rings

4.1 Overview of Regolith Radiative Transfer Modeling

Traditional regolith radiative transfer (RRT) modeling, following either Hapke (1993, 2013) or Shkuratov et al. (1999, 2005, 2012), treats regolith grains on the surface of a moon or an individual ring particle as independent, isolated scattering objects with some “single-scattering” albedo and phase function. The basic versions of these approaches presume the particles have no internal structure on scales of a wavelength; being internally uniform they are treated using some average real and imaginary refractive indices as a function of wavelength.

This approach has frequently been adapted to two similar-sounding regolith structures, which however have important differences from the standpoint of compositional interpretation (Fig. 9). One regolith structure is the so-called *intramixture* in which individual regolith grains are composed of some primary material with tiny embedded particles of different materials at sizes much smaller than the wavelength of interest. The refractive indices of these mixed grains are treated with Effective Medium Theory (for reviews and references see Bohren and Huffman 1983; Cuzzi et al. 2014a). On the other hand, a physical mixture of grains having multiple different sizes and/or compositions is called an *intimate mixture*, like salt and pepper or grains of sand on a beach. Traditional Hapke theory provides standard ways to treat this heterogeneous mix (Roush 1994; Hendrix and Hansen 2008), using an average grain albedo and phase function calculated and adopted for the entire mixture,

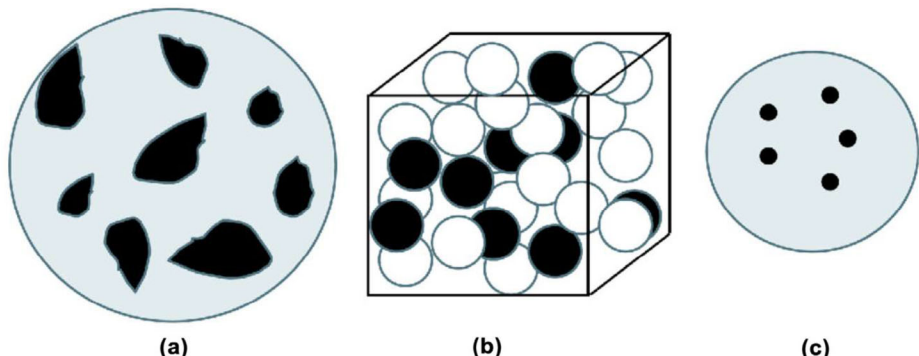


Fig. 9 Schematic diagram of different modalities for two-component mixtures. (a) areal mixture, blue circle represents instrument field of view; (b) intimate mixture; (c) intramixture, blue circle represents a single grain. From Ciarniello et al. (2011)

with different components weighted by their cross sections. RRT models can even include combinations of both kinds - an intimate mixture of grains containing different kinds of intramixtures (Cuzzi et al. 2018b). In the even more advanced adaptations these regolith grains can themselves have *internal scatterers*, distinct from any internal intramixed composition (Chap. 6 of Hapke 1993). The most basic assumption is that the regolith mixture has a single typical regolith grain size. However, multiple size distributions, different size distributions for different compositions, or other refinements are often incorporated, all at the cost of additional parameters (Poulet et al. 2003; Clark et al. 2012).

A complication of realistic RRT is that longer wavelengths may be insensitive to scattering by grains much smaller than the wavelength, instead selecting out grains (or clusters of grains) with size perhaps closer to the wavelength in question to interact most strongly with. This may be why RRT analyses often tend to infer “optimum” regolith grain sizes that increase with wavelength. For example, compare VIMS implications of particle size in Fig. 15.27 of Cuzzi et al. (2009) with those from UVIS analyses by Bradley et al. (2010). This effect is likely to be most important in the analysis of observations covering wide spectral ranges, from perhaps fractions of a micron well into the IR. Poulet et al. (2003) dealt with this problem by assuming a broad regolith grain size distribution, not unrealistic in general.

Intramixtures tend to maximize the absorbing power per unit mass of nonicy material. Grains of even strongly colored material that is highly absorbing (large imaginary index) can become totally absorbing over wide ranges of wavelength at fairly small sizes, suppressing any wavelength dependence (i.e. becoming less strongly colored). Tholins are good examples of this. While their imaginary indices are strong functions of wavelength through the visible and NIR, grains of the pure material quickly become so opaque that their characteristic reddish intrinsic color caused by strong wavelength dependence is lost if they are more than several microns in size. This drove Cuzzi and Estrada (1998) to adopt a tholin-in-ice intramixing model to fit the very strong redness of the A and B rings in Voyager imaging data. The same approach was used by Poulet et al. (2003), and Cuzzi et al. (2018b) still find that this approach provides the best fits to HST-STIS ring spectra.

Even for material with strong but wavelength-independent intrinsic absorption, large grains become so opaque at even small sizes that their darkening power becomes proportional to their surface area, not their volume, weakening the absorption per unit mass as

they get larger. An example of this might be seen in comparing the fraction of carbonaceous material in the rings (the so-called neutral absorber) inferred by Cuzzi et al. (2018b) using intramixtures (see Table 4) with the values inferred by Ciarniello et al. (2019) using intimate mixtures assuming 10-μm-radius grains (see Table 3). The fraction of nonicy absorber inferred by Ciarniello et al. (2019) is considerably larger than by Cuzzi et al. (2018b), probably because the assumed carbonaceous grain sizes of Ciarniello et al. (2019) are larger. Because inferences about the age and origin of the rings depend sensitively upon the fraction of nonicy material, these model-based uncertainties should be kept in mind.

One possible way to distinguish these different RRT hypotheses is to compare the above abundance inferences (both at visible and near-IR wavelengths, that sample only the very surfaces of ring particles) with cm-wavelength radiometry which samples the bulk of the ring particles. At the long wavelengths of microwave emission and scattering, intimate mixtures containing purely absorbing grains that are tens of microns or more in size behave like intramixtures. At present, the abundance of nonicy material over most of the rings inferred from 2.2 cm radiometry by Zhang et al. (2017a,b, 2019) seems to be closer to the results of Cuzzi et al. (2018b) than those of Ciarniello et al. (2019), possibly providing support for the lower fractions of nonicy material obtained from the intramixing model.

Finally, a recent wrinkle has emerged regarding ring RRT, that the planetary surfaces community has long been aware of: unresolved macroscopic shadows on/in the surfaces being observed make a surface look darker. If this effect is ignored, one infers an abundance of darkening material that is too large. It would not be unreasonable for ring particles, if they have a grape-cluster aggregate nature, to be even more strongly affected by this shadowing effect than other smoother surfaces. Hapke (1993, Chap. 12) has advanced a first-principles, geometrically-inspired, forward model along these lines, with several parameters. The role of shadowing in the rings context is also discussed by Cuzzi et al. (2017, see also references therein), where a simple one-parameter model is advanced to modify a basically Lambertian underlying smooth particle phase function. This simpler model turns out to be fairly similar in properties to the more complicated forward model of Hapke (1993).¹⁰

In the approach suggested by Cuzzi et al. (2017), the particle phase function is measured using observations over a wide range of viewing and illumination geometries. The shadowing behavior is manifested in the shape of the observed phase function, and this phase function defines the correction from the directly observed rough-surface, shadowed, effective ring particle albedo that rings analyses normally discuss, to a theoretical smooth-particle albedo with a Lambertian phase function and composition unbiased by shadowing. This is most easily done in low-optical-depth regions where multiple scattering is not a complication, but can be incorporated into a proper multiple-(ring particle) scattering model of arbitrary optical depth. The smooth particle albedo can then be modeled in terms of its underlying composition by the simplest forms of Hapke or Shkuratov theory. Of course, all of the above caveats apply as well to ring moon surfaces as to ring particle surfaces.

One prediction of this approach is that the shadowing parameter characterizing the observed particle phase function depends on the intrinsic, smooth-surface reflectance of the particle material - with particles appearing “smoother” at wavelengths where they are intrinsically brighter because shadows are filled in by nearby lit facets. A look at recent phase functions from icy moons provides some support for this hypothesis (Pitman et al. 2010), but more comparisons need to be done for the probably much craggier ring particles.¹¹

¹⁰As the Hapke model is parameterized assuming shadows are formed by craters, one might not expect the quantitative results (slopes) to be meaningful for clumpy aggregate ring particles.

¹¹An undergraduate class could test this conjecture in a large, empty, blacked out room with a flashlight and a light meter.

Along these lines, Cooke (1991) contains some carefully derived and highly relevant results, even if only in the Voyager clear filter. For example, the particle phase functions in all the outer C ring plateaux, and certain parts of the very inner C ring, are steeper (suggesting stronger shadowing, requiring a larger albedo correction) than the phase function in the mid-C Ring. The implications of this effect for the underlying intrinsic ring particle material is explored further in Cuzzi et al. (2024) using C ring regions intentionally chosen to be complementary to those of Cooke (1991) but covering Cassini UV3, BL1, and RED filters, as well as by Elliott and Esposito (2021) over all the rings using the basic Hapke approach.

4.2 Compositional Inferences from Modeling

Having described the approach, terminology, and caveats generally associated with spectral modeling in Sect. 4.1, we summarize here models of ring composition to date, as well as their primary conclusions. In one of the first attempts to apply a physics-based light-scattering model to the VIMS data, Hedman et al. (2013) modeled a selected subset of VIMS spectra using the 1D reflectance model of Shkuratov et al. (1999). Their principal results, shown in Fig. 10, indicate that while effective scattering lengths (a surrogate for grain size) are larger in the outer A and B rings than in the C ring or Cassini Division, the volume fraction of the UV absorber is in fact similar in the Cassini Division to that in the A and outermost B ring. The volume fraction of the UV absorber then increases monotonically inwards across the B ring, before decreasing again in the outer C ring. The above behavior supports the idea that the UV absorber is uniformly mixed with the water ice and is thus probably embedded within the icy grains, but also suggests that its volume mixing ratio generally increases with proximity to Saturn. In the Hedman models this component also appears to have a local maximum in the middle C ring, although some caution is appropriate here, as described below.

The model of Hedman et al. (2013) requires all the observed spectral properties to correspond to one of their three components: water ice, UV absorber, or neutral absorber. If the reality is more complex than three components, this approach may lead to analytical artifacts. For example, Fig. 14 of Cuzzi et al. (2002) shows very similarly increasing short-wavelength reddening inwards to the B ring edge, but nothing similar in the mid-C ring. Given the likelihood of excess non-icy material of *some kind* in the mid-C Ring (see Sect. 5), inclusion of an additional component in the model to account for rocky material may be more appropriate. Similarly, the Hedman et al. (2013) model ascribes a considerable amount of fine-scale photometric structure in the mid-B ring to grain size variations that affect spectral slopes. This approach of simplifying complex natural materials that may be present in the rings, such as chondritic grains, via modeling of a few key representative characteristics or pure components, such as amorphous carbon and silicates, is a common compromise that reproduces some features of the ring spectra within a more tractable parameter space. However, reality is more complex than any model, and there may well be other radial variations on those scales that became convolved into the grain size parameter.

The models shown in Fig. 10 confirm the much higher concentration of a neutral absorber within the Cassini Division and especially the C ring, where its volume fraction is 5–10 times higher than in the A and B rings. It is noteworthy that the abundance of the neutral absorber seems to increase monotonically inwards across the C ring, whereas the microwave measurements show a peak in the abundance of the nonicy material near the mid-C ring (Sect. 5), much like that of the UV absorber shown here. These two different radial trends may further support different origins for the UV and neutral absorbers, and a link between the UV absorber and the non-icy material from microwave observations. The models of

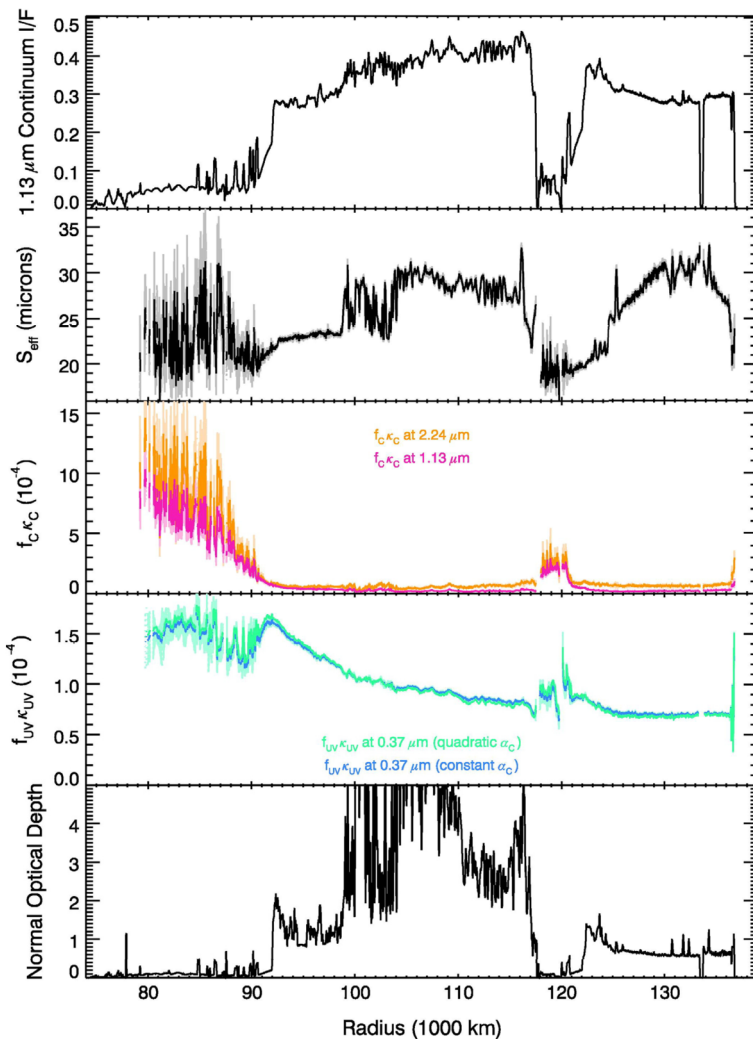


Fig. 10 Radial profiles of spectral parameters for the rings of Saturn derived from selected Cassini-VIMS observations and the 1D light-scattering model of Shkuratov et al. (1999). The upper panel shows the low-phase reflectivity of the rings at the continuum wavelength of $1.13 \mu\text{m}$. The second panel shows the effective scattering length in the regolith, which may be loosely interpreted as an average “grain size”. The third and fourth panels show the volume-weighted absorption coefficients of the continuum (or neutral) and UV absorbers, respectively. The lower panel shows an optical depth profile of the rings obtained from an occultation of the star γ Crucis, binned to 10 km resolution. (from Hedman et al. 2013)

Hedman et al. (2013) shown in Fig. 10 do not attempt to identify either the UV absorber or the neutral absorber, only their spatial variations.

Clark et al. (2012) pointed out the similarity between the dark regions on Iapetus and other satellites with properties of the C ring and Cassini Division in terms of the shape and central wavelength of the strong water ice band at $\sim 3.0 \mu\text{m}$ as well as the visible wavelength spectral slope. They suggested on the basis of this similarity that the best overall spectral fit, including the UV slope and infrared water bands, may be obtained with nano-scale inclu-

sions (i.e. an intramixture) of iron and/or iron-oxides, rather than the so-called “ice-tholins”. However, significant overall spectral and albedo differences between the satellites and the rings preclude any obvious similarities in the composition of even the C Ring, much less the A and B rings, with these dark regions (e.g. Figs. 15–34 and 15–37 in Cuzzi et al. 2009). In addition, recent spectral observations of the satellites in question actually find better fits from carbon-tholin mixtures than iron-hematite mixtures (Ciarniello et al. 2024). More recently, spectral fits to UV-visible STIS data from the Hubble Space Telescope that bridge the gap between the Cassini UVIS and VIMS datasets indicate that a good match to the steep UV slope seen in the A and B ring spectra can be obtained with tholins¹² embedded in fine-grained water ice (Cuzzi et al. 2018b). Attempts to fit this region of the rings’ spectra using nanophase iron-bearing materials were found to be unsatisfactory. These models are discussed further below, and illustrated in Fig. 13.

Additional clues as to the composition of the non-icy component(s) of the main rings are provided by more sophisticated modeling of the VIMS spectra of Saturn’s rings and moons based on Hapke’s theory of light-scattering in planetary regoliths (Hapke 2012). Ciarniello et al. (2019) showed that the main ring spectra can be reproduced by intramixtures of water ice grains with inclusions of organic materials providing the UV absorption (Titan tholins; Imanaka et al. 2004, 2012; West et al. 2014), intimately mixed with sub-micron water ice grains and a variable abundance of other compounds contributing as neutral absorbers, either in pure form (amorphous carbon or amorphous silicates) or embedded in water ice (nanophase hydrated iron oxides, carbon, silicates, crystalline hematite, metallic iron, troilite). Corresponding optical constants are shown in Fig. 11.

Given the lack of diagnostic VIS-IR features, the nature of the neutral absorber and its corresponding absolute volumetric abundance cannot be unequivocally determined remotely. The latter in fact depends on the particular compound selected and on the corresponding grain size. In this respect, the model VIS-IR spectrum of opaque and spectrally-bland materials is virtually independent of the grain size, provided they are large enough to completely absorb light passing through them. This prevents a robust grain size characterization, thus potentially biasing the inferred abundance of the corresponding compound.

Nonetheless, assuming a common composition and similar properties of the neutral absorber across the rings, results from spectral modeling can still be interpreted in relative terms. Keeping this in mind, Ciarniello et al. (2019) determined the abundance of the non-icy materials across regions of the main rings characterized by different optical depths, under the assumption that the neutral absorber is represented by 10-μm-size amorphous carbon grains. For the A and B rings the best unmixing fits were achieved by assuming intimate mixing of three types of grains: (1) water ice grains intramixed with tholins, (2) submicron (0.2 μm) water ice grains, and (3) carbon grains that are 10 μm.

For the C ring it is necessary to add a further population of water ice grains containing troilite intramixture inclusions in order to match the higher broad-band absorption and to introduce a positive continuum spectral slope across the whole VIS-NIR spectral range. Their findings are summarized in Table 3 and in Fig. 12, and indicate that the content of tholin increases inwards across the main rings, while the fraction of darkening materials (amorphous carbon and troilite) is anti-correlated with optical depth. (See Sect. 4.1 however, for a cautionary note about a possible role for on-particle shadowing in lowering apparent particle albedo.)

¹²Physically, the decrease in reflectivity is attributed to a $\pi - \pi^*$ transition in the carbon rings common in tholins and other PAHs (Jaffe and Orchin 1962; Clar 1964; Birks 1970; Salama et al. 1996; Malloci et al. 2004).

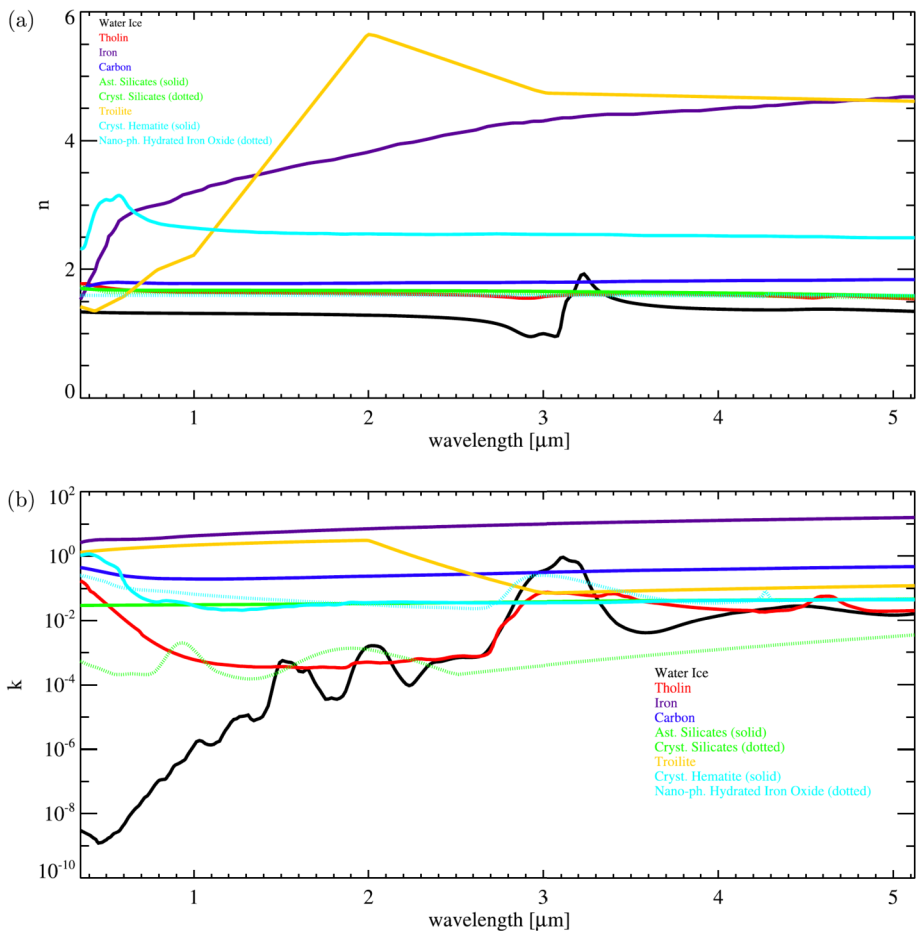


Fig. 11 Real (top) and imaginary (bottom) part of the refractive index of different materials used for ring spectral modeling. Note the decreasing absorption coefficient of water ice at shorter wavelengths, while those of tholins, hematite, and (to a lesser extent) carbon are rapidly increasing. From Ciarniello et al. (2019)

These results are consistent with the trends found by Hedman et al. (2013) for the UV and the neutral absorber, respectively (see Fig. 10). Also, the inferred size of the icy grains tends to be smaller in the C ring, in agreement with the scattering lengths or regolith grain sizes estimated by Hedman et al. (2013) and Filacchione et al. (2014).

The models discussed above were based entirely on VIS-IR data obtained by the Cassini-VIMS instrument that span the wavelength range $0.35 - 5.2 \mu\text{m}$. By extending such physical models for the ring particle reflectivity into the UV it is possible to derive further clues about the rings' composition, complementary to those obtained in the VIS-IR region. The near-UV spectral range, in fact, is very sensitive to the presence of chromophores, or UV-absorbers, including tholins, silicates, nanophase iron and amorphous carbon mixed with the dominant water ice.

Cuzzi et al. (2018b) fitted high-quality HST spectra of different ring regions using Hapke (1993) theory, with additional corrections made to take into account the shadowing effects caused by the particles' roughness (Cuzzi et al. 2017). Lacking such a correction, the shad-

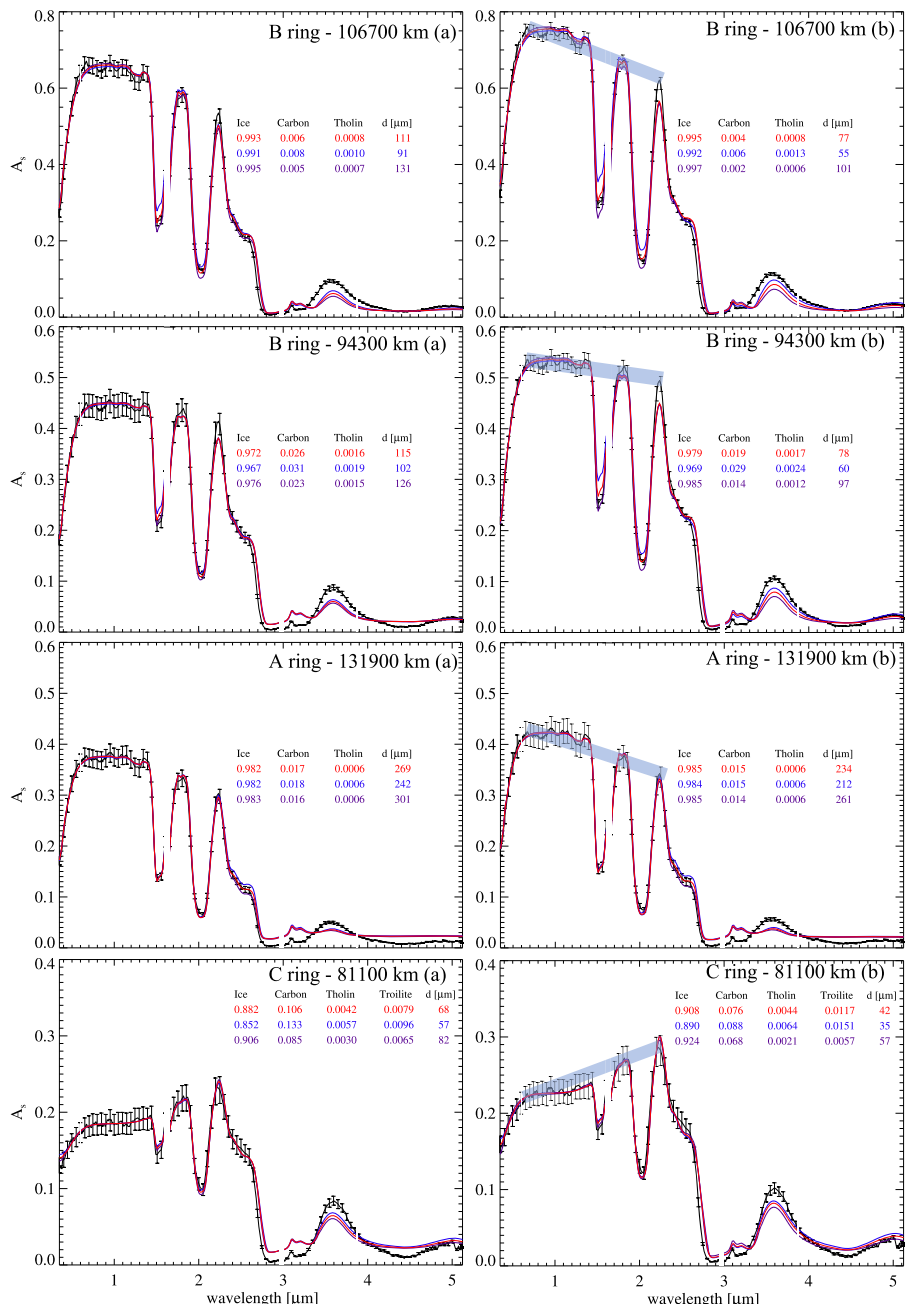


Fig. 12 Bond albedo spectra of Saturn's main rings derived from Cassini VIMS observations (black lines) and the best-fitting spectral models (red curve: best fit; blue and violet curves: models with accuracy comparable to the best fit). For each ring region two solutions for the Bond albedo spectra are shown (a, b), as resulting from ring photometric modeling performed in Ciarniello et al. (2019). Missing parts of the spectrum indicate instrumental order sorting filters. Note the positive continuum slope in the C ring between 0.6 and 2.3 μm , compared with the flat or blueish slope in the A and B rings, characteristic of mostly pure water ice. Adapted from Ciarniello et al. (2019)

Table 3 Inferred composition of Saturn's main rings from spectral modeling of VIMS data by Ciarniello et al. (2019). The models assume water ice grains with embedded tholin (ice-tholin intramixture) in intimate mixture with sub-micron water ice grains (0.2 μm size) and amorphous carbon grains (10 μm size). The C ring model requires an additional population of water ice grains with embedded troilite, whose size is assumed equal to that of the ice-tholin population (indicated as icy-grain size). The possible ranges in the total percentage of volumetric abundance of the different constituents are reported

Ring region	Radius [km]	τ	Carbon	Tholin	Troilite	Water ice	Icy-grain size [μm]
outer A ring	131900	0.6	1.39-1.78	0.061-0.063	-	98.15-98.54	212-301
mid B ring	106700	4.6	0.24-0.81	0.13-0.57	-	99.09-99.70	55-131
inner B ring	94300	1.4	1.42-3.08	0.12-0.24	-	96.73-98.46	60-126
mid C ring	81100	0.1	6.76 - 13.30	0.21-0.64	0.57- 1.5	85.18-92.45	35 - 82

Table 4 Total fractional abundances (F) of tholin, carbon and silicate by ring region. The total average abundance F_j for component j is given for different ring regions. F_j is the product of the volume fraction of grains containing component j , multiplied by the volume fraction f_j of pollutant intramixed within those grains. The range shown is inferred from best-fitting models across a wide array of different Hapke-based models that all fit comparably well. This systematic sensitivity testing provides a sense of the uncertainties in the spectral modeling results. Non-asterisked values come from the bulk of the simulations in which the grain size for each population is allowed to vary within a plausible range between 3–10 μm diameter. The grain size is constrained by the location of the UV edge (Bradley et al. 2010). Asterisked models assume all constituents have the same grain size; in general constant grain size models provide worse fits to the data. From Cuzzi et al. (2018b)

Ring	F_{tho}	F_{carb}	F_{sil}
A	$(4 - 10) \times 10^{-3}$	$(2 - 4) \times 10^{-4}$	$(0.5 - 7) \times 10^{-5}$
A*	9×10^{-3}	1.5×10^{-4}	1.6×10^{-3}
B	$(2.5 - 3) \times 10^{-3}$	$(0.5 - 3) \times 10^{-5}$	$(0.5 - 3) \times 10^{-5}$
B	1.2×10^{-2}	$(2 - 6) \times 10^{-6}$	$(0 - 1) \times 10^{-6}$
B*	8×10^{-3}	2.5×10^{-7}	1.9×10^{-3}
C	$(2 - 10) \times 10^{-3}$	$(5 - 15) \times 10^{-3}$	$(1 - 30) \times 10^{-4}$
C*	8×10^{-3}	2.6×10^{-2}	2.5×10^{-4}
C'*	7×10^{-3}	4.5×10^{-2}	2.0×10^{-4}

ows caused by the irregular surfaces of the ring particles darken the particle and can lead typical smooth particle models to overestimate the actual fractional abundance of darkening material. The main ring spectra were modeled with combinations of intimate and intramixture modalities of 10- μm -size grains made of water ice, amorphous carbon, tholins and silicates. Tholins appear only within a fraction (4 – 50%) of the water ice grains, arguing for a heterogeneous mixture. Here, HP and LP refer to High Pressure- and Low-Pressure formation regimes (Imanaka et al. 2004, 2012; West et al. 2014). The LP tholins tend to have more aromatic bonds and the HP tholins tend to have more aliphatic bonds (Cuzzi et al. 2018b). In general neither iron nor hematite, in nanoparticle form or in larger grains, was found to provide satisfactory spectral fits to the HST data for the A or B rings. Examples of the best fits from Cuzzi et al. (2018b) are shown in Fig. 13, while the corresponding model parameters are listed in Table 4.

Two fits are given for the B Ring, where we see that the tholin abundance can exceed one percent or so only if the amorphous carbon and silicates are both reduced to extremely low

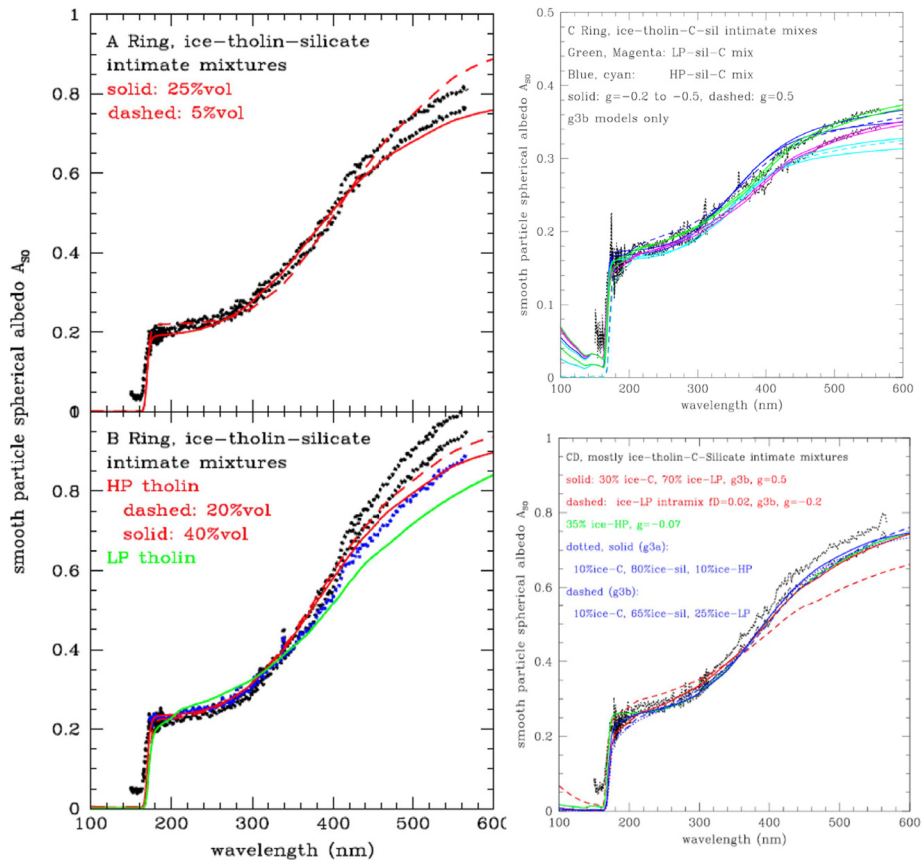


Fig. 13 “Smooth particle” Bond albedo of Saturn’s main ring (A, B, C, CD) particles derived from HST observations (heavy and light dotted curves, representing two different particle shadowing parameters) along with the best-fitting spectral modeling results (colored curves). Several variants of Hapke models are shown, to provide a sense of potential model-based uncertainties. The parameter g is the assumed regolith grain scattering asymmetry, with negative values referring to backscattering grains and positive values to forward scattering grains. Models denoted g3a and g3b are slightly different ways Hapke theory can be implemented. For details of the models see Cuzzi et al. (2018b)

levels. For the A ring, the upper limit of about one percent tholin also occurs only in models with almost no amorphous carbon. The main difference between fits with variable (A, B) and constant (A^* , B^*) regolith grain sizes is that the latter have more silicates — but still only a fraction of a percent. For the C Ring, the variable grain size model (non-asterisked) has much more silicate than do the corresponding A and B Ring models. Underneath the nominal C ring fit, we show two alternate fits with constant grain sizes for comparison with the A^* and B^* models: one for the nominal rough surface (C^*), and one where the particles are assumed to be smooth (C'^*). The latter needs more amorphous carbon (*i.e.*, darkening agent) than does the nominal case.

As noted above, the radial distribution of the neutral absorber (*i.e.*, amorphous carbon or silicates) supports an exogenous origin by meteoroid or cometary bombardment (Cuzzi and Estrada 1998), which more effectively contaminates regions of low surface mass density, while the radial trend of the UV absorber (tholin) may reflect an intrinsic origin (Cuzzi et al.

2018b). Alternatively, it may be derived from different parts of different precursor moons (Crida et al. 2024), or perhaps reflect indirectly the influence of Saturn's magnetic field.

5 Microwave Observations of Main Ring Bulk Composition

The UV, visible and near-IR spectra, of course, only sample the composition of the outermost layers of the decimeter to meter-sized particles in the main rings, which may differ from the composition of their interiors depending on how effective the mixing processes are (Elliott and Esposito 2011). In order to probe the interiors of the ring particles, and thus the bulk of the ring material, we must turn to the longer wavelengths of the rings' microwave emission spectrum, which penetrate many meters of solid ice because of its very low microwave absorptivity.

Early ground-based measurements in the 1970s showed that the rings' brightness temperature was quite low at wavelengths longer than a few mm, suggestive either of a very low absorption coefficient (and hence low emissivity) of the ring material, or of average particle sizes less than ~ 1 cm. The rings' very strong S-band radar reflectivity effectively ruled out the latter possibility, leaving the former. With its unusually low radio extinction coefficient, pure, cold water ice soon emerged as the most likely candidate (Pollack et al. 1973; Pettengill and Hagfors 1974; Cuzzi et al. 1980), subsequently supported by the strong water ice bands seen in the near-IR spectrum (Clark and McCord 1980). Interferometric observations by Grossman (1990) suggested a maximum non-icy mass fraction assumed to be silicates in the A and B rings of $\sim 1\%$, a value that is much lower than the bulk composition of any of the mid-sized saturnian satellites (or of any known solar system object). This surprising result was not challenged or improved upon until the Cassini mission 25 years later. The assumption that silicates are the only nonicy constituent is one of convenience; the microwave absorption properties of all other candidates are less well known. So, the microwave observations should be interpreted as constraining the total amount of nonicy material (silicates, organics, etc).

The radiometer channel of the Cassini RADAR instrument (Elachi et al. 2004) observed Saturn's rings at a wavelength of 2.2 cm between 2004 and 2008 with resolutions of order 2000 km, providing an ideal window through which to study the non-icy material fraction within the bulk of the ring mass. At 2.2 cm, the absorptivity of water ice is negligible compared to that of most non-icy materials, and thus the intrinsic thermal radiation from the ring layer is dominated by its non-icy components.

The Cassini radiometer observations show an exceptionally high brightness when the C ring is in front of Saturn, at near-zero azimuthal angles. Besides directly-transmitted planetary thermal radiation, a large portion of the scattered radiation by the ring particles must be in the forward direction, suggesting a high porosity of 70–75% for the C ring particles. The ring particles could achieve such a quasi-equilibrium, highly porous regolith as a result of a balance between frequent fragmentation and excavation of debris due to micrometeoroid bombardment, ballistic transport to relocate the debris more gently on other particle surfaces, and inter-particle collisions to compact the particles. Most regions in the C ring contain about 1–2% silicates by volume (Fig. 14; Zhang et al. 2017b). This composition can be converted into an exposure age between 10^2 to 10^8 years if the ring system is assumed to be initially pure ice that has been continuously contaminated by in-falling micrometeoroids (Cuzzi and Estrada 1998; Kempf et al. 2023). Such a calculation assumes that the C ring optical depth and surface density has not changed significantly during that time, and also that the present-day micrometeoroid flux is representative. This absolute time scale is inversely

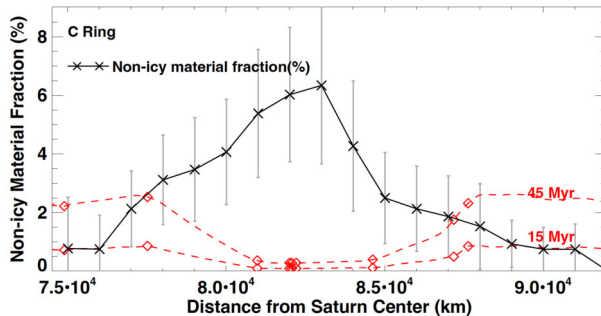


Fig. 14 The black curve shows the non-icy material fraction in the C ring derived from Cassini-RADAR observations. Red dashed curves show the predicted evolution of the non-icy material fraction over 15 and 45 Myr, assuming that meteoroid bombardment is the only source of contamination and that the meteoroid flux has remained constant over the past few tens of Myr. Red diamonds indicate the positions where opacity measurements have been made using density waves. The broad minimum in the predicted nonicy fraction is caused by the small opacities (high surface mass densities) observed in that part of the C Ring (Baillié et al. 2011; Hedman and Nicholson 2014). Figure from Zhang et al. (2017b)

proportional not only to the flux at infinity, but also to the amount of gravitational focusing by Saturn that the micrometeoroids experience before encountering the rings. See Sect. 2 of Crida et al. (2024, this collection) for a more extensive discussion of the exposure age, its relationship to the ring age, and associated assumptions.

An enhanced abundance of non-icy material is found in the middle C ring. Modeling of the middle C ring (Zhang et al. 2017b) reproduces the observed strong forward-directed scattering phase function as well as radially-variable thermal emission and low opacity (Hedman and Nicholson 2013; Zhang et al. 2017b) in the middle C ring when silicate material is included. Notably, the best fits are obtained when the silicate material is not well mixed with the water ice, but is instead present as large chunks in the cm to m size range, coated with porous icy mantles. In this case, the bulk composition may be on the order of 54 vol.% silicate. When the silicate material is instead modeled as volumetrically mixed with water, the non-ice component peaks at 6–11 vol.% at a radius of 83,000 km (Fig. 14; Zhang et al. 2017b). The significantly higher non-ice concentration in the middle C ring cannot be explained by direct meteoroid deposition alone. A possible scenario is that the entire C ring has been continuously polluted by meteoroid bombardment since it first formed, and the middle C ring includes additional contamination from a rocky body such as a Centaur that was broken apart by tidal forces. In this case, the spatial extent of the non-icy enhancement in the middle C ring suggests that the Centaur was likely to have been captured and integrated into the rings as recently as $\sim 10 - 20$ Myr ago (Zhang et al. 2017b).

Zhang et al. (2017a) found non-icy volume fractions of $\sim 0.3 - 0.5\%$ in the inner and outer B ring and as little as $\sim 0.1 - 0.2\%$ in the central region. For the A ring interior to the Encke gap, the derived non-icy volume fraction is $\sim 0.2 - 0.3\%$ everywhere. Finally, the Cassini Division has a non-icy fraction of $\sim 1 - 2\%$, similar to most regions in the C ring. The overall pollution exposure times calculated for the A and B rings and the Cassini Division from microwave constraints range from $\sim 30 - 150$ Myr, in line with the $\sim 15 - 90$ Myr derived for most regions in the C ring. For further discussion of the exposure age, see Sect. 2 of Crida et al. (2024, this collection).

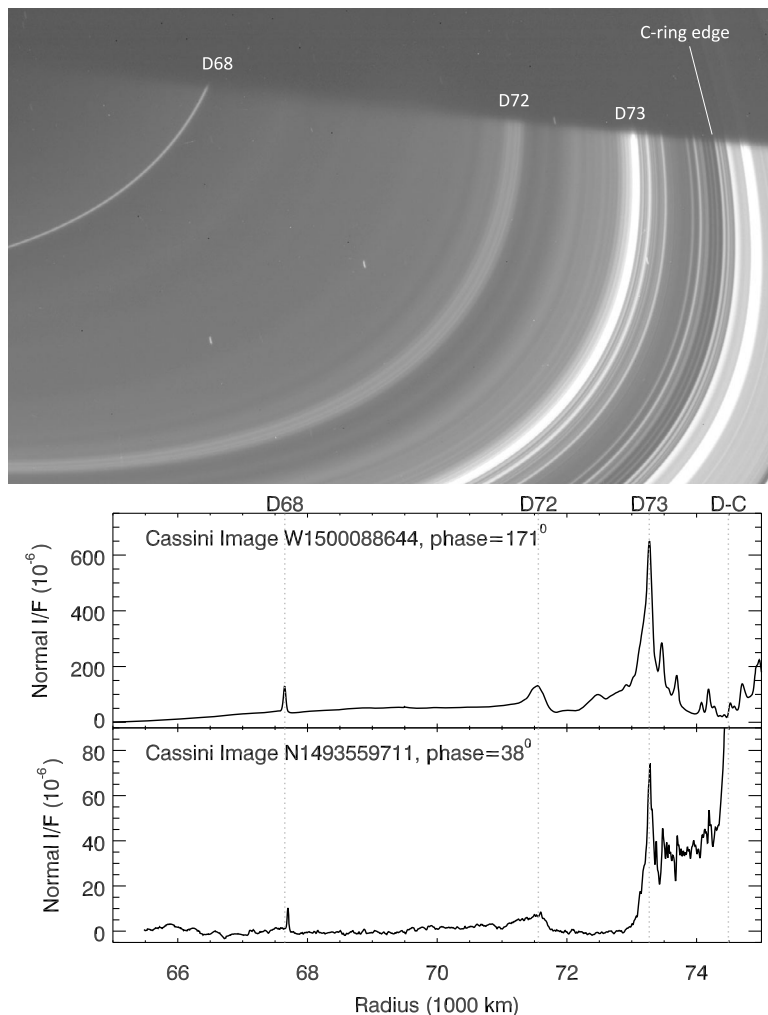


Fig. 15 Overview of the D-ring’s structure. The top image shows a Cassini image of the D ring obtained at a phase angle of 154° (N1541397571), while the bottom image shows radial brightness profiles of the ring from selected images obtained at high and low phase angles (adapted from Hedman et al. 2007a). In all cases, the locations of the three named ringlets and the inner edge of the C ring are marked

6 D Ring

Having reviewed the physical and chemical composition of the main rings, we now turn to the innermost D ring. The D ring is a relatively tenuous but complex ring that extends from the main rings down almost to the planet’s upper atmosphere. Any material coming from the main rings and entering the planet’s equatorial atmosphere must pass through this region, so the structure and composition of this ring is relevant to connecting the composition of the main rings with the material flowing into the planet.

Figure 15 provides a general overview of the D ring’s structure (Hedman et al. 2007a). The most prominent features in this ring are three ringlets designated D68, D72 and D73

after their distance from Saturn's center in thousands of km. Exterior to D73 there is a region that contains a collection of additional ringlets when viewed at high phase angles, but appears instead as a faint shelf of material when viewed at low phase angles. Meanwhile, D72 and D68 are surrounded by a broad, diffuse sheet of material that is only clearly visible at high phase angles. This diffuse sheet of material gradually fades interior to D68 with a scale length of order 1000 km and no distinct inner edge.

6.1 Constraints on Particle Size and Composition

Remote sensing data provide some constraints on the composition and typical particle size in the D ring, and are the only data source for the bulk D ring properties. The fact that all parts of the ring become brighter at higher phase angles implies that the majority of the visible particles are less than 100 microns across (Hedman et al. 2007a; Hedman and Stark 2015). Larger particles may exist in the region exterior to D73, which is both unusually bright at low phase angles and has a measurable optical depth in some stellar occultations (Hedman et al. 2007a). The sudden appearance of clumps in the D68 ringlet near the end of the Cassini mission provides indirect evidence that larger objects may reside within the ringlet (Hedman 2019; A'Hearn et al. 2021), but these objects have not yet been directly observed. Thus far, no evidence for larger particles has been uncovered elsewhere in the D ring. At the same time, sub-micron particles are very inefficient at scattering light at visible wavelengths, so there are at present no strong constraints on the distribution of such tiny particles within the D ring, a fact that should be kept in mind when assessing the *in situ* data from CDA, MIMI and INMS described in Sect. 7.2.

The small size of the visible particles in the ring limits the amount of compositional information that can be extracted from the remote sensing data. Fortunately, near-infrared spectra of the D ring obtained by VIMS do provide some useful constraints on the composition of this material. As shown in Fig. 16, many different parts of the D ring show a clear and deep absorption band around 3 μm due to water-ice. This indicates that water-ice is a major component of the D ring, as it is for the rest of the rings. The question then becomes how much non-icy material could be in this region.

It is reasonable to expect that the D ring contains a higher fraction of non-icy material than the main rings because the observed spectral trends across the main rings clearly indicates that the concentration of non-icy materials becomes higher closer to the planet (Hedman et al. 2013; Filacchione et al. 2014). We can place a rough constraint on the amount of non-icy material in the outer and middle D ring based on the observed depth of the very strong 3 μm ice band. This particular band is visible at high phase angles because the real index of water-ice approaches unity, thus inhibiting surface scattering. This dip becomes weaker if non-icy material is added to the particles because this tends to increase the real index away from unity.

Fig. 16 shows the predicted ratio of brightness between 2.9 μm and 2.5 μm for dielectric spheres computed from Mie theory¹³ as a function of particle size and composition for various mixtures of water ice and amorphous carbon. Note that the optical constants used for these calculations are obtained using measurements for water ice and amorphous carbon by Mastrapa et al. (2009) and Rouleau and Martin (1991), respectively, and the effective optical constants for the mixtures are computed using formulae from Cuzzi et al. (2014a). These calculations indicate that adding even 20% by volume of amorphous carbon to ice is enough to significantly change the depth of the ice band; this limit scales roughly proportionally with

¹³Readers are referred to van de Hulst (1981) for an introduction to Mie theory.

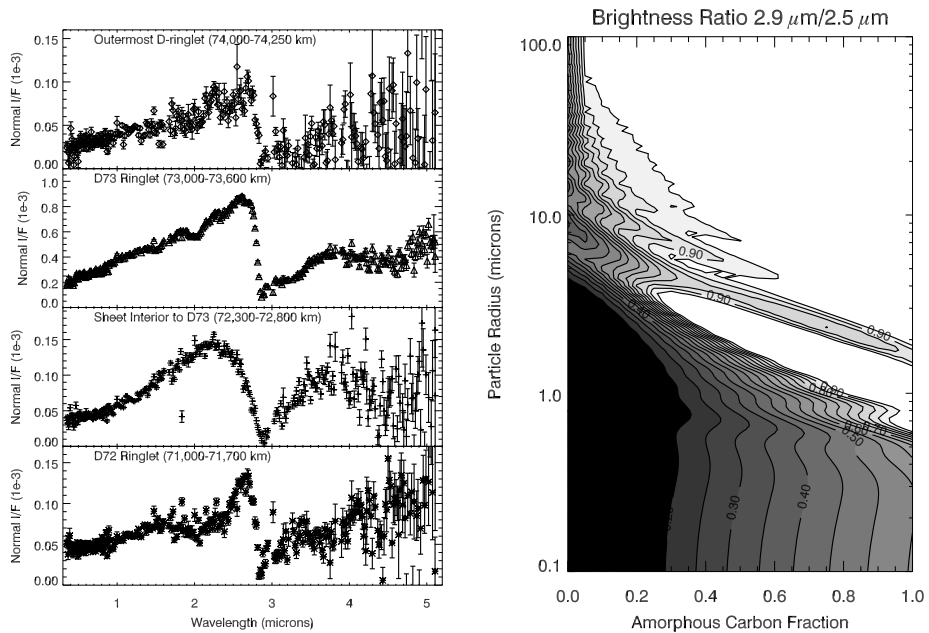


Fig. 16 Compositional information from near-infrared D-ring spectra. The left image shows spectra of various regions in the D ring derived from VIMS observations obtained at a phase angle of 167° (Hedman et al. 2007a). Note that all these spectra show a strong band at $3\text{ }\mu\text{m}$ due to the fundamental water-ice absorption band. These spectra have ratios for particle brightness at $2.5\text{ }\mu\text{m}$ and $2.9\text{ }\mu\text{m}$ that range between $R = 0.04$ and $R = 0.24$. The right panel shows as contours the predicted values for R as a function of particle size and composition assuming the particles are spheres with optical constants given by a mixture of water ice and amorphous carbon

the real index of the contaminant at $2.9\text{ }\mu\text{m}$. Thus the strength of these ice bands suggests that the material in at least the outer and middle D ring is still predominantly (≥ 80 vol.%) water ice. However, the ice-band strengths in the innermost D ring have not yet been analyzed in detail.

6.2 Evidence for Disturbances

Another important aspect of the D ring relevant for understanding the flow of material between the rings and the planet is that unlike the main rings, the D ring is time variable on time scales of years to decades (Hedman et al. 2007a). Between the Voyager flybys in 1980/81 and the arrival of Cassini in 2004 the structure of the middle D ring changed dramatically, with the brightest feature in the entire ring during the Voyager encounters (Showalter 1996) turning into a much more subtle feature 25 years later. During the Cassini mission, various parts of this ring were perturbed by sudden events, either impacts or temporal anomalies in the planet's magnetosphere (Hedman et al. 2007a, 2009, 2015; Hedman and Showalter 2016).

Finally, the innermost narrow feature in the ring, D68, developed a collection of bright clumps towards the end of the Cassini mission (Hedman 2019; A'Hearn et al. 2021). This localized brightening is most easily explained as the result of disruption of source bodies trapped in this region, releasing additional dust into the system. These sorts of changes could well have influenced the rate at which material flows from the rings into the planet.

7 Inflowing Material

During Cassini's Grand Finale orbits, the spacecraft passed between the inner edge of the rings and Saturn's upper atmosphere, to a depth of 1360 km above the 1 bar level. Initial expectations were that only Saturn's atmosphere would be detected by the suite of *in situ* instruments during these proximal orbits. As the spacecraft completed the proximal orbits, it became evident that an abundance of material was measured by the Ion Neutral Mass Spectrometer (INMS, Waite et al. 2004), the Magnetospheric Imaging Instrument (MIMI, Krimigis et al. 2004), and the Cassini Dust Analyzer (CDA, Srama et al. 2004) at or near the equatorial plane flowing into the atmosphere from the rings (Waite et al. 2018; Mitchell et al. 2018; Hsu et al. 2018). This chemically complex material included grains from nanometers to tens of nanometers in size, with mixing ratios that increased relative to the H₂ and He atmosphere with increasing altitude (Perry et al. 2018), supporting its origin exogenous to Saturn's atmosphere. Here, we review the current understanding of the material that has been observed flowing into Saturn's atmosphere from the rings, which breaks into two categories: ring rain at mid-latitudes coming in along magnetic field lines, and the equatorial inflow observed *in situ* by Cassini.

7.1 Charged Ring Rain at Mid-Latitudes

The first evidence for the flow of material from Saturn's rings into the atmosphere was measurement of ionospheric electron density profiles by Pioneer and Voyager (Kliore Astron et al. 1980; Tyler et al. 1981), which indicated a paucity of electrons with respect to the modeled densities (Waite et al. 1979; Atreya and Waite 1981). These previous chemical models required high electron densities to reproduce observations of long-lived H⁺ ions. The addition of charge-exchange reactions with water as an additional sink for H⁺ ions reduced the required electron densities and reconciled theory and data, leading to the identification of "ring rain" (Connerney and Waite 1984). Further analysis and modeling of this phenomenon identified that the main influx was due to movement of charged material along magnetic field lines, with deposition at mid-latitudes especially in the southern hemisphere (Northrop and Hill 1982; Connerney 1986; Ip 1983).

More recently, ground-based observations revealed that H₃⁺ ion emission in Saturn's atmosphere is latitudinally variable, with a symmetric pattern offset from the equator that maps along magnetic field lines to areas of the rings with greater optical depth, which was interpreted as additional evidence of ring rain (O'Donoghue et al. 2013). Moore et al. (2015) reproduced the observed H₃⁺ observations with an atmospheric chemistry model that includes a shifting balance between two loss pathways for H⁺: reaction with water or reaction with vibrationally excited H₂. This leads to a complex relationship between H₃⁺ and H₂O. Charge exchange with vibrationally excited H₂ produces H₃⁺, and competes with the water pathway for removal of protons, subsequently decreasing the electron density. This in effect slows the rate of loss of H₃⁺ by electron recombination. Combined with constraints on the electron density (Kliore et al. 2009) and haze latitudinal distribution (Connerney 1986), both of which are removed by water, O'Donoghue et al. (2013, 2019) utilized the H₃⁺ distribution to infer the presence and abundance of ring rain.

Notably, Cravens (1987) identified quenching with atomic H as a major loss pathway for vibrationally excited H₂, and photoionization of atomic H is a major source for H⁺ (Connerney and Waite 1984). Atomic H may play an important role in the inflow of ring material, including water, at the equator (Mitchell et al. 2018, see also Sect. 7.2 below). Observations of Saturn's Lyman-alpha brightness between 5°N and 35°N suggest that the mid-latitude

abundance of atomic H may be higher than current model predictions by a factor of two to three (Ben-Jaffel et al. 2023). Better understanding of the latitudinal distribution and source of atomic hydrogen may therefore be an important step forward for understanding the Saturn-rings system.

The Cassini Grand Finale orbits provided a unique opportunity to directly measure the mass flux and composition of ring rain particles, which includes the small fraction of high-speed ejecta from micrometeoroid impacts across the rings that can be charged and travel along magnetic field lines (e.g., Northrop and Connerney 1987; Ip et al. 2016). Measuring the flux of these nanograins plays an important role in constraining the rings' age, origin, and their remaining lifetime (discussed in more detail in Crida et al. 2024), as well as for understanding certain observed properties of Saturn's atmosphere itself.

During Cassini's Grand Finale, the CDA instrument detected inflowing grains with peaks in distribution in the northern and especially southern mid-latitudes when the instrument was pointed in the plasma-ram direction, as well as at the equator when the instrument was pointed towards the Keplerian-ram direction (Hsu et al. 2018). Mapping of this distribution along magnetic field lines to the B and C rings with the observed north-south flux asymmetry was interpreted as evidence that this material constitutes direct observation of charged ring rain.

One of the interesting aspects of this observation is that in general, many of the detected particles are composed of silicates, which is in contrast to the water ice-rich composition of the main rings from which they originated, with between 8 and 33 weight% silicate grains reported in the CDA data (Hsu et al. 2018). There are a few ways in which this may be explained: (a) The detected grains could be biased towards non-icy material by the nature of the high-velocity initial impact into the rings that charged the grains, perhaps because the ice resident in the ring particles is more easily vaporized and recondenses back onto shadowed ring surfaces or is reduced to grains too tiny for CDA sampling; (b) impact ejecta grains retaining ice could be larger or have slower ejection speeds, and could be more closely restricted to low latitudes that were not as well sampled by CDA; (c) photosputtering of icy-silicate ring ejecta could readily convert the water ice into vapor as the grains flow into the planet's atmosphere at high latitudes; or (d) CDA deadtime effects (Kempf 2008) could lead to biasing of the grain composition sampling during flux peaks.

These possibilities may be assessed by a parallel analysis of the total amount of water that is entering the planet's midlatitudes. CDA measured a total flux of nanometer-sized grains arriving at Saturn consistent with a mass-deposition rate (MDR) of $\sim 300 - 1200 \text{ kg s}^{-1}$, 70% of which fell near the midplane, and the remaining 30% ($\sim 100 - 370 \text{ kg s}^{-1}$) at the so called ring rain latitudes (Hsu et al. 2018). This water-depleted inflow is insufficient to explain the amount of charged water products needed ($\sim 430 - 2800 \text{ kg s}^{-1}$) to account for the observed latitudinal pattern of H_3^+ emission in Saturn's atmosphere (O'Donoghue et al. 2019). This may suggest that the water has been liberated from the observed grain population, and that this missing water is still somehow making it into the atmosphere, perhaps in vapor form. If one were to reconstitute the CDA grain population with sufficient water so that it were similar in composition to the inner edge of the C ring ($\sim 6\%$ non-icy by mass, see Fig. 14), this would give a lower bound of an additional $\sim 470 - 1750 \text{ kg s}^{-1}$ of water (Durisen and Estrada 2023) which is more consistent with the O'Donoghue et al. (2019) result.

This water liberation may be explained by photosputtering of the icy material *en route* from the rings to the planet. This rate can be simply estimated from the far-UV flux at Saturn (between 10–1200 Å) of approximately $10^{-3} \text{ J m}^{-2}\text{s}^{-1}$, scaled from 1 AU (Colina et al. 1996; Chadney 2017). A 20-nm-radius grain, the best-fit size for CDA data (Hsu et al. 2018), then

Table 5 Composition of inflowing ring material in weight percent. Values presented here compare deconvolutions from Waite et al. (2018), Miller et al. (2020), and Serigano et al. (2022) and are scaled to account for the effects of diffusive fractionation in Saturn’s atmosphere following methods from Waite et al. (2018). Organics (“Org”) are held constant for comparison

Reference	CH ₄	H ₂ O	NH ₃	CO	N ₂	CO ₂	Org
Waite et al. (2018)	16%	24.2%	2.4%	20%	20%	0.5%	37%
Miller et al. (2020)	9.0%	17.9%	3.6%	15.7%	16.4%	0.4%	37%
Serigano et al. (2022)	12.6%	16.6%	2.2%	15.2%	13.7%	2.7%	37%

receives about $5 \times 10^{-18} \text{ J s}^{-1}$. The latent heat of water is 2800 J g^{-1} so the energy needed to photosputter away a 20-nm-radius grain is about $0.9 \times 10^{-13} \text{ J}$, giving an exposure time of about five hours, comparable to the time the grain takes to wander along field lines into the planet’s upper atmosphere at ring rain latitudes (Hsu et al. 2018). The most likely effect of the CDA deadtime biasing the composition would be to increase the silicate/water ratio of the detected material. These numbers therefore may give an upper limit estimate to the amount of ring rain water that could be derived via this mechanism. Nevertheless, while additional work is needed it is possible that water ice is photosputtered off of icy ejecta grains, and is a significant source of Saturn’s mid-latitude ring rain.

7.2 Equatorial Inflow

In addition to the flow of charged material inward from the rings along magnetic field lines, neutral material from the inner edge of Saturn’s D ring can be decelerated by impacts with Saturn’s extended atmosphere, and subsequently deorbited (Mitchell et al. 2018; Perry et al. 2018). The highest influx of material observed during the Grand Finale was centered around the equator and measured by INMS, which detected masses across its full range from 1 to 99 unified atomic mass units (u; Waite et al. 2018; Miller et al. 2020; Serigano et al. 2020, 2022). This dataset provides a new window into the composition of Saturn’s rings, but there are some challenges to its interpretation. Cassini’s relative velocity compared to the inflowing ring material was approximately 30 km s^{-1} . This high velocity may have led to impact fragmentation of material entering the instrument, such that the measured masses may represent impact products of the ring materials rather than direct measurement of unaltered ring materials.

Furthermore, data on neutrals from INMS in this time period were collected using the closed source, which has a higher sensitivity but can lead to artifacts caused by interactions of incoming material with the instrument. Such effects include a time delay in detection of materials that adsorb more strongly to the surface, such as water. This effect leads to compositional fractionation, which requires recreation of the original composition via integration of the data from each orbit into a single composite mass spectrum (Magee et al. 2009). Finally, while ionization fragmentation can yield unique signatures for many compounds, convolution of those signatures leads to degeneracies that cannot be resolved with the unit mass resolution of INMS. With these caveats in mind, some important conclusions can still be drawn about the composition of the inflowing ring material.

7.2.1 Composition

The INMS measurements included gas, both from the rings and from the nominal H₂ and He atmospheric gas component, and volatilized fragments generated by dust impacting at

over 30 km s⁻¹ into the instrument's titanium antechamber surface. Unexpectedly, there was a high abundance of material heavier than He with identifiable compounds (CH₄, CO₂, CO/N₂/C₂H₄, H₂O, NH₃), as well as a host of organic fragments. Together, these compounds comprised a measured mass density of 1.6 × 10⁻¹⁶ g cm⁻³, as compared to the mean atmospheric mass density in this region of 4.7 × 10⁻¹⁵ g cm⁻³ (Waite et al. 2018). This material was measured at altitudes above the turbopause,¹⁴ and the presence of these heavy masses with increasing mixing ratios at higher altitudes indicates that they originate from material falling into Saturn's atmosphere rather than being atmospheric constituents (Perry et al. 2018).

Overall, the inflowing equatorial material was found to be quite water-poor in comparison to remote sensing constraints. By mixing ratio, water is still the single most abundant compound, comprising approximately 25 molar% of the material measured by INMS (Miller et al. 2020; Serigano et al. 2020), or an estimated 20 vol.% assuming all components have approximately the same porosity (Table 5). This is notably lower than the main ring composition, which is greater than 90 vol.% water (see Sect. 3.1 and Table 6). However, the D ring composition is also water-poor compared to the main rings (Sect. 6.1) as is the mid C ring (Sect. 5), and the overall trend suggests enrichment of non-water material moving inward through the rings. Other abundant compounds in the equatorial inflow include organics with fragments dominated by compounds with 4 C atoms and comprising between 10 and 20 wt.% (g per 100 g), CH₄ comprising approximately 10 to 16 wt.% of the INMS sample, NH₃ at 2 to 3 wt.%, CO₂ at < 3 wt.%, and CO, C₂H₄ and/or N₂ with a combined 20 to 30 wt.%.¹⁵

7.2.2 Evidence for a Gas-Grain Mixture

Based on comparisons of proximal orbits that crossed the ring plane (e.g. Rev290–292¹⁶) with the final plunge (Rev293) that did not pass through the ring plane, Miller et al. (2020) concluded that the inflowing material was latitudinally fractionated, with more refractory components depleted at higher latitudes (see their Fig. 3). They interpreted this as inflow of the more volatile components CH₄ and CO (or N₂) as gas, and the remaining, refractory components as grains, and estimated a gas to dust molar ratio of 0.7.

New analysis presented in this work of the scale heights of Saturn's atmospheric constituents and the major classes of inflowing material provides additional evidence for a gas-grain division (Fig. 17). Here, 15 u represents CH₄, 18 u represents H₂O, 28 u represents the combination of CO, N₂, and C₂H₄, 44 u represents CO₂, and 56 u is representative of organics. The scale height H and pressure P are described by

$$H = \frac{kT}{mg} \quad (6)$$

$$P = P_0 \exp\left(-\frac{z - z_0}{H}\right) \quad (7)$$

¹⁴The turbopause is defined as the vertical height in the atmosphere at which diffusion dominates over turbulent mixing.

¹⁵The INMS data cannot mass resolve CO, C₂H₄ and N₂. The confinement of the 28 u peak around the equator in high altitude proximals provides some evidence that more refractory C₂H₄ contributes to the 28 u counts (see Fig. 1b of Perry et al. 2018). Whether the remainder of 28 u material is dominated by CO or N₂ depends on the original source for the material. CO is much more abundant in cometary sources, for example.

¹⁶Here we refer to each different revolution around Saturn as a "Rev." Earlier literature on the Grand Finale dataset also uses the terms "Prox" for proximal orbit, or "Orbit"; these terms all refer to the same concept.

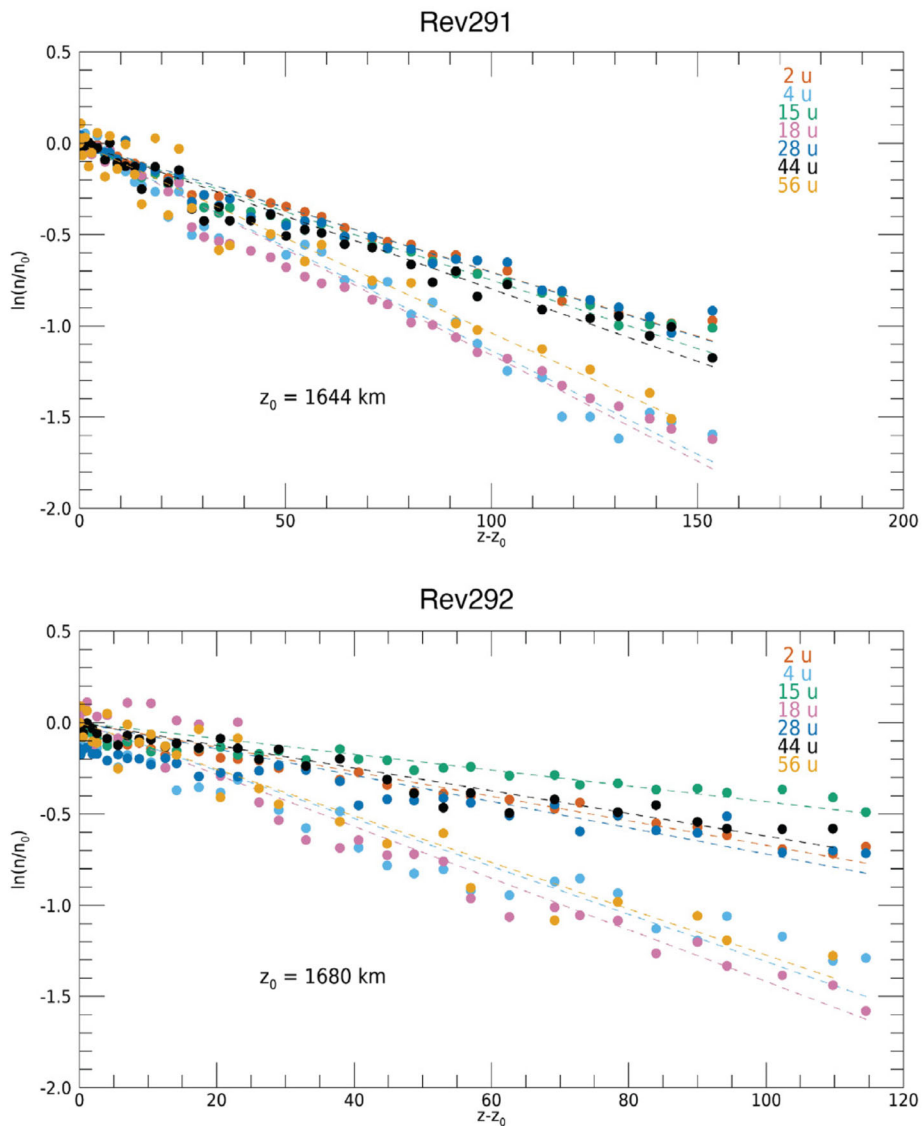


Fig. 17 Calculated scale heights for marker masses for atmospheric H₂ (2 u) and He (4 u), as well as for inflowing CH₄ (15 u), H₂O (18 u), CO/N₂/C₂H₄ (28 u), CO₂ (44 u), and organics (56 u). Symbols show measured density values, and dashed lines show linear fits to the data. The different scale heights for H₂ and He are evidence that the measurements are made above the turbopause where diffusion velocity dominates. The different scale heights between volatile and refractory inflowing masses suggests that refractory materials are falling more rapidly because of contributions from grains

where k is the Boltzmann constant, T is the temperature, m is the compound mass, g is the gravitational acceleration, and z is the altitude. While scale heights calculated from the slope of the dashed fits in Fig. 17 match within formal uncertainty (which is not shown for visual clarity), two separate trends or groups are visible. The scale heights for H₂ and He differ by a factor of 2 (~ 140 km versus 70 km), matching the $2\times$ mass difference between the com-

pounds. This provides confirmation that the measurements are taken above the turbopause, where the scale height for upward-moving material becomes mass-dependent. Masses in the downward-flowing material that have been associated with the gas phase (Miller et al. 2020) have scale heights that are most similar to the bulk atmosphere (H_2). This suggests diffusive coupling of these gases with the atmosphere; that is, the downward velocity of the gases is controlled by the rate of diffusion through H_2 because the gas-phase inflow is strongly coupled with the atmosphere. Masses that have been associated with grains of less-volatile material (18 u and 56 u; Miller et al. 2020) have scale heights that are smaller than the bulk atmosphere. This may indicate that these masses are not yet coupled to the bulk atmosphere at the altitudes measured, and are falling at higher velocities in the form of grains.

The presence of inflowing grains is further supported by analyses of the Langmuir probe (LP) dataset. Johansson et al. (2022) modeled secondary emission produced by high velocity impacts of water vapor molecules on the Langmuir probe, and derived a median mixing ratio for gaseous water molecules of 10^{-5} . This value is approximately an order of magnitude lower than the water mixing ratio reported by Waite et al. (2018), suggesting that the majority of water measured by INMS may be present as grains.

Ionospheric chemistry also points towards the presence of grains in the equatorial inflow. Photochemical modeling identifies loss processes for H^+ and H_3^+ via reaction with a heavy compound M, which may be CH_4 or H_2O (Cravens et al. 2019). The modeled mixing ratio for M, f_M , is the same order of magnitude as the mixing ratio measured by INMS for water. At higher latitudes, f_M increases, while the equatorial region is dominated by a second heavy compound R that reacts with H_3^+ but not H^+ . N_2 and CO are suggested as candidates for R. While the photochemical model of Cravens et al. (2019) therefore also supports latitudinal fractionation, the higher abundances of volatile CO and/or N_2 at the ring plane are contrary to the findings of Miller et al. (2020). However, the modeled reactions are for gas-phase compounds, and the depletion in f_M at the equator may be explained by retention of most water in grains at lower latitudes, while CO and/or N_2 may be in the gas phase at all latitudes.

This explanation is consistent with further modeling by Vigren et al. (2022), who consider the role of grain charging in this environment. Their model results require higher mixing ratios of M-type molecules and lower mixing ratios of R-type molecules than reported by Miller et al. (2020). Similar to Cravens et al. (2019), their photochemical model considers reactions of gas-phase water with H_3^+ and H^+ , but does not include solid-phase water in icy grains. Vigren et al. (2022) report that the number density of grains required by their model is approximately equal to the difference between the number of positive ions, n_i , and the number of electrons, n_e . This difference is greater at lower latitudes, which may be suggestive of an increased grain population near the equator. They suggest an upper limit of ~ 40 ppm for M, and compare this to the 200 to 400 ppm abundances reported by Miller et al. (2020). This may suggest a molar gas to dust ratio for M molecules on the order of 40:200 (0.2) to 40:400 (0.1) if the grains are dominated by water ice, somewhat lower than the value of 0.7 estimated by Miller et al. (2020).

Modeling of Saturn's atmospheric chemistry by Moses et al. (2023) suggests that the physical state of the inflow as a gas-grain mixture rather than as gas only is significant for interpretation of the inflow timescales; see Sect. 7.2.4. Additional work to understand the distribution of gas and grains in the inflowing material is needed.

7.2.3 Comparison of Mass Deposition Rate Derivations

In situ measurements by Cassini captured instantaneous compositional snapshots of parcels of Saturn's atmosphere along each proximal orbit. To determine the mass deposition rate

Table 6 Comparison of ring compositions via in situ and remote sensing measurements. Remote sensing values summarize the upper and lower limits for non-water and water ice components respectively. In situ compositions include the average value from deconvolution results in Serigano et al. (2022) and Miller et al. (2020). Other ices includes NH₃ and CO₂. Gas includes CH₄, N₂, and CO. Rocky material includes silicates and troilite

	In Situ			Remote Sensing						
	INMS inflow		SUDA inflow	D ring ^a		C ring edges ^b		C ring mid ^c		B ring ^d
	molar%	weight%	volume%	weight%	volume%	volume%	volume%	volume%	volume%	volume%
water	24	16	31	67-92	87-97	>80	>92	>75 ^h	>95	>92
organics	34	50	55	—	<20	<6	<14	<4	<6	<2
other ices	11	8	14	—	—	—	—	—	—	—
gas	30	26	—	—	—	—	—	—	—	—
rocky	—	—	—	8-33	3-13	—	<2	<54 ⁱ	<1	<1

^asee Sect. 6

^b(Cuzzi et al. 2018b; Zhang et al. 2017b); away from the central, anomalous peak (see Fig. 14)

^c(Zhang et al. 2017b; Ciarniello et al. 2019)

^d(Cuzzi et al. 2018b; Zhang et al. 2017b; Ciarniello et al. 2019)

^equantitative constraints from Zhang et al. (2017b), plus similarity to C ring from Hedman et al. (2013)

^feffectively molecules per 100 molecules

^ggrams per 100 grams

^hfrom measurement techniques that probe the surface

ⁱfrom measurement techniques that probe the bulk volume

(MDR) required to produce these measured compositions, the downward velocity of ring material traversing through each parcel and the total surface area represented by each parcel must be constrained. To date, there are five reported calculations of a large equatorial mass influx of ring material based on data from Cassini's Ion Neutral Mass Spectrometer (INMS; Waite et al. 2004), including two different methods and three independent calculations (Waite et al. 2018; Perry et al. 2018; Yelle et al. 2018; Serigano et al. 2020, 2022). The results are summarized in Table 7. Calculations based on measurements by the MIMI Ion Neutral CAmera (INCA) of the equatorial influx (Mitchell et al. 2018), and by CDA of grains at the equator as well as at mid-latitudes are also included (Hsu et al. 2018). Ground-based measurements from the Keck telescope constraining the mass influx of charged water at mid-latitudes from modeling of H_3^+ densities are provided for comparison (O'Donoghue et al. 2019).

MIMI detected high energy impacts of large molecules in a tight band with a half width of +/- 1.4 degrees centered around the equator, when the spacecraft was moving through the upper atmosphere at a relative velocity of greater than 30 km s^{-1} . Particles were found to have a limited mass range greater than $1 \times 10^4 \text{ u}$. Assuming a mass density of 1 g cm^{-3} for the grains, the inferred particle sizes range from 1.6 to 2.5 nm. MIMI's INCA sensor detected a dust number density of 0.1 cm^{-3} (Mitchell et al. 2018). Utilizing terminal velocity from their model of collisional deceleration of dust grains (2.5 km s^{-1} at an altitude of 3000 km), and assuming a grain size of 15,000 u, Mitchell et al. (2018) scale the measurement for regions within 1° latitude of the equator to calculate a grain MDR of 5 kg s^{-1} .

The MIMI value is several orders of magnitude lower than the MDR calculated from INMS data, and the values do not appear to be reconcilable via reasonable adjustment of the model parameters. The MIMI influx calculation scales approximately linearly with grain mass. Use of the terminal velocity yields the upper limit for mass influx, and choice of a different altitude consistent with the same atmospheric model would lead to lower values for the MDR. Imposing a $10\times$ increase on the atmospheric H density leads to a $3\times$ increase in the mass influx. The most likely explanation may be measurement by the two instruments of different grain populations based on size (Perry et al. 2018), discussed further below.

INMS data are dominated by signal at the lowest altitudes, where ring material is diffusively coupled to the atmosphere, e.g. below 1700 km. Therefore, in the Waite et al. (2018) calculations of influx rate, diffusive velocities¹⁷ are used rather than terminal velocity. Measurements are still made above the turbopause, where diffusion dominates over turbulent mixing; this is evidenced by the different scale heights measured for H₂ and He (Fig. 17; see also Fig. 3 of Waite et al. 2018).

Waite et al. (2018) base their velocities off of bounding limits for the downward velocity of methane, with the lower limit (45 m s^{-1}) given by the limiting flux approximation, and the upper limit (100 m s^{-1}) adapted from a simple hydrostatic model (Bell et al. 2014). Velocities for different compounds are then scaled using diffusion coefficients (Mason and Marrero 1970) for each of the major molecular components identified by INMS. These velocities are much lower than the terminal velocities utilized by Mitchell et al. (2018). Note that using higher velocities at the same altitudes would imply higher mass influxes to explain the observed mixing ratios for inflowing material. The Waite et al. (2018) calculation uses a wider spread of the material than Mitchell et al. (2018) at 4° north and south of the

¹⁷“Diffusive velocities” are defined from a simplified diffusion equation, which is easily seen to be just a rearrangement of terms in equation (9) to $F_i = D_i(X_i N_{H_2}/H_i)$ where the term in parentheses approximates a vertical gradient. The same equation can then be written as $F_i = (D_i/H_i)X_i N_{H_2} \equiv v_D N_i$ where $v_D = D_i/H_i$ is thereby defined as the diffusive velocity, multiplying the local number density.

Table 7 Mass deposition rates (MDR) calculated for inflowing material measured during Cassini's Grand Finale. Inflows are categorized as mid-latitude ring rain ("Mid") or as equatorial inflow ("Eq")

Reference	Dataset	Material included	MDR (kg/s)	Latitude	Notes
Waite et al. (2018)	INMS	Volatiles + nanograins	4800 - 45000	Eq.	
Perry et al. (2018)	INMS	Volatiles + nanograins	4000 - 30000	Eq.	Altitudes and velocities comparable to MIMI (Mitchell et al. 2018)
Perry et al. (2018)	INMS	Volatiles + nanograins	10000 - 200000	Eq.	Sedimentation velocities, and mid-altitudes comparable to Waite et al. (2018), Yelle et al. (2018)
Yelle et al. (2018)	INMS final plunge	CH4	1300 - 11000	Eq.	Here we assume 10^{10} km^2 surface area for comparison
Serigano et al. (2020)	INMS	CH ₄ , H ₂ O, NH ₃	1390 - 9380	Eq.	
Serigano et al. (2022)	INMS	All compounds	19700 - 80600	Eq.	Following Yelle et al. (2018)
Mitchell et al. (2018)	MIMI	Particles 10,000 to 40,000 u	5.5	Eq.	Some evidence for flow of charged material on magnetic field lines
Hsu et al. (2018)	CDA	Grains	224 - 854	Eq.	
Hsu et al. (2018)	CDA	Grains	100 - 370	Mid	
O'Donoghue et al. (2019)	Keck telescope	Water	432 - 2870	Mid	Based on models of observed H ₃ ⁺ densities

equator, based off of the half-width for INMS counts. The mass influx numbers calculated over three separate orbits ranged from 4800 to 45,000 kg s⁻¹ of infalling material at masses heavier than the H₂ and He atmospheric compounds (Waite et al. 2018). The mass influx variation from orbit to orbit differs by 2.5, while differences from the two bounding cases for velocity are a factor of 3.8; uncertainty in velocity contributes more strongly to the range of values reported.

Similar influx estimates (10,000 to 200,000 kg s⁻¹ for the mid-altitude range) were determined by Perry et al. (2018), with velocity estimates calculated based on Epstein drag:

$$v_s = \frac{0.36\rho_p g(2a)}{m_{H_2} n_{H_2} v_{H_2}} \quad (8)$$

where v_s is the sedimentation velocity, ρ_p is the particle mass density, g is the gravitational acceleration, a is the particle radius, and v_{H_2} , n_{H_2} , and m_{H_2} are the mean thermal speed, number density, and mass for atmospheric H₂. They calculate velocities at 1700 km of between 3 and 30 m s⁻¹. Perry et al. (2018) also report that use of INMS data at altitudes (3000 km) and terminal velocities (1 to 3 km s⁻¹) matching the method and region used for the MIMI MDR result in a ~ 50% reduction in the calculated INMS MDR. However, this method still results in an exceptionally high inflow rate, and at the higher altitudes it is likely that material is undercounted in the INMS dataset because of the lower signal to noise ratio.

Perry et al. (2018) concluded that the MDR discrepancy between MIMI and INMS was best explained by the size distribution of the infalling material, with a peak near a mass of 500 u and INMS measuring the smallest grains. Such small grains may be more likely to avoid sublimation (Hamil et al. 2018), consistent with the minimal effects observed on atmospheric chemistry (Moses et al. 2023). These data imply an extremely steep size distribution if the INMS and MIMI grains are derived from the same population. However, the physical process of deorbiting ring material via collisions with atmospheric gases (Mitchell et al. 2018; Perry et al. 2018) is likely to fractionate the original grain population as a function of grain radius a . While grains with a larger radius are more likely to have collisions with atomic H (an a^2 dependence), the greater momentum of grains with higher mass may require more collisions to deorbit (an a^3 dependence). Further work is needed to understand the relationship between size distribution of the measured material, the size distribution of the source material in the D ring, and any connection to the main rings e.g. by ballistic transport (Durisen and Estrada 2023).

The Yelle et al. (2018) work draws on a different atmospheric model, based on Koskinen and Guerlet (2018), and utilizes the methane mixing ratio in the deep atmosphere reported from occultations (Koskinen and Guerlet 2018) as well as mixing ratios calculated from the INMS data to construct and solve a diffusion profile of the form:

$$X_i = (H_i F_i) / (N_{H_2} D_i), \quad (9)$$

where X_i is the mixing ratio of compound i , H is the scale height, F is the flux, N_{H_2} is the density of H₂, the dominant atmospheric component, and D is the diffusion coefficient for compound i . They utilize the same source for coefficients for diffusion through H₂ gas as Waite et al. (2018); Mason and Marrero (1970). Their separate analysis confirms that the region sampled is dominated by diffusion, and calculates similar mass influxes independent of the underlying atmospheric model.

Serigano et al. (2020) and Serigano et al. (2022) build on this approach to calculate the MDR through the conversion

$$\text{MDR} = F_i m_i \times 2\pi R_S^2 \theta, \quad (10)$$

where m is the molecular mass, and θ is the latitudinal width over which the influx is spread. For θ , they utilize a latitudinal width of 16° , chosen to match the drop in signal for minor constituents at $\pm 8^\circ$ from the equator. They follow the same formulation for F_i as Yelle et al. (2018), adding H_2O and NH_3 (Serigano et al. 2020), as well as deconvolved compounds across the INMS mass range (Serigano et al. 2022). Their results suggest that the MDR may reach $74,000 \text{ kg s}^{-1}$.

In conclusion, the MDR from the rings to Saturn's atmosphere inferred from the INMS dataset is measured to be of the order of 10^4 kg s^{-1} , orders of magnitude higher than the 10^2 kg s^{-1} flux to the rings from meteoroid bombardment (Durisen and Estrada 2023). However, this calculation of the meteoroid flux assumes that only 10% of the material is retained as observable, absorbing material (Cuzzi and Estrada 1998; Estrada et al. 2015), in which case the total meteoroid influx becomes much more comparable to the INMS influx to Saturn's atmosphere. This inferred MDR is concentrated at the ring plane and is dependent on the measured number densities of the infalling material, as well as the downward velocities imposed. Analysis via two different atmospheric models plus separate consideration of Epstein drag suggests that velocities are on the order of $< 100 \text{ m s}^{-1}$. The use of higher velocities, such as the thermal velocity of the bulk atmosphere, results in higher influxes. The MDR of fine-grained material therefore appears to be exceptionally high. Modeling of ring dynamics suggests that ballistic transport in the rings and, to a lesser degree, mass loading could lead to inward flow of the inner B ring and C ring with an MDR on the order of 10^4 kg s^{-1} (Durisen and Estrada 2023), comparable to the INMS MDR. These values therefore allow a possible explanation for the INMS observations, but do not exclude the possibility that the observed D ring inflow phenomenon may be transient, and Cassini may have observed an unusually high rate as discussed below in Sect. 7.2.4; see also discussion of changes in the D ring in Sect. 6.2.

7.2.4 Atmospheric Observational Inferences and Their Implications for Time Variability

Moses et al. (2023) place constraints on the duration and/or properties of the equatorial ring inflow based on comparisons between Saturn's observed atmospheric composition and the modeled impact of the inflow on atmospheric chemistry. They demonstrate that the non-detections of HCN and HC_3N in Saturn's stratosphere from infrared observations, and the low inferred stratospheric abundance of CO_2 and H_2O from infrared, ultraviolet, and sub-millimeter observations, are inconsistent with coupled ion-neutral photochemical models that adopt ring-inflow compositions from either Serigano et al. (2022) or Miller et al. (2020). Moses et al. (2023) conclude that the large inflow rates inferred from INMS measurements must be a recent phenomenon (i.e., $\lesssim 4$ months to 50 years since the onset of such large ring inflow rates), or the ring material must consist primarily of small grains that do not ablate in the atmosphere at the depths perceived by CIRS. Even a $\lesssim 50$ -year-old continuous ring-inflow event would provide observational signatures of excess HC_3N , HCN, and CO_2 in Saturn's stratosphere, unless the material flowing in from the rings is primarily present as unablated grains smaller than $\sim 50 \text{ nm}$ for entry velocities of 25 km s^{-1} (Hamil et al. 2018)¹⁸, with only the most volatile compounds (CO , N_2 , CH_4) being present as vapor; furthermore, this volatile vapor component must spread globally before reaching the top of

¹⁸For grains with a radius of 10 nm , slightly smaller than the CDA best-fit size of 20 nm (Hsu et al. 2018), and density of 917 kg/m^3 , ablation occurs at velocities above 15 km/s (Hamil et al. 2018). These velocities are significantly higher than the velocities calculated by MIMI (Mitchell et al. 2018), which reach a maximum value of 2.5 km/s , and INMS (Perry et al. 2018; Yelle et al. 2018; Waite et al. 2018), which cite velocities on the order of 30 to 100 m/s for diffusively coupled material.

the stratosphere to prevent observational consequences in the stratosphere. Inflow of gas-phase CO and/or N₂ in particular cannot be reconciled with longer inflow timescales. The effects of assuming 28 u instead represents gas-phase C₂H₄ have not yet been examined.

Of the three atmospheric products that constrain the inflow timescale (HC₃N, HCN, and CO₂), HCN is the longest-lived, persisting for \sim 2000 years at 1 mbar and \sim 30 years at 1 μ bar. Therefore, even if the inflow of material is a transient but repeating phenomenon, the times when this process is inactive may be more common than when it is active. The possible division of inflowing material into gas-phase and solid-phase components is consistent with compositional constraints discussed in Sect. 7.2.1. Saturn's atmospheric chemistry places time constraints on the inflow of gas-phase material, but does not directly constrain the inflow timescale for solid-phase material unless it ablates. The short timescales for the present gas inflow rate may be tied to recent changes in the D ring (Sect. 6.2).

8 Ring Atmosphere

The exposure of the ring particles to photons, charged particles, and meteoroids produces a toroidal gaseous envelope of neutrals that is referred to as the ring atmosphere. Atoms and molecules are subsequently scattered from this atmosphere, creating a system-wide neutral corona that extends into Saturn's atmosphere and out into the magnetosphere well beyond the A ring (Johnson et al. 2006; Tseng et al. 2010, 2013a; Cuzzi et al. 2009). This extended ring atmosphere is superimposed on the toroidal atmospheres produced by outgassing from Enceladus, atmospheric escape from Titan, and, to a lesser extent, by sputtering of the icy satellites and the grains in the tenuous E, F and G rings, as seen in modeling of their H₂ and H contributions to the atmosphere over the ring plane (Tseng et al. 2011, 2013b). The presence of an ambient gas with molecules precipitating into Saturn's atmosphere was predicted prior to Cassini's arrival (Carlson 1980), and Cassini's Saturn Orbital Insertion (SOI) maneuver where the spacecraft crossed the ring plane provided the only in situ measurement of the ring atmosphere region over the B ring during the outbound trajectory.¹⁹ The simplicity of the ion mass spectrum, which consists of narrow peaks of O⁺ and O₂⁺ (Tokar et al. 2005), was surprising. It was the least contaminated mass spectrum obtained by the Cassini Plasma Spectrometer (CAPS; Young et al. 2004) during the mission. These SOI data are the basis of a model for the production, composition and spatial distribution of the ring atmosphere, dominated by O₂ (e.g. Johnson et al. 2006). That species other than oxygen must be present below the CAPS detection limits is suggested by reflectance observations of the rings (see Sects. 3.2 and 4.2) and, indirectly, by plasma observations outside the rings discussed below.

During Cassini's outbound SOI trajectory the CAPS instrument detected oxygen ions north of the B ring, through the Cassini division, out to the inner edge of the A ring (Tokar et al. 2005). Oxygen ions were again detected when CAPS was turned back on beyond the outer edge of the A ring as Cassini moved into the magnetosphere (Elrod et al. 2012, 2014). Although other water products were seen by INMS closer to the ring plane over the A ring (Waite et al. 2005), the dominance of oxygen ions was roughly consistent with our understanding of the radiation effects at the icy Jovian satellites (Johnson et al. 2004). That is, when ice is the dominant surface constituent, radiolysis and photolysis result in the ejection of water products, a significant fraction of which are O₂ and H₂. These volatiles do not recondense at the expected ring particle temperatures, resulting in residence times over the B-ring of the order of a half year for O₂ and an order of magnitude larger for H₂ (Johnson

¹⁹Readers are referred to Fig. 1 of Tokar et al. (2005) for a diagram of the SOI trajectory.

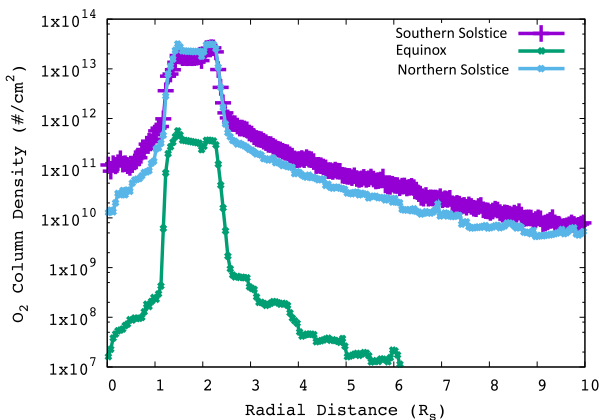


Fig. 18 Radial distribution of the modeled neutral O_2 column density for illumination of the A, B and C rings at three seasons with their minimum photodecomposition O_2 source rates: Southern Solstice (SOI, $2 \times 10^{57} O_2 s^{-1}$), Equinox ($2 \times 10^{25} O_2 s^{-1}$) and Northern Solstice (Grand Finale, $2 \times 10^{27} O_2 s^{-1}$). The respective injection rates into Saturn's atmosphere are $5 \times 10^{26} O_2 s^{-1}$ (27 kg s^{-1}), $5 \times 10^{23} O_2 s^{-1}$ (0.03 kg s^{-1}), and $2.5 \times 10^{26} O_2 s^{-1}$ (27 kg s^{-1}). (Tseng et al. 2010; Tseng and Ip 2011; Tseng et al. 2013a)

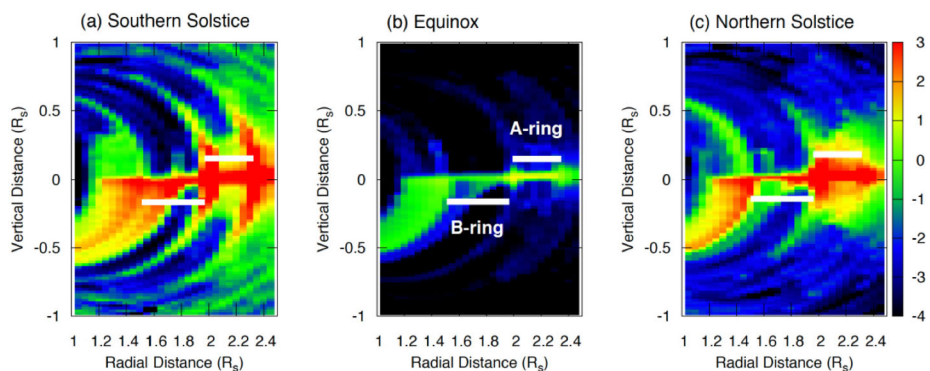


Fig. 19 O_2^+ ion density (cm^{-3}) in log10 scale as indicated by the color bar at right for the three seasons and neutral O_2 source rates in Fig. 18: (a) Southern Solstice (SOI), (b) Equinox and (c) Northern Solstice (Grand Finale). (Tseng et al. 2010; Tseng and Ip 2011; Tseng et al. 2013a)

et al. 2006). Because the inflowing magnetospheric plasma is suppressed at the edge of the A ring, photolysis is the dominant source of decomposition of the ice particles. Since the southern side of the ring plane was illuminated at SOI, the detection of a significant component of oxygen ions north of the ring plane indicates that a toroidal O_2 , and concomitant H_2 , atmosphere permeates and co-orbits with the ring particles with an O_2 centrifugal scale height $\sim 0.026 R_{ss}$ at $2 R_{ss}$, varying as $r^{3/2}$. Their lifetimes are primarily determined by photoionization and photodissociation producing O , O^+ , O_2^+ and H , H^+ and H_2^+ . Although ionization predominantly occurred south of the ring plane at SOI, the CAPS detection of O^+ and O_2^+ north of the plane indicates that the B ring is not fully opaque to the UV and/or to the flow of ions along field lines through the plane (Johnson et al. 2006). Of course, the estimates of the source rates and the lifetimes needed to interpret the CAPS data depend strongly on the uncertain fate of the chemistry initiated by the interaction of the radiation

products with the ring particles, a fraction of which are charged. In the following the fate of ionization and dissociation products is discussed using a rough estimate of their recycling on the ice grains (Johnson et al. 2006). Using this estimate, $\sim 270 \text{ kg/s}$ of O_2 is emitted from the A, B and C rings at solstice initiated by the photolysis of ice (Fig. 18).

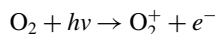
The motion of the ionic products is especially interesting as the magnetic equator is $\sim 0.046 R_S$ north of the ring plane and the magnetic field co-rotation speed falls below the neutral orbital speed at $R \lesssim 1.86 R_S$. Due to this geometry, ions formed and then “picked up” (accelerated) by the rotating field south of the ring plane and inside of $\sim 1.86 R_S$ precipitate into Saturn’s southern hemisphere (Luhmann et al. 2006; Bouhram et al. 2006) as seen in Fig. 19. This accounts for a molecular ion contribution to ring rain (see more detail in Fig. 4 in Tseng et al. 2010). This contribution consists of on the order of 0.5 to 1 percent of the oxygen neutral source rate from the ring particles, up to $\sim 0.3 \text{ kg s}^{-1}$, suggesting a minor contribution relative to the grain deposition rates of Hsu et al. (2018) and O’Donoghue et al. (2019).

Pick-up ions that do not precipitate into Saturn will oscillate along the field lines about the magnetic equator prior to impacting a ring particle. Such ions have a centrifugal scale height of O_2^+ varying from $\lesssim 0.1$ -to- $0.16 R_S$ across the region where CAPS ring atmosphere data were acquired ($\sim 1.8 - 2.08 R_S$). Therefore, although neutral molecules, including O_2 , have not been directly measured, the observed population of ions oscillating about the magnetic equator with lifetimes limited by impact with ring particles indicates the presence of a neutral source that we call the ring atmosphere.

This picture of a ring atmosphere dominated near the ring plane by O_2 is strongly supported by the ion temperatures measured by CAPS (Johnson et al. 2006), which are approximated by the sum of the ions’ energy at formation and their pick-up gyro energy. Newly formed O_2^+ and O^+ , which are accelerated by Saturn’s rotating magnetic field, are produced with very different initial speed distributions. Dissociative photoionization of O_2 produces an O^+ with a significant excess energy due to the kinetic energy associated with loss of the O atom:



In contrast, O_2^+ is formed with very little excess energy because of the low mass of the electron that is lost:



Since the pick-up contribution to the ion temperature depends on the relative speeds between the neutrals that orbit at the Keplerian orbital velocity, and ions confined by the rotating magnetic field orbiting at the magnetic field co-rotation velocity, the O_2^+ temperature was seen to go through a minimum at $\sim 1.86 R_S$, where the Keplerian and co-rotation velocities are roughly equal (see Fig. 1b of Johnson et al. 2006). That is, because of the low excess energy of formation of O_2^+ , its temperature is dominated by the pick-up energy, whereas the O^+ temperature is dominated by its excess energy and does not exhibit as strong of a radial influence from the pick-up energy. The radial temperature trends of O_2^+ and O^+ therefore support their relationship to neutral O_2 .

Because the distance of the magnetic equator above the ring plane is of the order of the neutral scale height, those ions moving about the magnetic equator can collide with and charge exchange with neutrals, producing hot neutrals with energies determined primarily by the ion’s speed. These scattered neutrals create a highly extended component of the ring atmosphere indicated by the radial column densities in Fig. 18. It is seen that a fraction of the

scattered O₂, as well as H₂ not shown here, precipitates into Saturn's atmosphere as neutrals with estimated rates at three phases given in the caption. The absolute magnitude of the ring atmosphere density and, hence, these precipitation rates, depends on the still-uncertain recycling of hydrogen and oxygen on the ring particles.

Although the much lighter H₂ dominates O₂ in the extended ring atmosphere, it is not the dominant source of H₂ or H over the ring plane. Modelling of significant contributions to hydrogen in this region indicate it also comes from Saturn's extended atmosphere, escape from Titan's atmosphere, and the Enceladus torus (Tseng et al. 2011, 2013b) each with very different centrifugal scale heights. This toroidal atmosphere produces the Lyman-alpha flux in this region (e.g. Ben-Jaffel et al. 2023) as well as the hot proton plasma detected by Cassini at the inner (Kollmann et al. 2018) and outer (Cooper et al. 2018) edges of the main rings. However, the observed seasonal and longitudinal dependence of the Lyman-alpha flux (Ben-Jaffel et al. 2023) are suggestive of a ring source of hydrogen. These data have also been used to help constrain hydrogen recycling on the ring particles. Of particular interest is the role of the incident H and H⁺ on the particles of the inner D-ring ringlets that has yet to be modeled.

The extension of the neutral ring atmosphere beyond the edge of the A ring ($R_S = 2.27$) seen in Fig. 18 contributes to the local plasma out to large distances. As Cassini did not fly over the rings again until the end of the mission, by which time the CAPS instrument was unfortunately shut off, the model of the O₂ ring atmosphere was further confirmed by analysis of the plasma data outside the A ring (e.g. Elrod et al. 2014, 2012; Christon et al. 2013). That is, since the oxygen plasma density roughly tracks the local neutral density, the plasma outside the A ring exhibited a variability consistent with a steep drop in the solar flux onto the ring plane as Saturn approached equinox, as indicated by the drop in the source rate in Fig. 18. Post-equinox, when the magnetic equator is above the sunlit ring plane, the same processes occur. Therefore, the tilt of the ring plane to the sun leads to an extended ring atmosphere that varies with inclination to the solar illumination (Tseng et al. 2010).

To explain the radiation processing by the magnetospheric plasma adsorbed at the outer edge of the A ring, Tseng and Ip (2011) suggested that the erosion of the icy ring particles in this region might be sustained by water from Enceladus. Refreshed ice grains in this region were also suggested to account for the observed delay in the post-equinox repopulation of O₂⁺ plasma (Christon et al. 2013). Using a direct simulation Monte Carlo model and a plume outflow rate of 10^{28} molecules H₂O s⁻¹, Cassidy and Johnson (2010) find a mass deposition rate from Enceladus' neutral cloud onto the rings of approximately 100 kg s⁻¹, which is equivalent to a quarter of the mass of the main rings in approximately 1 Gyr if the plume rate were constant. (Note that the active lifetime of the Enceladus plume is at present poorly constrained.) However, using a similar plume rate Smith and Richardson (2021) find a much lower water product deposition rate. Further research into contributions from Enceladus to the rings is needed, including how such contributions would affect regional composition and albedo in the rings.

Even though INMS detected other water products closer to the ring plane during SOI (Waite et al. 2005) when CAPS was briefly off, the absence of non-ice products was striking. This is especially the case given the material from Enceladus that is deposited onto the ring particles (Jurac and Richardson 2007; Farrell et al. 2008; Cassidy and Johnson 2010). This material is likely processed in two ways. Due to collisions of ring particles, contaminants more refractory than H₂O can be dispersed into the ring particles, depleting surface concentrations. In addition, any desorbed volatiles, or surface species made volatile by reactions with the water products, can be scattered into the outer magnetosphere or into Saturn's atmosphere as discussed above for the photolytically produced O₂. That the latter process

occurs is confirmed by the seasonal variation of ions of mass 28 u as well as O₂⁺ observed by the MIMI CHEMS (Charge-Energy-Mass Spectrometer) sensor at suprathermal energies (Christon et al. 2014). Further analysis of CHEMS data presented at the Cassini Science Seminar in 2018 by Hamilton and colleagues showed that C⁺ and CO⁺ also exhibit a seasonal variation suggestive of a photolytic ring source that is seen to peak in fall of 2014 and persist through to the Grand Finale (Hamilton et al. 2018). This was interpreted to be due to CO₂ deposited on the rings from the Enceladus torus. The observed lifetimes of CO⁺ and CO₂⁺ seen in the plasma appears to correlate with their photoionization rates producing CO⁺ and CO₂⁺ over the rings, which are scattered into the outer magnetosphere as neutrals by charge exchange with the dominant O₂.

Although the D-ring particles are also dominated by ice so that photolysis can contribute water products to the ring atmosphere, they contain a higher concentration of more refractory materials. Whereas the plasma flux onto the other rings is highly suppressed, Kollmann et al. (2018) examined the hot plasma quenching going from the outer regions of Saturn's atmosphere onto the inner edge of the D-ring. In this way they were able to estimate the extended scale height of Saturn's atmosphere as well as sense the effect of the ambient gas-phase species over the inner ringlets, which are exposed to hot neutrals and energetic ions. Surprisingly, their estimated flux, 10¹⁶ H₂O/m² is remarkably similar to that estimated by Tseng et al. (2010) for the contribution to the column density in this region of O₂ formed from the A, B and C rings. Therefore, the D-ring contribution to its local atmosphere might indeed be small, in spite of any chemistry induced in the particles by the incident protons and hydrogen. These interactions should produce a not-yet modeled gas component originating from this region that would also contribute to Saturn's atmosphere. If this D ring atmosphere is related to the CH₄-rich inflowing gas measured by INMS during the Grand Finale, then its composition must be quite different than the ring atmosphere over the main rings.

8.1 Possible Ring Atmosphere Connection to the Inflowing Material

We have seen that the composition of the inflowing material differs substantially from the observed composition in the main rings and in the D ring, namely in how water-poor the inflowing material is (Table 6). Here, we consider whether this difference in composition is intrinsic to the material, or whether the initial source composition may be identical and the observed differences could be caused by different evolutionary processes occurring in Saturn's ring environment. In the latter case, more volatile compounds may be lost via such processes, and the material observed in situ may represent the remaining residue. This volatile component may contribute to the ring atmosphere, including in the D ring region. We consider this component here. Since the D ring bulk composition is poorly constrained (Sect. 6.1), we assume that it is related to the main ring composition with a greater abundance of non-icy material.

A large mass of material more volatile than water (e.g. CH₄, CO) was observed by INMS, and the latitudinal variation suggests it is present as a volatile component rather than as an impact fragment from more refractory material (Miller et al. 2020; Serigano et al. 2020). However, compounds more volatile than water are not observed in the main rings (e.g. Sect. 3.2.4), and should be lost more quickly than water ice in the absence of a lag deposit. Therefore, to calculate the missing water mass, we make the simplifying assumption here that all non-water masses detected by INMS can be attributed to impact fragments of refractory organic material related to the neutral and/or UV absorbers in the main rings (Sects. 3.2.2 and 3.2.1). In this simplified scenario, there are two observed components (water and organic products), and the missing mass of water is the mass required to reconcile

the relative abundance of these two components with remote observations of the D ring or main rings.

The range in observed inflowing mass from INMS is bracketed by values in Serigano et al. (2020) (see Table 7), between 2080 and 74000 kg s⁻¹. The observed inflowing composition was approximately 16 to 24 wt.% water (Table 5). If we take 24 wt.% as representative, this implies that the inflowing non-water mass is 1,581 to 56,260 kg s⁻¹. For the source material, we take the lower limit of 80 vol.% water ice in the bulk D ring composition (Fig. 16), and assume a density ratio for water/organics of 0.9/1.4 (Reynard and Sotin 2023) i.e., equal porosity for the two compositions. This corresponds to 72 wt.% water ice in the bulk D ring. In order to reconcile the observed composition with the bulk D ring, between 3,566 and 126,857 kg s⁻¹ of water must be volatilized or lost in the ring environment. Estimates of the ring atmosphere production rate for the main rings (Fig. 18) peak at 2×10^{27} O₂ molecules s⁻¹, which corresponds to approximately 120 kg s⁻¹ of water ice, a value that is significantly lower than the required water mass loss (3,566 – 126,857 kg s⁻¹). The ring atmosphere in the D ring region has not yet been modeled, but as discussed above, estimates by Kollmann et al. (2018) of plasma quenching suggest that the D ring atmosphere flux may be relatively small. If true, then this estimate of 120 kg s⁻¹ may be an upper limit. Steady ongoing production of the water-poor inflow composition is therefore not realistic, since the water loss rate required to keep pace with the mass deposition rate (3,566 – 126,857 kg s⁻¹) is much greater than the expected rate of water volatilization in the D ring region.

An alternative explanation is that ring “residue” may accumulate, since the observed inflow may be a transient process (Sect. 7.2.4). From Moses et al. (2023), the time constraints on the inflow are between 4 and 600 months. This time range, together with the water mass loss rate from above (3,566 – 126,857 kg s⁻¹) implies a total water mass loss between 4×10^{10} and 2×10^{14} kg. We can generate a rough estimate for the total mass of the ring atmosphere by taking an upper limit on the column density, 1×10^{14} cm⁻² (Fig. 18), and the surface area of the rings, 4×10^{20} cm² (Table 2.2). This yields on the order of 4×10^{34} molecules of O₂, or 2×10^9 kg. For the extended ring atmosphere from 2.5 to 10 R_S, we calculate an additional 5×10^8 kg using an upper limit column density of 1×10^{12} cm⁻² (Fig. 18). We therefore estimate a total ring atmosphere mass of $\sim 3 \times 10^9$ kg. The estimated water loss that would be needed to reconcile the inflowing composition with the bulk D ring composition (4×10^{10} and 2×10^{14} kg) is likely orders of magnitude greater than the mass of the ring atmosphere. We would therefore expect that this magnitude of water loss may be significant, and have a noticeable effect on the ring system.

While the total required water mass loss appears large in comparison to the estimated ring atmosphere mass, it may be possible that the water loss has occurred over a sufficiently long timescale that it can be reconciled with the expected ring atmosphere production and loss rates. As calculated above, the production rate for the ring atmosphere is on the order of 120 kg of water s⁻¹. To remove 4×10^{10} to 2×10^{14} kg of water into the ring atmosphere would then require between 10 and 50,000 years. This is rapid on geologic timescales, and further suggests that the observed inflow may be transient if the material is derived from the bulk D ring. This additionally assumes concentration of residue material at the inner edge of the D ring. The overall contribution of the D ring region to the ring atmosphere has not yet been modeled but is expected to be small in comparison to the main rings. Loss rates for the ring atmosphere into Saturn’s atmosphere are < 30 kg s⁻¹ (Fig. 18), and transfer of water vapor products outward to the magnetosphere may be required instead if the INMS material does represent D ring residue. While we have assumed here that all inflowing material may be represented by a combination of water and complex organic material, this simplified scenario does not explain the presence of CH₄ and CO or N₂ in the vapor phase (Sect. 7.2.1).

A related scenario may involve water loss from a subset of the D ring material, and selective deorbiting of that residue into Saturn's atmosphere. The "tholin" material used for spectral fitting in Cuzzi et al. (2018b) produces the best fits when it is concentrated into a subset of grains that comprises 2–40% of the overall population of grains. We suggest that these grains may be volatilized more quickly due to increased absorption of sunlight by the darker organics, and subsequently higher temperatures for organic-bearing grains. Water loss may reduce the size of these organic-rich grains, which in turn may increase the likelihood that they fall into Saturn's atmosphere since small grains may be decelerated more rapidly by impacts with Saturn's extended atmosphere (Mitchell et al. 2018). The INMS material is hypothesized to be very small in size (e.g. Perry et al. 2018), and if the inflowing material selectively draws from the organic-rich material in the D ring, such a scenario may reduce the water loss mass required to reconcile INMS observations with the bulk D ring composition.

9 Relationship Between the Rings and Ring Moons

While inwardly connected with Saturn through the observed mass inflow discussed above, from a compositional standpoint the main rings also appear to be outwardly linked with Saturn's ring moons, and in particular with the innermost ones. These include small satellites orbiting within (Pan, Daphnis) and just outside the A ring (Atlas), shepherding the F ring (Prometheus and Pandora), and the co-orbitals Janus and Epimetheus (orbiting at $\sim 151,000$ km).

As discussed in greater detail in Ciarniello et al. (2024, this collection), Cassini remote sensing observations at UV-VIS-IR wavelengths show significant spectral similarities between the main rings and these ring moons. Both are characterized by the dominance of water ice features with absorption bands at 1.5, 2 and 3 μm , and by UV absorption at wavelengths shorter than $\sim 0.55 \mu\text{m}$, indicative of the presence of non-icy material. Although such spectral features can also be observed on the rest of Saturn's icy moons, spectral indicator analysis (see Sect. 6 in Ciarniello et al. 2024) reveals similar trends between the main rings and inner ring moons, for which the intensity of the UV absorption is in general positively correlated with the albedo and the water ice band depths. This is not the case for the mid-sized icy satellites, thus suggesting a similar compositional paradigm for the rings and the inner ring moons in which the UV absorber is embedded in water ice grains, with an additional endmember as a broad-band absorber (see Sect. 4).

Further evidence of a compositional link between the main rings and ring moons is provided by the radial trend of the ring moon spectral shapes, which become progressively similar to that of the A ring moving inward from Janus and Epimetheus, which appear the most polluted, to Pan. In fact, this radial trend may result from the accumulation of nearby A ring particles on the ring moon surfaces. This accumulation is more effective for the inner moons, and counteracts the contamination from meteoritic bombardment that modifies the surface composition inherited from the rings. An additional contribution may also come from a seasonal flow of neutral species from the ring atmosphere that are scattered beyond the edge of the rings by molecules and ions generated from the rings by photoionization and subsequently accelerated by the magnetic field (Tseng et al. 2010).

Ring moons are thought to originate within or in the vicinity of the A ring, accumulating ring material on their external layers in the process, and then moving outward due to the gravitational torque of the rings (Charnoz et al. 2010; see also Sect. 5 of Ciarniello et al. 2024 and Sect. 3.2.2 of Blanc et al. 2024). As a consequence, Janus and Epimetheus, orbiting

at larger distance from Saturn with respect to the other ring moons, are likely older and may have endured a longer exposure to meteoritic bombardment. In this respect, it is interesting to note that these two moons appear spectrally similar to the C ring, the most contaminated of the main rings, thus pointing to a similar role for the pollution mechanism. However, we note that contrary to the main rings, ring moons are affected by additional exogenous processes such as contamination from E-ring grains and the effects of charged particle fluxes (see Sect. 8 of Ciarniello et al. 2024), thus requiring particular care in comparisons with contamination/alteration processes in the main rings.

10 Conclusions

From this retrospective look at the Cassini dataset and at previous remote observations of the Saturnian ring system, a few themes for the ring composition emerge. Overall, the bulk composition of Saturn’s rings is overwhelmingly dominated by water ice. This is especially true in the optically thick B ring, which dominates the ring mass. However, remote sensing constraints suggest that even the “water-poor” D ring may be as much as 80 vol.% water. This composition is consistent with fairly minimal signs of pollution or contamination of the rings by external impactors. While microwave observations suggest that some silicate material may remain “hidden” from surficial spectroscopy in the C ring, in general the dynamic evolution of the rings suggests they are well-mixed and this composition is representative of the bulk. Thus, the effective exposure age of the rings to micrometeoroid flux may be relatively young, on the order of 10^8 years.

While the composition is dominated by water throughout, compositional trends are observed with both radial distance (Table 6) and optical depth. The abundance of non-water components tends to increase going from the A ring towards the D ring. This trend mirrors the inward increase in temperature seen by VIMS and CIRS data on the sunlit side. Similarly, the abundance of small particles increases from the inner A ring to the D ring. The Cassini Division deviates from these trends, and instead points to the influence of optical depth on the ring composition. Namely, optical depths are lower in the C ring and Cassini Division, and as a result these regions are more susceptible to pollution from external impactors. Microwave data show that the composition of the middle C ring may also be silicate-rich, with icy mantles concealing interiors that may point towards the recent break up of a small rocky body.

Data collected during Cassini’s Grand Finale of material from the rings support this trend of enhanced abundance of non-water components moving inwards towards Saturn. However, the degree of enhancement from INMS measurements on the smallest size fraction is extreme. This material is comprised of small grains as well as gas that includes a 28 u component (likely dominated by CO with some C_2H_4 and possibly some N_2) and methane. Such highly volatile material has not previously been detected in the main rings from remote sensing observations. While inflow of charged “ring rain” material to the mid-latitudes is likely a steady process, constraints from Saturn’s atmospheric chemistry suggest that the more massive equatorial inflow detected during the Grand Finale may represent a recent event. This may be related to the appearance of bright clumps in the D68 ringlet in 2014, just a few years before the measurements.

The composition of this material may be partially reconciled with the bulk D ring composition via photolysis and sublimation processes, which are known to generate the ring atmosphere. While these processes in the D ring region have not been specifically modeled, estimates for the local gas density from plasma flux onto the rings suggest that D ring

contributions to the ring atmosphere may be relatively small. If the equatorial inflow does represent evolved material from the main rings, the timescale for devolatilization must be much longer than the inflow timescale ($\sim 10^5 \times$) and the ring “residue” must accumulate and be effectively fractionated by the inflow process. The simplified scenario presented here may broadly allow reconciliation of the inflow composition with the bulk composition, but it does not explain the presence of the vapor component in the INMS inflow. This processing of the ring material may be related to the ring “cleaning” suggested by Crida et al. (2019).

Ballistic transport indicates mass inflow of material from across the rings with total inward fluxes consistent with the equatorial inflow abundances. However, additional work is needed to explore the relationship of these processes to the compositionally- and size-fractionated material in the D ring region. Similarly, future work should examine how the Grand Finale inflow fits within the broader context of ring evolution, and the degree to which these processes are stochastic or smooth in time.

Acknowledgements We are grateful to M. Tiscareno and to an anonymous reviewer for their constructive feedback. We also thank V. Lainey for organizing the discussions that led to this work, and to A. Crida for editing. This research was supported by the International Space Science Institute (ISSI) in Bern, through ISSI Workshop “New Vision of the Saturnian System in the Context of a Highly Dissipative Saturn” (Bern, 9–13 May 2022). This research has made use of NASA’s Astrophysics Data System. KEM acknowledges support from SwRI. GF and MC acknowledge support from INAF-IAPS.

Author Contribution The idea for this review article came from GF and JNC. All authors contributed to the literature search. New data analysis was performed by KB, CF, MMH, JC, KEM and WLT. All authors contributed to drafting and revisions.

Funding Open access funding provided by Istituto Nazionale di Astrofisica within the CRUI-CARE Agreement. Nothing to declare.

Data Availability Cassini data used in this work are archived in NASA’s Planetary Data System (PDS) and publicly available.

Declarations

Competing Interests The authors have no competing interests to declare.

Open Access This article is licensed under a Creative Commons Attribution 4.0 International License, which permits use, sharing, adaptation, distribution and reproduction in any medium or format, as long as you give appropriate credit to the original author(s) and the source, provide a link to the Creative Commons licence, and indicate if changes were made. The images or other third party material in this article are included in the article’s Creative Commons licence, unless indicated otherwise in a credit line to the material. If material is not included in the article’s Creative Commons licence and your intended use is not permitted by statutory regulation or exceeds the permitted use, you will need to obtain permission directly from the copyright holder. To view a copy of this licence, visit <http://creativecommons.org/licenses/by/4.0/>.

References

- A’Hearn JA, Hedman MM, Hamilton DP (2021) Modeling Saturn’s D68 clumps as a co-orbital satellite system. *Planet Sci J* 2(2):74. <https://doi.org/10.3847/PSJ/abed57>. arXiv:2103.05119 [astro-ph.EP]
- Albers N, Spahn F (2006) The influence of particle adhesion on the stability of agglomerates in Saturn’s rings. *Icarus* 181(1):292–301. <https://doi.org/10.1016/j.icarus.2005.10.011>
- Altobelli N, Lopez-Paz D, Pilorz S, et al (2014) Two numerical models designed to reproduce Saturn ring temperatures as measured by Cassini-CIRS. *Icarus* 238:205–220. <https://doi.org/10.1016/j.icarus.2014.04.031>

- Atreya SK, Waite JH (1981) Saturn ionosphere: theoretical interpretation. *Nature* 292(5825):682–683. <https://doi.org/10.1038/292682a0>
- Baillié K, Colwell JE, Lissauer JJ, et al (2011) Waves in Cassini UVIS stellar occultations. 2. The C ring. *Icarus* 216:292–308. <https://doi.org/10.1016/j.icarus.2011.05.019>
- Baillié K, Colwell JE, Esposito LW, et al (2013) Meter-sized moonlet population in Saturn's C ring and Cassini division. *Astron J* 145(6):171. <https://doi.org/10.1088/0004-6256/145/6/171>
- Becker TM (2016) Saturn's rings: measuring particle size distributions using Cassini UVIS occultation data. PhD thesis, University of Central Florida
- Becker TM, Colwell JE, Esposito LW, et al (2016) Characterizing the particle size distribution of Saturn's A ring with Cassini UVIS occultation data. *Icarus* 279:20–35. <https://doi.org/10.1016/j.icarus.2015.11.001>
- Bell JM, Hunter Waite J, Westlake JH, et al (2014) Developing a self-consistent description of Titan's upper atmosphere without hydrodynamic escape. *J Geophys Res Space Phys* 119(6):4957–4972. <https://doi.org/10.1002/2014JA019781>
- Ben-Jaffel L, Moses JI, West RA, et al (2023) The enigmatic abundance of atomic hydrogen in Saturn's upper atmosphere. *Planet Sci J* 4(3):54. <https://doi.org/10.3847/PSJ/acaf78>
- Birks JB (1970) Photophysics of aromatic molecules. Wiley, London
- Blanc M, Crida A, Shibaike Y (2024) *Space Sci Rev* 220
- Bohren CF, Huffman DR (1983). Absorption and scattering of light by small particles
- Bouhoum M, Johnson RE, Berthelier JJ, et al (2006) A test-particle model of the atmosphere/ionosphere system of Saturn's main rings. *Geophys Res Lett* 33(5):L05106. <https://doi.org/10.1029/2005GL025011>
- Bradley ET, Colwell JE, Esposito LW, et al (2010) Far ultraviolet spectral properties of Saturn's rings from Cassini UVIS. *Icarus* 206(2):458–466. <https://doi.org/10.1016/j.icarus.2009.12.021>
- Bradley ET, Colwell JE, Esposito LW (2013) Scattering properties of Saturn's rings in the far ultraviolet from Cassini UVIS spectra. *Icarus* 225(1):726–739. <https://doi.org/10.1016/j.icarus.2013.04.008>
- Brilliantov N, Krapivsky PL, Bodrova A, et al (2015) Size distribution of particles in Saturn's rings from aggregation and fragmentation. *Proc Natl Acad Sci* 112(31):9536–9541. <https://doi.org/10.1073/pnas.1503957112>
- Brown RH, Baines KH, Bellucci G, et al (2004) The Cassini visual and infrared mapping spectrometer (vims) investigation. *Space Sci Rev* 115(1–4):111–168. <https://doi.org/10.1007/s11214-004-1453-x>
- Canup RM (2010) Origin of Saturn's rings and inner moons by mass removal from a lost Titan-sized satellite. *Nature* 468:943–946. <https://doi.org/10.1038/nature09661>
- Carlson RW (1980) Photo-sputtering of ice and hydrogen around Saturn's rings. *Nature* 283(5746):461. <https://doi.org/10.1038/283461a0>
- Cassidy TA, Johnson RE (2010) Collisional spreading of Enceladus' neutral cloud. *Icarus* 209(2):696–703. <https://doi.org/10.1016/j.icarus.2010.04.010>
- Chadney J (2017) Modelling the Upper Atmosphere of Gas-Giant Exoplanets Irradiated by Low-Mass Stars. <https://doi.org/10.1007/978-3-319-63351-0>
- Charnoz S, Salmon J, Crida A (2010) The recent formation of Saturn's moonlets from viscous spreading of the main rings. *Nature* 465(7299):752–754. <https://doi.org/10.1038/nature09096>
- Christon SP, Hamilton DC, Difabio RD, et al (2013) Saturn suprathermal O₂⁺ and mass-28⁺ molecular ions: long-term seasonal and solar variation. *J Geophys Res Space Phys* 118(6):3446–3463. <https://doi.org/10.1002/jgra.50383>
- Christon SP, Hamilton DC, Mitchell DG, et al (2014) Suprathermal magnetospheric minor ions heavier than water at Saturn: discovery of ²⁸M⁺ seasonal variations. *J Geophys Res Space Phys* 119(7):5662–5673. <https://doi.org/10.1002/2014JA020010>
- Ciarniello M, Capaccioni F, Filacchione G, et al (2011) Hapke modeling of Rhea surface properties through Cassini-VIMS spectra. *Icarus* 214(2):541–555. <https://doi.org/10.1016/j.icarus.2011.05.010>
- Ciarniello M, Filacchione G, D'Aversa E, et al (2019) Cassini-VIMS observations of Saturn's main rings: II. A spectrophotometric study by means of Monte Carlo ray-tracing and Hapke's theory. *Icarus* 317:242–265. <https://doi.org/10.1016/j.icarus.2018.07.010>
- Ciarniello M, Filacchione G, Nicholson PD, et al (2024) *Space Sci Rev* 220
- Clar F (1964) Polycyclic hydrocarbons. Academic Press, NY
- Clark RN, McCord TB (1980) The rings of Saturn: new near-infrared reflectance measurements and a 0.326–4.08 μm summary. *Icarus* 43(2):161–168. [https://doi.org/10.1016/0019-1035\(80\)90116-5](https://doi.org/10.1016/0019-1035(80)90116-5)
- Clark RN, Cruikshank DP, Jaumann R, et al (2012) The surface composition of Iapetus: mapping results from Cassini VIMS. *Icarus* 218(2):831–860. <https://doi.org/10.1016/j.icarus.2012.01.008>
- Clark RN, Brown RH, Cruikshank DP, et al (2019) Isotopic ratios of Saturn's rings and satellites: implications for the origin of water and Phoebe. *Icarus* 321:791–802. <https://doi.org/10.1016/j.icarus.2018.11.029>
- Colina L, Bohlin RC, Castelli F (1996) The 0.12–2.5 micron absolute flux distribution of the Sun for comparison with solar analog stars. *Astron J* 112:307. <https://doi.org/10.1086/118016>

- Colwell JE, Esposito LW, Sremčević M (2006) Self-gravity wakes in Saturn's A ring measured by stellar occultations from Cassini. *Geophys Res Lett* 33(7):L07201. <https://doi.org/10.1029/2005GL025163>
- Colwell JE, Cooney JH, Esposito LW, et al (2009) Density waves in Cassini UVIS stellar occultations. 1. The Cassini division. *Icarus* 200(2):574–580. <https://doi.org/10.1016/j.icarus.2008.12.031>
- Colwell J, Esposito L, Jerousek R, et al (2010) Cassini uvis stellar occultation observations of Saturn's rings. *Astron J* 140(6):1569
- Connerney JEP (1986) Magnetic connection for Saturn's rings and atmosphere. *Geophys Res Lett* 13(8):773–776. <https://doi.org/10.1029/GL013i008p00773>
- Connerney JEP, Waite JH (1984) New model of Saturn's ionosphere with an influx of water from the rings. *Nature* 312(5990):136–138. <https://doi.org/10.1038/312136a0>
- Cooke ML (1991) Saturn's rings: photometric studies of the C ring and radial variation in the Keeler gap. PhD thesis, Cornell University, New York
- Cooper J, Johnson R, Kollmann P, et al (2018) Plasma, neutral atmosphere, and energetic radiation environments of planetary rings. *Planet Ring Syst Prop Struct Evol*, 363–398
- Coradini A, Tosi F, Gavrinish AI, et al (2008) Identification of spectral units on Phoebe. *Icarus* 193(1):233–251. <https://doi.org/10.1016/j.icarus.2007.07.023>
- Cravens TE (1987) vibrationally excited molecular hydrogen in the upper atmosphere of Jupiter. *J Geophys Res* 92(A10):11,083–11,100. <https://doi.org/10.1029/JA092iA10p11083>
- Cravens TE, Moore L, Waite Jr J, et al (2019) The ion composition of Saturn's equatorial ionosphere as observed by Cassini. *Geophys Res Lett* 46(12):6315–6321
- Crida A, Charnoz S, Hsu HW, et al (2019) Are Saturn's rings actually young? *Nat Astron* 3:967–970. <https://doi.org/10.1038/s41550-019-0876-y>
- Crida A, Estrada PR, Nicholson PD, et al (2024) *Space Sci Rev* 220
- Cruikshank DP, Dalton JB, Dalle Ore CM, et al (2007) Surface composition of Hyperion. *Nature* 448(7149):54–56. <https://doi.org/10.1038/nature05948>
- Cruikshank DP, Wegryn E, Dalle Ore CM, et al (2008) Hydrocarbons on Saturn's satellites Iapetus and Phoebe. *Icarus* 193(2):334–343. <https://doi.org/10.1016/j.icarus.2007.04.036>
- Cuzzi JN (1985) Rings of Uranus: not so thick, not so black. *Icarus* 63(2):312–316. [https://doi.org/10.1016/0019-1035\(85\)90014-4](https://doi.org/10.1016/0019-1035(85)90014-4)
- Cuzzi JN, Estrada PR (1998) Compositional evolution of Saturn's rings due to meteoroid bombardment. *Icarus* 132(1):1–35. <https://doi.org/10.1006/icar.1997.5863>
- Cuzzi JN, Pollack JB, Summers AL (1980) Saturn's rings: particle composition and size distribution as constrained by observations at microwave wavelengths II. Radio interferometric observations. *Icarus* 44(3):683–705. [https://doi.org/10.1016/0019-1035\(80\)90137-2](https://doi.org/10.1016/0019-1035(80)90137-2)
- Cuzzi JN, French RG, Dones L (2002) HST multicolor (255–1042 nm) photometry of Saturn's main rings. I: radial profiles, phase and opening angle variations, and regional spectra. *Icarus* 158(1):199–223. <https://doi.org/10.1006/icar.2002.6851>
- Cuzzi J, Clark R, Filacchione G, et al (2009) Ring particle composition and size distribution. In: Dougherty MK, Esposito LW, Krimigis SM (eds) *Saturn from Cassini-Huygens*. Springer, Dordrecht, p 459. https://doi.org/10.1007/978-1-4020-9217-6_15
- Cuzzi JN, Estrada PR, Davis SS (2014a) Utilitarian opacity model for aggregate particles in protoplanetary nebulae and exoplanet atmospheres. *Astrophys J Suppl Ser* 210(2):21. <https://doi.org/10.1088/0067-0049/210/2/21>. arXiv:1312.1798 [astro-ph.EP]
- Cuzzi JN, Whizin AD, Hogan RC, et al (2014b) Saturn's F ring core: calm in the midst of chaos. *Icarus* 232:157–175. <https://doi.org/10.1016/j.icarus.2013.12.027>
- Cuzzi JN, Chambers LB, Hendrix AR (2017) Rough surfaces: is the dark stuff just shadow?; Who knows what evil lurks in the hearts of men? The shadow knows!. *Icarus* 289:281–294. <https://doi.org/10.1016/j.icarus.2016.10.018>
- Cuzzi JN, Filacchione G, Marouf EA (2018a) The rings of Saturn. In: Tiscareno MS, Murray CD (eds) *Planetary ring systems. Properties, structure, and evolution*, pp 51–92. <https://doi.org/10.1017/9781316286791.003>
- Cuzzi JN, French RG, Hendrix AR, et al (2018b) HST-STIS spectra and the redness of Saturn's rings. *Icarus* 309:363–388. <https://doi.org/10.1016/j.icarus.2018.02.025>
- Cuzzi JN, Marouf EA, French RG, et al (2024) Saturn's F Ring is Intermittently Shepherded by Prometheus. *Sci Adv*. <https://doi.org/10.1126/sciadv.adl6601> [astro-ph.EP]
- Daisaka H, Tanaka H, Ida S (2001) Viscosity in a dense planetary ring with self-gravitating particles. *Icarus* 154(2):296–312. <https://doi.org/10.1006/icar.2001.6716>
- Dalle Ore CM, Cruikshank DP, Clark RN (2012) Infrared spectroscopic characterization of the low-albedo materials on Iapetus. *Icarus* 221(2):735–743. <https://doi.org/10.1016/j.icarus.2012.09.010>
- Durisen RH, Estrada PR (2023) Large mass inflow rates in Saturn's rings due to ballistic transport and mass loading. *Icarus* 400:115221. <https://doi.org/10.1016/j.icarus.2022.115221>. arXiv:2305.13578 [astro-ph.EP]

- Durisen RH, Cramer NL, Murphy BW, et al (1989) Ballistic transport in planetary ring systems due to particle erosion mechanisms I. Theory, numerical methods, and illustrative examples. *Icarus* 80(1):136–166. [https://doi.org/10.1016/0019-1035\(89\)90164-4](https://doi.org/10.1016/0019-1035(89)90164-4)
- Durisen RH, Bode PW, Dyck SG, et al (1996) Ballistic transport in planetary ring systems due to particle erosion mechanisms. III. Torques and mass loading by meteoroid impacts. *Icarus* 124(1):220–236. <https://doi.org/10.1006/icar.1996.0200>
- Eckert S, Colwell JE, Becker TM, et al (2021) Sizes of the smallest particles at Saturn's ring edges. *Icarus* 357:114224. <https://doi.org/10.1016/j.icarus.2020.114224>
- Edgington SG, Spilker LJ, Leyrat C, et al (2008) Emissivity in the thermal IR: composition and polarization in Saturn's rings with Cassini/CIRS: part 2. In: AAS/Division for Planetary Sciences Meeting abstracts #40, pp 29.04
- Elachi C, Allison MD, Borgarelli L, et al (2004) Radar: the Cassini Titan radar mapper. *Space Sci Rev* 115(1–4):71–110. <https://doi.org/10.1007/s11214-004-1438-9>
- Elliott JP, Esposito LW (2011) Regolith depth growth on an icy body orbiting Saturn and evolution of bidirectional reflectance due to surface composition changes. *Icarus* 212(1):268–274. <https://doi.org/10.1016/j.icarus.2010.10.031>
- Elliott J, Esposito L (2021) Macroscopic roughness, composition and age of saturns rings and FUV phase curve analysis. In: AGU Fall Meeting abstracts, pp P35E-2167
- Elrod MK, Tseng WL, Wilson RJ, et al (2012) Seasonal variations in Saturn's plasma between the main rings and Enceladus. *J Geophys Res Space Phys* 117(A3):A03207. <https://doi.org/10.1029/2011JA017332>
- Elrod MK, Tseng WL, Woodson AK, et al (2014) Seasonal and radial trends in Saturn's thermal plasma between the main rings and Enceladus. *Icarus* 242:130–137
- Esposito LW, De Stefano M (2018) Space age studies of planetary rings. In: Tiscareno MS, Murray CD (eds) Planetary ring systems. Properties, structure, and evolution. Cambridge University Press, pp 3–29. <https://doi.org/10.1017/9781316286791.001>
- Esposito LW, Barth CA, Colwell JE, et al (2004) The Cassini ultraviolet imaging spectrograph investigation. *Space Sci Rev* 115(1–4):299–361. <https://doi.org/10.1007/s11214-004-1455-8>
- Esposito LW, Albers N, Meinke BK, et al (2012) A predator-prey model for moon-triggered clumping in Saturn's rings. *Icarus* 217(1):103–114. <https://doi.org/10.1016/j.icarus.2011.09.029>
- Estrada PR, Cuzzi JN (1996) Voyager observations of the color of Saturn's rings. *Icarus* 122(2):251–272. <https://doi.org/10.1006/icar.1996.0124>
- Estrada PR, Durisen RH, Cuzzi JN, et al (2015) Combined structural and compositional evolution of planetary rings due to micrometeoroid impacts and ballistic transport. *Icarus* 252:415–439. <https://doi.org/10.1016/j.icarus.2015.02.005>
- Farrell WM, Kaiser ML, Kurnett DA, et al (2008) Mass unloading along the inner edge of the Enceladus plasma torus. *Geophys Res Lett* 35(2):L02203. <https://doi.org/10.1029/2007GL032306>
- Ferrari C, Galdemard P, Lagage PO, et al (2005) Imaging Saturn's rings with CAMIRAS: thermal inertia of B and C rings. *Astron Astrophys* 441(1):379–389. <https://doi.org/10.1051/0004-6361:20053100>
- Filacchione G, Capaccioni F, Ciarniello M, et al (2012) Saturn's icy satellites and rings investigated by Cassini-VIMS: III - radial compositional variability. *Icarus* 220(2):1064–1096. <https://doi.org/10.1016/j.icarus.2012.06.040>. arXiv:1203.6230 [astro-ph.EP]
- Filacchione G, Ciarniello M, Capaccioni F, et al (2014) Cassini-VIMS observations of Saturn's main rings: I. Spectral properties and temperature radial profiles variability with phase angle and elevation. *Icarus* 241:45–65. <https://doi.org/10.1016/j.icarus.2014.06.001>
- Filacchione G, D'Aversa E, Capaccioni F, et al (2016) Saturn's icy satellites investigated by Cassini-VIMS. IV. Daytime temperature maps. *Icarus* 271:292–313. <https://doi.org/10.1016/j.icarus.2016.02.019>. arXiv:1602.02890 [astro-ph.EP]
- Fischer C, Postberg F, Altobelli N, et al (2018) Mineral dust in the Saturnian system. In: European Planetary Science Congress, EPSC2018–1279
- Flasar FM, Kunde VG, Abbas MM, et al (2004) Exploring the Saturn system in the thermal infrared: the composite infrared spectrometer. *Space Sci Rev* 115(1–4):169–297. <https://doi.org/10.1007/s11214-004-1454-9>
- French RG, Nicholson PD (2000) Saturn's rings II. Particle sizes inferred from stellar occultation data. *Icarus* 145(2):502–523. <https://doi.org/10.1006/icar.2000.6357>
- Goldreich P, Tremaine SD (1978) The velocity dispersion in Saturn's rings. *Icarus* 34(2):227–239. [https://doi.org/10.1016/0019-1035\(78\)90164-1](https://doi.org/10.1016/0019-1035(78)90164-1)
- Grossman AW (1990) Microwave imaging of Saturn's deep atmosphere and rings. PhD thesis, California Institute of Technology
- Hamil O, Cravens TE, Reedy NL, et al (2018) Fate of ice grains in Saturn's ionosphere. *J Geophys Res Space Phys* 123(2):1429–1440. <https://doi.org/10.1002/2017JA024616>

- Hamilton DC, Christon SP, Mitchell DG, et al (2018) A large seasonal variation of energetic C⁺ and CO⁺ abundances in Saturn's magnetosphere probably resulting from changing ring illumination. In: Cassini science symposium, pp 29–30. <https://lasp.colorado.edu/home/wp-content/uploads/2018/08/Cassini-Science-Symposium-Program-with-cover-web.pdf>
- Hapke B (1993) Theory of reflectance and emittance spectroscopy. Cambridge University Press. <https://doi.org/10.1017/CBO9780511524998>
- Hapke B (2012) Theory of reflectance and emittance spectroscopy, 2nd edn. Cambridge University Press, Cambridge. <https://doi.org/10.1017/CBO9781139025683>
- Hapke B (2013) Comment on “A critical assessment of the Hapke photometric model” by Y. Shkuratov et al. *J Quant Spectrosc Radiat Transf* 116:184–190. <https://doi.org/10.1016/j.jqsrt.2012.11.002>
- Harbison RA, Nicholson PD, Hedman MM (2013) The smallest particles in Saturn's A and C rings. *Icarus* 226(2):1225–1240. <https://doi.org/10.1016/j.icarus.2013.08.015>. arXiv:1312.2927 [astro-ph.EP]
- Harris AW (1984) The origin and evolution of planetary rings. In: Greenberg R, Brahic A (eds) IAU colloq. 75: Planetary rings. University of Arizona Press, Tucson, pp 641–659
- Hedman MM (2019) Bright clumps in the D68 ringlet near the end of the Cassini mission. *Icarus* 323:62–75. <https://doi.org/10.1016/j.icarus.2019.01.007>. arXiv:1901.02043 [astro-ph.EP]
- Hedman MM, Nicholson PD (2013) Kronoseismology: using density waves in Saturn's C ring to probe the planet's interior. *Astron J* 146(1):12. <https://doi.org/10.1088/0004-6256/146/1/12>. arXiv:1304.3735 [astro-ph.EP]
- Hedman MM, Nicholson PD (2014) More Kronoseismology with Saturn's rings. *Mon Not R Astron Soc* 444(2):1369–1388. <https://doi.org/10.1093/mnras/stu1503>. arXiv:1407.6702 [astro-ph.EP]
- Hedman MM, Nicholson PD (2016) The B-ring's surface mass density from hidden density waves: less than meets the eye?. *Icarus* 279:109–124. <https://doi.org/10.1016/j.icarus.2016.01.007>. arXiv:1601.07955 [astro-ph.EP]
- Hedman MM, Showalter MR (2016) A new pattern in Saturn's D ring created in late 2011. *Icarus* 279:155–165. <https://doi.org/10.1016/j.icarus.2015.09.017>. arXiv:1509.04755 [astro-ph.EP]
- Hedman MM, Stark CC (2015) Saturn's G and D rings provide nearly complete measured scattering phase functions of nearby debris disks. *Astrophys J* 811(1):67. <https://doi.org/10.1088/0004-637X/811/1/67>. arXiv:1508.00261 [astro-ph.EP]
- Hedman MM, Burns JA, Showalter MR, et al (2007a) Saturn's dynamic D ring. *Icarus* 188(1):89–107. <https://doi.org/10.1016/j.icarus.2006.11.017>
- Hedman MM, Nicholson PD, Salo H, et al (2007b) Self-gravity wake structures in Saturn's A ring revealed by Cassini VIMS. *Astron J* 133(6):2624–2629. <https://doi.org/10.1086/516828>
- Hedman MM, Burns JA, Tiscareno MS, et al (2009) Organizing some very tenuous things: resonant structures in Saturn's faint rings. *Icarus* 202(1):260–279. <https://doi.org/10.1016/j.icarus.2009.02.016>
- Hedman MM, Nicholson PD, Showalter MR, et al (2011) The christiansen effect in Saturn's narrow dusty rings and the spectral identification of clumps in the F ring. *Icarus* 215(2):695–711. <https://doi.org/10.1016/j.icarus.2011.02.025>. arXiv:1102.5116 [astro-ph.EP]
- Hedman MM, Nicholson PD, Cuzzi JN, et al (2013) Connections between spectra and structure in Saturn's main rings based on Cassini VIMS data. *Icarus* 223(1):105–130. <https://doi.org/10.1016/j.icarus.2012.10.014>. arXiv:1210.4727 [astro-ph.EP]
- Hedman MM, Burns JA, Showalter MR (2015) Corrugations and eccentric spirals in Saturn's D ring: new insights into what happened at Saturn in 1983. *Icarus* 248:137–161. <https://doi.org/10.1016/j.icarus.2014.10.021>. arXiv:1410.3761 [astro-ph.EP]
- Hedman M, Postberg F, Hamilton D, et al (2018) Dusty rings. In: Tiscareno MS, Murray CD (eds) Planetary ring systems. Properties, structure, and evolution. Cambridge University Press, Cambridge, pp 308–337
- Hendrix AR, Hansen CJ (2008) Ultraviolet observations of Phoebe from the Cassini UVIS. *Icarus* 193(2):323–333. <https://doi.org/10.1016/j.icarus.2007.06.030>
- Hsu HW, Schmidt J, Kempf S, et al (2018) In situ collection of dust grains falling from Saturn's rings into its atmosphere. *Science* 362(6410):aat3185. <https://doi.org/10.1126/science.aat3185>
- Iess L, Militzer B, Kaspi Y, et al (2019) Measurement and implications of Saturn's gravity field and ring mass. *Science* 364(6445):aat2965. <https://doi.org/10.1126/science.aat2965>
- Imanaka H, Khare BN, Elsila JE, et al (2004) Laboratory experiments of Titan tholin formed in cold plasma at various pressures: implications for nitrogen-containing polycyclic aromatic compounds in Titan haze. *Icarus* 168(2):344–366. <https://doi.org/10.1016/j.icarus.2003.12.014>
- Imanaka H, Cruikshank DP, Khare BN, et al (2012) Optical constants of Titan tholins at mid-infrared wavelengths (2.5–25 μm) and the possible chemical nature of Titan's haze particles. *Icarus* 218(1):247–261. <https://doi.org/10.1016/j.icarus.2011.11.018>
- Ip WH (1983) On plasma transport in the vicinity of the rings of Saturn: a Siphon flow mechanism. *J Geophys Res* 88(A2):819–822. <https://doi.org/10.1029/JA088iA02p00819>

- Ip WH, Liu CM, Pan KC (2016) Transport and electrodynamical coupling of nano-grains ejected from the Saturnian rings and their possible ionospheric signatures. *Icarus* 276:163–169. <https://doi.org/10.1016/j.icarus.2016.04.004>
- Jaffe H, Orchin M (1962) Theory and applications of ultraviolet spectroscopy. Wiley, London
- Jerousek R (2018) Determining the small-scale structure and particle properties in Saturn's rings from stellar and radio occultations. PhD thesis, University of Central Florida
- Jerousek RG, Colwell JE, Esposito LW (2011) Morphology and variability of the Titan ringlet and Huygens ringlet edges. *Icarus* 216(1):280–291. <https://doi.org/10.1016/j.icarus.2011.09.001>
- Jerousek RG, Colwell JE, Esposito LW, et al (2016) Small particles and self-gravity wakes in Saturn's rings from UVIS and VIMS stellar occultations. *Icarus* 279:36–50. <https://doi.org/10.1016/j.icarus.2016.04.039>
- Jerousek RG, Colwell JE, Hedman MM, et al (2020) Saturn's C ring and Cassini division: particle sizes from Cassini UVIS, VIMS, and RSS occultations. *Icarus* 344:113565. <https://doi.org/10.1016/j.icarus.2019.113565>
- Johansson FL, Vigren E, Waite JH, et al (2022) Implications from secondary emission from neutral impact on Cassini plasma and dust measurements. *Mon Not R Astron Soc* 515(2):2340–2350
- Johnson RE, Carlson RW, Cooper JF, et al (2004) Radiation effects on the surfaces of the Galilean satellites. In: Bagenal F, Dowling TE, McKinnon WB (eds) Jupiter. The planet, satellites and magnetosphere, vol 1, pp 485–512
- Johnson RE, Luhmann JG, Tokar RL, et al (2006) Production, ionization and redistribution of O₂ in Saturn's ring atmosphere. *Icarus* 180(2):393–402. <https://doi.org/10.1016/j.icarus.2005.08.021>
- Jurac S, Richardson JD (2007) Neutral cloud interaction with Saturn's main rings. *Geophys Res Lett* 34(8):L08102. <https://doi.org/10.1029/2007GL029567>
- Kempf S (2008) Interpretation of high rate dust measurements with the Cassini dust detector CDA. *Planet Space Sci* 56(3–4):378–385. <https://doi.org/10.1016/j.pss.2007.11.022>
- Kempf S, Altobelli N, Schmidt J, et al (2023) Micrometeoroid infall onto Saturn's rings constrains their age to no more than a few hundred million years. *Sci Adv* 9(19):eabd8537 <https://doi.org/10.1126/sciadv.abd8537>
- Kliore Astron J, Patel IR, Lindal GF, et al (1980) Structure of the ionosphere and atmosphere of Saturn from pioneer 11 Saturn radio occultation. *J Geophys Res Space Phys* 85(A11):5857–5870
- Kliore Astron J, Anderson JD, Armstrong JW, et al (2004) Cassini Radio Sci Space Sci Rev 115(1–4):1–70. <https://doi.org/10.1007/s11214-004-1436-y>
- Kliore A, Nagy A, Marouf E, et al (2009) Midlatitude and high-latitude electron density profiles in the ionosphere of Saturn obtained by Cassini radio occultation observations. *J Geophys Res Space Phys* 114(A4)
- Kollmann P, Roussos E, Kotova A, et al (2018) Saturn's innermost radiation belt throughout and inward of the D-ring. *Geophys Res Lett* 45(20):10,912–10,920. <https://doi.org/10.1029/2018GL077954>
- Koskinen TT, Guerlet S (2018) Atmospheric structure and helium abundance on Saturn from Cassini/UVIS and CIRS observations. *Icarus* 307:161–171. <https://doi.org/10.1016/j.icarus.2018.02.020>
- Krimigis S, Mitchell D, Hamilton D, et al (2004) Magnetosphere imaging instrument (MIMI) on the Cassini mission to Saturn/Titan In: Russell CT (ed) The Cassini-Huygens Mission: orbiter in situ investigations, vol 2. Springer, Dordrecht, pp 233–329. https://doi.org/10.1007/978-1-4419-2774-1_3
- Linti S, Postberg F, Hsu HW, et al (2024) Iron depletion in mineral dust grains from Saturn's main rings. *Mon Not R Astron Soc* 529(2):1207–1221. <https://doi.org/10.1093/mnras/stae603>
- Longaretti PY (2018) Theory of narrow rings and sharp edges. In: Tiscareno MS, Murray CD (eds) Planetary ring systems. Properties, structure, and evolution. Cambridge University Press, pp 225–275. <https://doi.org/10.1017/9781316286791.010>
- Luhmann JG, Johnson RE, Tokar RL, et al (2006) A model of the ionosphere of Saturn's rings and its implications. *Icarus* 181(2):465–474. <https://doi.org/10.1016/j.icarus.2005.11.022>
- Lynden-Bell D, Pringle JE (1974) The evolution of viscous discs and the origin of the nebular variables. *Mon Not R Astron Soc* 168:603–637. <https://doi.org/10.1093/mnras/168.3.603>
- Magee BA, Waite JH, Mandt KE, et al (2009) INMS-derived composition of Titan's upper atmosphere: analysis methods and model comparison. *Planet Space Sci* 57(14–15):1895–1916. <https://doi.org/10.1016/j.pss.2009.06.016>
- Mallochi G, Mulas G, Joblin C (2004) Electronic absorption spectra of PAHs up to vacuum UV. Towards a detailed model of interstellar PAH photophysics. *Astron Astrophys* 426:105–117. <https://doi.org/10.1051/0004-6361:20040541>
- Marouf EA, Tyler GL, Rosen PA (1986) Profiling Saturn's rings by radio occultation. *Icarus* 68(1):120–166. [https://doi.org/10.1016/0019-1035\(86\)90078-3](https://doi.org/10.1016/0019-1035(86)90078-3)
- Mason E, Marrero T (1970) The diffusion of atoms and molecules. In: Advances in atomic and molecular physics, vol 6. Elsevier, Amsterdam, pp 155–232

- Mastrapa RM, Sandford SA, Roush TL, et al (2009) Optical constants of amorphous and crystalline H₂O-ice: 2.5–22 μm (4000–455 cm⁻¹) optical constants of H₂O-ice. *Astrophys J* 701(2):1347–1356. <https://doi.org/10.1088/0004-637X/701/2/1347>
- Miller KE, Waite JH, Perryman RS, et al (2020) Cassini INMS constraints on the composition and latitudinal fractionation of Saturn ring rain material. *Icarus* 339:113595. <https://doi.org/10.1016/j.icarus.2019.113595>
- Mitchell DG, Perry ME, Hamilton DC, et al (2018) Dust grains fall from Saturn's D-ring into its equatorial upper atmosphere. *Science* 362(6410):aa2236. <https://doi.org/10.1126/science.aa2236>
- Moore L, O'Donoghue J, Müller-Wodarg I, et al (2015) Saturn ring rain: model estimates of water influx into Saturn's atmosphere. *Icarus* 245:355–366. <https://doi.org/10.1016/j.icarus.2014.08.041>
- Morishima R, Spilker L, Salo H, et al (2010) A multilayer model for thermal infrared emission of Saturn's rings II: albedo, spins, and vertical mixing of ring particles inferred from Cassini CIRS. *Icarus* 210(1):330–345. <https://doi.org/10.1016/j.icarus.2010.06.032>
- Morishima R, Spilker L, Ohtsuki K (2011) A multilayer model for thermal infrared emission of Saturn's rings. III: thermal inertia inferred from Cassini CIRS. *Icarus* 215(1):107–127. <https://doi.org/10.1016/j.icarus.2011.06.042>. arXiv:1209.3797 [astro-ph.EP]
- Morishima R, Edgington SG, Spilker L (2012) Regolith grain sizes of Saturn's rings inferred from Cassini-CIRS far-infrared spectra. *Icarus* 221(2):888–899. <https://doi.org/10.1016/j.icarus.2012.09.012>. arXiv:1209.3799 [astro-ph.EP]
- Moses JI, Brown ZL, Koskinen TT, et al (2023) Saturn's atmospheric response to the large influx of ring material inferred from Cassini INMS measurements. *Icarus* 391:115328. <https://doi.org/10.1016/j.icarus.2022.115328>. arXiv:2211.05253 [astro-ph.EP]
- Murray CD, French RS (2018) The F ring of Saturn. In: Tiscareno MS, Murray CD (eds) Planetary ring systems. Properties, structure, and evolution. Cambridge University Press, pp 338–362. <https://doi.org/10.1017/9781316286791.013>
- Nicholson PD, Hedman MM, Clark RN, et al (2008) A close look at Saturn's rings with Cassini VIMS. *Icarus* 193(1):182–212. <https://doi.org/10.1016/j.icarus.2007.08.036>
- Nicholson PD, French RG, Spitale JN (2018) Narrow rings, gaps, and sharp edges. In: Tiscareno MS, Murray CD (eds) Planetary ring systems. Properties, structure, and evolution. Cambridge University Press, pp 276–307. <https://doi.org/10.1017/9781316286791.011>
- Northrop TG, Connerney JEP (1987) A micrometeorite erosion model and the age of Saturn's rings. *Icarus* 70(1):124–137. [https://doi.org/10.1016/0019-1035\(87\)90079-0](https://doi.org/10.1016/0019-1035(87)90079-0)
- Northrop T, Hill JR (1982) Stability of negatively charged dust grains in Saturn's ring plane. *J Geophys Res Space Phys* 87(A8):6045–6051
- O'Donoghue J, Stallard TS, Melin H, et al (2013) The domination of Saturn's low-latitude ionosphere by ring 'rain'. *Nature* 496(7444):193–195. <https://doi.org/10.1038/nature12049>. arXiv:1310.7293 [astro-ph.EP]
- O'Donoghue J, Moore L, Connerney J, et al (2019) Observations of the chemical and thermal response of 'ring rain' on Saturn's ionosphere. *Icarus* 322:251–260. <https://doi.org/10.1016/j.icarus.2018.10.027>
- Pendleton YJ, Allamandola LJ (2002) The organic refractory material in the diffuse interstellar medium: mid-infrared spectroscopic constraints. *Astrophys J Suppl Ser* 138(1):75–98. <https://doi.org/10.1086/322999>
- Perry ME, Waite JH, Mitchell DG, et al (2018) Material flux from the rings of Saturn into its atmosphere. *Geophys Res Lett* 45(19):10,093–10,100. <https://doi.org/10.1029/2018GL078575>
- Pettengill GH, Hagfors T (1974) Comment on radar scattering from Saturn's rings. *Icarus* 21(2):188–190. [https://doi.org/10.1016/0019-1035\(74\)90135-3](https://doi.org/10.1016/0019-1035(74)90135-3)
- Pitman KM, Buratti BJ, Mosher JA (2010) Disk-integrated bolometric bond albedos and rotational light curves of saturnian satellites from Cassini visual and infrared mapping spectrometer. *Icarus* 206(2):537–560. <https://doi.org/10.1016/j.icarus.2009.12.001>
- Pollack JB, Summers A, Baldwin B (1973) Estimates of the sizes of the particles in the rings of Saturn and their cosmogonic implications. *Icarus* 20(3):263–278. [https://doi.org/10.1016/0019-1035\(73\)90003-1](https://doi.org/10.1016/0019-1035(73)90003-1)
- Poulet F, Cruikshank DP, Cuzzi JN, et al (2003) Compositions of Saturn's rings A, B, and C from high resolution near-infrared spectroscopic observations. *Astron Astrophys* 412:305–316. <https://doi.org/10.1051/0004-6361:20031123>
- Raponi A, Ciarniello M, Capaccioni F, et al (2020) Infrared detection of aliphatic organics on a cometary nucleus. *Nat Astron* 4:500–505. <https://doi.org/10.1038/s41550-019-0992-8>. arXiv:2009.14476 [astro-ph.EP]
- Reynard B, Sotin C (2023) Carbon-rich icy moons and dwarf planets. *Earth Planet Sci Lett* 612:118172. <https://doi.org/10.1016/j.epsl.2023.118172>
- Rouleau F, Martin PG (1991) Shape and clustering effects on the optical properties of amorphous carbon. *Astrophys J* 377:526. <https://doi.org/10.1086/170382>

- Roush TL (1994) Charon: more than water ice? *Icarus* 108(2):243–254. <https://doi.org/10.1006/icar.1994.1059>
- Salama F, Bakes ELO, Allamandola LJ, et al (1996) Assessment of the polycyclic aromatic hydrocarbon–diffuse interstellar band proposal. *Astrophys J* 458:621. <https://doi.org/10.1086/176844>
- Schmidt J, Ohtsuki K, Rappaport N, et al (2009) Dynamics of Saturn's dense rings. In: Dougherty MK, Esposito LW, Krimigis SM (eds) *Saturn from Cassini-Huygens*. Springer, Dordrecht, pp 413–458. https://doi.org/10.1007/978-1-4020-9217-6_14
- Serigano J, Hörst SM, He C, et al (2020) Compositional measurements of Saturn's upper atmosphere and rings from Cassini INMS. *J Geophys Res, Planets* 125(8):e06427. <https://doi.org/10.1029/2020JE006427>. arXiv:2005.06554 [astro-ph.EP]
- Serigano J, Hörst SM, He C, et al (2022) Compositional measurements of Saturn's upper atmosphere and rings from Cassini INMS: an extended analysis of measurements from Cassini's grand finale orbits. *J Geophys Res, Planets* 127(6):e07238. <https://doi.org/10.1029/2022JE007238>
- Shkuratov Y, Starukhina L, Hoffmann H, et al (1999) A model of spectral albedo of particulate surfaces: implications for optical properties of the moon. *Icarus* 137(2):235–246. <https://doi.org/10.1006/icar.1998.6035>
- Shkuratov YG, Stankevich DG, Petrov DV, et al (2005) Interpreting photometry of regolith-like surfaces with different topographies: shadowing and multiple scattering. *Icarus* 173(1):3–15. <https://doi.org/10.1016/j.icarus.2003.12.017>
- Shkuratov Y, Kaydash V, Korokhin V, et al (2012) A critical assessment of the Hapke photometric model. *J Quant Spectrosc Radiat Transf* 113(18):2431–2456. <https://doi.org/10.1016/j.jqsrt.2012.04.010>
- Showalter MR (1996) Saturn's D ring in the Voyager images. *Icarus* 124(2):677–689. <https://doi.org/10.1006/icar.1996.0241>
- Smith HT, Richardson JD (2021) The 3d structure of Saturn magnetospheric neutral tori produced by the Enceladus plumes. *J Geophys Res Space Phys* A028:775
- Smith BA, Soderblom L, Beebe R, et al (1981) Encounter with Saturn: Voyager 1 imaging science results. *Science* 212(4491):163–191
- Spahn F, Sremčević M (2000) Density patterns induced by small moonlets in Saturn's rings? *Astron Astrophys* 358:368–372
- Spahn F, Hoffmann H, Rein H, et al (2018) Moonlets in dense planetary rings. In: Tiscareno MS, Murray CD (eds) *Planetary ring systems. Properties, structure, and evolution*. Cambridge University Press, pp 157–197. <https://doi.org/10.1017/9781316286791.008>
- Spilker LJ, Pilorz SH, Edgington SG, et al (2005) Cassini CIRS observations of a roll-off in Saturn ring spectra at submillimeter wavelengths. *Earth Moon Planets* 96(3–4):149–163. <https://doi.org/10.1007/s11038-005-9060-8>
- Spilker LJ, Pilorz SH, Wallis BD, et al (2006) Cassini thermal observations of Saturn's main rings: implications for particle rotation and vertical mixing. *Planet Space Sci* 54(12):1167–1176. <https://doi.org/10.1016/j.pss.2006.05.033>
- Spilker L, Ferrari C, Morishima R (2013) Saturn's ring temperatures at equinox. *Icarus* 226(1):316–322. <https://doi.org/10.1016/j.icarus.2013.06.002>
- Spilker LJ, Ferrari C, Altobelli N, et al (2018) Thermal properties of rings and ring particles. In: Tiscareno MS, Murray CD (eds) *Planetary ring systems. Properties, structure, and evolution*. Cambridge University Press, pp 399–433. <https://doi.org/10.1017/9781316286791.015>
- Srama R, Ahrens TJ, Altobelli N, et al (2004) The Cassini cosmic dust analyzer. *Space Sci Rev* 114(1–4):465–518. <https://doi.org/10.1007/s11214-004-1435-z>
- Tajeddine R, Nicholson PD, Longaretti PY, et al (2017) What confines the rings of Saturn? *Astrophys J Suppl Ser* 232(2):28. <https://doi.org/10.3847/1538-4365/aa8c09>. arXiv:1710.08462 [astro-ph.EP]
- Tiscareno MS, Harris BE (2018) Mapping spiral waves and other radial features in Saturn's rings. *Icarus* 312:157–171. <https://doi.org/10.1016/j.icarus.2018.04.023>. arXiv:1708.03702 [astro-ph.EP]
- Tiscareno MS, Murray CD (2018) Planetary ring systems: properties, structure, and evolution. Cambridge University Press, Cambridge. <https://doi.org/10.1017/9781316286791>
- Tiscareno MS, Burns JA, Hedman MM, et al (2006) 100-metre-diameter moonlets in Saturn's A ring from observations of "propeller" structures. *Nature* 440(7084):648–650. <https://doi.org/10.1038/nature04581>
- Tiscareno MS, Burns JA, Nicholson PD, et al (2007) Cassini imaging of Saturn's rings. II. A wavelet technique for analysis of density waves and other radial structure in the rings. *Icarus* 189(1):14–34. <https://doi.org/10.1016/j.icarus.2006.12.025>. astro-ph. arXiv:astro-ph/0610242
- Tiscareno MS, Burns JA, Hedman MM, et al (2008) The population of propellers in Saturn's A ring. *Astron J* 135(3):1083–1091. <https://doi.org/10.1088/0004-6256/135/3/1083>. astro-ph. arXiv:0710.4547
- Tiscareno MS, Burns JA, Sremčević M, et al (2010) Physical characteristics and non-Keplerian orbital motion of "propeller" moons embedded in Saturn's rings. *Astrophys J Lett* 718(2):L92–L96. <https://doi.org/10.1088/2041-8205/718/2/L92>. arXiv:1007.1008 [astro-ph.EP]

- Tiscareno MS, Hedman MM, Burns JA, et al (2013a) Compositions and origins of outer planet systems: insights from the Roche critical density. *Astrophys J Lett* 765(2):L28. <https://doi.org/10.1088/2041-8205/765/2/L28>. arXiv:1302.1253 [astro-ph.EP]
- Tiscareno MS, Hedman MM, Burns JA, et al (2013b) Probing the inner boundaries of Saturn's A ring with the Iapetus -1:0 nodal bending wave. *Icarus* 224(1):201–208. <https://doi.org/10.1016/j.icarus.2013.02.026>. arXiv:1302.5712 [astro-ph.EP]
- Tiscareno MS, Nicholson PD, Cuzzi JN, et al (2019) Close-range remote sensing of Saturn's rings during Cassini's ring-grazing orbits and grand finale. *Science* 364(6445):aau1017. <https://doi.org/10.1126/science.aaau1017>
- Tokar RL, Johnson RE, Thomsen MF, et al (2005) Cassini observations of the thermal plasma in the vicinity of Saturn's main rings and the F and G rings. *Geophys Res Lett* 32(14):L14S04. <https://doi.org/10.1029/2005GL022690>
- Toomre A (1964) On the gravitational stability of a disk of stars. *Astrophys J* 139:1217–1238. <https://doi.org/10.1086/147861>
- Trieloff M, Fischer C, Postberg F, et al (2023) Dynamical analysis of mineral dust in the Saturnian system. In: EGU General Assembly 2023. Vienna, Austria, 24–28 Apr 2023, EGU23-16469. <https://doi.org/10.5194/egusphere-egu23-16469>
- Tseng WL, Ip WH (2011) An assessment and test of Enceladus as an important source of Saturn's ring atmosphere and ionosphere. *Icarus* 212(1):294–299. <https://doi.org/10.1016/j.icarus.2010.12.003>
- Tseng WL, Ip WH, Johnson RE, et al (2010) The structure and time variability of the ring atmosphere and ionosphere. *Icarus* 206(2):382–389. <https://doi.org/10.1016/j.icarus.2009.05.019>
- Tseng WL, Johnson RE, Thomsen MF, et al (2011) Neutral H₂ and H₂⁺ ions in the Saturnian magnetosphere. *J Geophys Res Space Phys* 116(A3):A03209. <https://doi.org/10.1029/2010JA016145>
- Tseng WL, Johnson RE, Elrod MK (2013a) Modeling the seasonal variability of the plasma environment in Saturn's magnetosphere between main rings and Mimas. *Planet Space Sci* 77:126–135. <https://doi.org/10.1016/j.pss.2012.05.001>. arXiv:1112.5511 [astro-ph.EP]
- Tseng WL, Johnson RE, Ip WH (2013b) The atomic hydrogen cloud in the saturnian system. *Planet Space Sci* 85, 164–174. <https://doi.org/10.1016/j.pss.2013.06.005>. arXiv:1302.3270 [astro-ph.EP]
- Tyler GL, Eshleman VR, Anderson JD, et al (1981) Radio science investigations of the Saturn system with Voyager 1: preliminary results. *Science* 212(4491):201–206. <https://doi.org/10.1126/science.212.4491.201>
- Vahidinia S, Cuzzi JN, Hedman M, et al (2011) Saturn's F ring grains: aggregates made of crystalline water ice. *Icarus* 215(2):682–694. <https://doi.org/10.1016/j.icarus.2011.04.011>
- van de Hulst HC (1981) Light scattering by small particles. Courier Corporation.
- Verbiscer Astron J, Skrutskie MF, Hamilton DP (2009) Saturn's largest ring. *Nature* 461(7267):1098–1100. <https://doi.org/10.1038/nature08515>
- Vigren E, Dreyer J, Eriksson AI, et al (2022) Empirical photochemical modeling of Saturn's ionization balance including grain charging. *Planet Sci J* 3(2):49
- Waite JH, Atreya SK, Nagy AF (1979) The ionosphere of Saturn: predictions for pioneer 11. *Geophys Res Lett* 6(9):723–726. <https://doi.org/10.1029/GL006i009p00723>
- Waite JH, Lewis W, Kasprzak W, et al (2004) The Cassini Ion and Neutral Mass Spectrometer (INMS) investigation. In: Russell CT (ed) The Cassini-Huygens Mission: orbiter in situ investigations, vol 2. Springer, Dordrecht, pp 113–231. https://doi.org/10.1007/978-1-4020-2774-1_2
- Waite JH, Cravens TE, Ip WH, et al (2005) Oxygen ions observed near Saturn's A ring. *Science* 307(5713):1260–1262. <https://doi.org/10.1126/science.1105734>
- Waite JH, Perryman RS, Perry ME, et al (2018) Chemical interactions between Saturn's atmosphere and its rings. *Science* 362(6410):aat2382. <https://doi.org/10.1126/science.aat2382>
- West R, Lavvas P, Anderson C, et al (2014) Titan's haze. In: Titan, pp 285. <https://doi.org/10.1017/CBO9780511667398.011>
- Yelle RV, Serigano J, Koskinen TT, et al (2018) Thermal structure and composition of Saturn's upper atmosphere from Cassini/Ion Neutral Mass Spectrometer measurements. *Geophys Res Lett* 45(20):10,951–10,958. <https://doi.org/10.1029/2018GL078454>
- Young D, Berthelier J, Blanc M, et al (2004) Cassini Plasma Spectrometer investigation. In: Russell CT (ed) The Cassini-Huygens Mission: orbiter in situ investigations, vol 2. Springer, Dordrecht, pp 1–112. https://doi.org/10.1007/978-1-4020-2774-1_1
- Zebker HA, Marouf EA, Tyler GL (1985) Saturn's rings: particle size distributions for thin layer models. *Icarus* 64(3):531–548. [https://doi.org/10.1016/0019-1035\(85\)90074-0](https://doi.org/10.1016/0019-1035(85)90074-0)
- Zhang Z, Hayes AG, Janssen MA, et al (2017a) Exposure age of Saturn's A and B rings, and the Cassini division as suggested by their non-icy material content. *Icarus* 294:14–42. <https://doi.org/10.1016/j.icarus.2017.04.008>

- Zhang Z, Hayes AG, Janssen MA, et al (2017b) Cassini microwave observations provide clues to the origin of Saturn's C ring. *Icarus* 281:297–321. <https://doi.org/10.1016/j.icarus.2016.07.020>
- Zhang Z, Hayes AG, de Pater I, et al (2019) VLA multi-wavelength microwave observations of Saturn's C and B rings. *Icarus* 317:518–548. <https://doi.org/10.1016/j.icarus.2018.08.014>

Publisher's Note Springer Nature remains neutral with regard to jurisdictional claims in published maps and institutional affiliations.

Authors and Affiliations

Kelly E. Miller¹ · Gianrico Filacchione²  · Jeffrey N. Cuzzi³ · Philip D. Nicholson⁴ ·
Matthew M. Hedman⁵ · Kevin Baillié⁶ · Robert E. Johnson⁷ · Wei-Ling Tseng⁸ ·
Paul R. Estrada³ · Jack Hunter Waite⁹ · Mauro Ciarniello² · Cécile Ferrari¹⁰ ·
Zhimeng Zhang¹¹ · Amanda Hendrix¹² · Julianne I. Moses¹³ · Hsiang-Wen Hsu¹⁴

 G. Filacchione
gianrico.filacchione@inaf.it

K.E. Miller
kmiller@swri.edu

J.N. Cuzzi
jeffrey.cuzzi@nasa.gov

P.D. Nicholson
pdn2@cornell.edu

M.M. Hedman
mhedman@uidaho.edu

K. Baillié
kevin.baillie@obspm.fr

R.E. Johnson
rej@virginia.edu

W.-L. Tseng
wltsgeng@ntnu.edu.tw

P.R. Estrada
paul.r.estrada@nasa.gov

J.H. Waite
hunterwaite@gmail.com

M. Ciarniello
mauro.ciarniello@inaf.it

C. Ferrari
ferrari@ipgp.fr

Z. Zhang
zzm19881204@gmail.com

A. Hendrix
ahendrix@psi.edu

J.I. Moses
jmoses@space-science.org

H.-W. Hsu
sean.hsu@lasp.colorado.edu

¹ Space Science, Southwest Research Institute, 9503 W. Commerce, San Antonio, TX, 78227, USA

- 2 INAF, IAPS Institute for Space Astrophysics and Planetology, via del Fosso del Cavaliere, 100,
Rome, 00133, Italy
- 3 Space Sciences Div., NASA Ames Research Center, MS 245-3, Moffett Field, CA, 94035, USA
- 4 Department of Astronomy, Cornell University, Ithaca, NY, 14853, USA
- 5 Department of Physics, University of Idaho, Moscow, ID, 83844, USA
- 6 IMCCE, Observatoire de Paris, PSL Research University, CNRS, Sorbonne Universités, UPMC
Univ Paris 06, Univ. Lille, 77 Av. Denfert-Rochereau, Paris, 75014, France
- 7 Engineering Physics, University of Virginia, Charlottesville, VA, 22902, USA
- 8 Department of Earth Sciences, National Taiwan Normal University, Taipei, 116, Taiwan
- 9 Waite Science, LLC, 16284 Narwhal Drive, Pensacola, FL, 32507, USA
- 10 Université de Paris Cité, Institut de physique du globe de Paris, CNRS, Paris, F-75005, France
- 11 Division of Geological and Planetary Sciences, California Institute of Technology, Pasadena, CA,
91125, USA
- 12 Planetary Science Institute, Tucson, AZ, 85719, USA
- 13 Space Science Institute, Boulder, CO, 80301, USA
- 14 Laboratory for Atmospheric and Space Physics, University of Colorado-Boulder, Boulder, CO,
80303, USA